

Hu Wu

Gravity field recovery from GOCE observations

München 2016

**Verlag der Bayerischen Akademie der Wissenschaften
in Kommission beim Verlag C. H. Beck**

ISSN 0065-5325

ISBN 978-3-7696-5189-8

**Diese Arbeit ist gleichzeitig veröffentlicht in:
Wissenschaftliche Arbeiten der Fachrichtung Geodäsie und Geoinformatik der Leibniz Universität Hannover
ISSN 0174-1454, Nr. 324, Hannover 2016**

Gravity field recovery from GOCE observations

Von der Fakultät für Bauingenieurwesen und Geodäsie
der Gottfried Wilhelm Leibniz Universität Hannover
zur Erlangung des Grades
Doktor-Ingenieur (Dr.-Ing.)
genehmigte Dissertation

von

M.Sc. Hu Wu

geboren am 25.09.1986 in Anhui, China

München 2016

Verlag der Bayerischen Akademie der Wissenschaften
in Kommission bei der C. H. Beck'schen Verlagsbuchhandlung München

Adresse der Deutschen Geodätischen Kommission:



Deutsche Geodätische Kommission

Alfons-Goppel-Straße 11 • D – 80 539 München

Telefon +49 – 89 – 23 031 1113 • Telefax +49 – 89 – 23 031 -1283 / - 1100

e-mail post@dgk.badw.de • <http://www.dgk.badw.de>

Prüfungskommission

Vorsitzender: Prof. Dr.-Ing. Jürgen Müller

Korreferenten: Prof. Dr.techn. Wolf-Dieter Schuh

Prof. Dr.-Ing. Christian Heipke

Tag der mündlichen Prüfung: 05.07.2016

© 2016 Deutsche Geodätische Kommission, München

Alle Rechte vorbehalten. Ohne Genehmigung der Herausgeber ist es auch nicht gestattet,
die Veröffentlichung oder Teile daraus auf photomechanischem Wege (Photokopie, Mikrokopie) zu vervielfältigen

ISSN 0065-5325

ISBN 978-3-7696-5189-8

Summary

An accurate model of the Earth's gravity field is beneficial for practical engineering and scientific applications, such as the unification of height systems, study of sea-level changes or understanding of dynamics of the Earth's interior. In order to improve the knowledge of the gravity field, the dedicated Gravity field and steady-state Ocean Circulation Explorer (GOCE) mission was realized by the European Space Agency (ESA). It was successfully operated from March 2009 to October 2013, and delivered hundreds of millions of observations in this period. In addition to Satellite-to-Satellite Tracking in high-low mode (SST-hl) for the long-wavelength part of the gravity field, the GOCE mission firstly applied Satellite Gravity Gradiometry (SGG) in space to measure the medium- and short-wavelength part. Hence, GOCE provided the great opportunity to recover a gravity field model that is accurate in the full wavelength spectrum down to 100 km spatial resolution.

To recover such a gravity field model, the SST-hl and SGG observations are analysed both separately and jointly. The SST-hl observations are processed with the acceleration approach which balances the satellite accelerations with the first-order derivatives of the gravitational potential, while the SGG observations are directly balanced with the second-order derivatives of the gravitational potential. The separate analysis of the two types of observations leads to two models that are accurate at complementary wavelengths, and the joint analysis gives the final model with high accuracy over the full spectrum up to a spherical harmonic degree 200.

The model determination, i.e., the estimation of the spherical harmonic coefficients, is based on the Least-Squares method. Because of the huge amount of observations and the large number of unknown coefficients, the above-mentioned procedure is a very challenging task with high computational complexity in both time and memory. Also, measurement errors, i.e., outliers, systematic errors and coloured noise, form a big challenge to obtain the best accuracy of the derived model. Moreover, the polar gaps have a severe effect on the zonal and near-zonal coefficients. These challenges have been coped with properly to derive a model with high quality. In addition, the performance of the recovered model is also affected by many other aspects such as the altitude of the satellite, the stochastic model of the observations and the amount of observations. All these issues are fully addressed in this dissertation and solutions are given to provide useful insight for future research.

With a self-developed software written in Fortran, the SST-hl and SGG observations are processed on the cluster system of Leibniz Universität IT Services (LUIS). In addition to two separate models that are accurate in complementary wavelength parts, four generations of combined gravity field models are derived from observations in four time spans (November 2009 - June 2010, November 2009 - April 2011, November 2009 - June 2012, November 2009 - October 2013). The geoid height errors of the four combined models up to a spherical harmonic degree 200 are 3.62, 3.23, 2.98 and 2.75 cm, respectively.

Keywords: GOCE, gravity field model, SST-hl, SGG, outlier, systematic error, coloured noise

Zusammenfassung

Ein genaues Modell des Erdschwerefeldes ist sowohl für ingenieurpraktische als auch wissenschaftliche Anwendungen von großem Interesse, wie z.B. bei der Untersuchung von Änderungen des Meeresspiegels, der Vereinheitlichung von Höhensystemen oder für das Verständnis der Dynamik des Erdinneren. Um die Kenntnisse über das Erdschwerefeld weiter zu verbessern, realisierte die European Space Agency (ESA) die GOCE (Gravity field and steady-state Ocean Circulation Explorer) Mission. GOCE umkreiste die Erde zwischen März 2009 und Oktober 2013 und lieferte in diesem Zeitraum hunderte Millionen von Daten. Neben dem Satellite-to-Satellite Tracking im high-low Modus (SST-hl) zur Bestimmung langwelliger Anteile, wurde bei der GOCE Mission erstmals die Satellitengradiometrie (Satellite Gravity Gradiometry, SGG) zur Bestimmung mittel- und kurzwelliger Anteile des Erdschwerefeldes genutzt. Damit eröffnete GOCE die großartige Möglichkeit, ein Schwerefeld zu bestimmen, das im gesamten Spektralbereich bis zur räumlichen Auflösung von 100 km hochgenaue Informationen enthält.

Zur Bestimmung eines solchen Schwerefeldmodells werden SST-hl und SGG Beobachtungen sowohl gemeinsam als auch getrennt voneinander analysiert. Die SST-hl Beobachtungen werden mit dem Beschleunigungs-Ansatz (acceleration approach) verarbeitet, bei dem die Satellitenbeschleunigungen mit den ersten Ableitungen des Gravitationspotentials verknüpft und ausgeglichen werden. Die SGG Beobachtungen werden über die direkte Verknüpfung zu den zweiten Ableitungen des Gravitationspotentials ausgeglichen. Die getrennte Analyse beider Beobachtungstypen liefert zwei Modelle, die in komplementären Frequenzbereichen genau sind. Die gemeinsame Analyse führt zum endgültigen Modell, das eine gute Genauigkeit über den gesamten Frequenzbereich bis zum sphärisch-harmonischen Grad 200 aufweist.

Die Modellbestimmung, also die Schätzung von sphärisch-harmonischen Koeffizienten, basiert auf der vermittelnden Ausgleichung nach der Methode der kleinsten Quadrate. Aufgrund der riesigen Anzahl an Beobachtungen und der großen Anzahl an unbekanntem Koeffizienten stellt das genannte Verfahren eine sehr anspruchsvolle Aufgabe mit hohem Rechenaufwand in puncto Zeit und Arbeitsspeicher dar. Darüber hinaus ist die Behandlung von Messfehlern, also Ausreißern, systematischen Fehlern und farbigem Rauschen eine große Herausforderung, um die höchste Genauigkeit des abgeleiteten Modells zu erhalten. Außerdem haben die Polarlöcher gravierende Auswirkungen auf die zonalen und nahen zonalen Koeffizienten. Die genannten Herausforderungen wurden zielgerichtet bearbeitet, um ein Modell mit guter Qualität zu bestimmen. Zusätzlich wird die Güte des abgeleiteten Modells auch durch viele andere Aspekte, wie beispielsweise die Höhe des Satelliten, das stochastische Modell der Beobachtungen und die Anzahl der Beobachtungen, beeinflusst. Alle diese Einflussfaktoren werden ausführlich in dieser Arbeit diskutiert, und es werden Lösungen präsentiert, um wertvolle Hinweise für zukünftige Forschungsarbeiten zu geben.

Mit einer selbstentwickelten Fortran-Software werden die SST-hl und SGG Beobachtungen auf dem Clustersystem des Leibniz Universität IT Services (LUIS) verarbeitet. Neben zwei separaten Modellen, die in komplementären Frequenzbereichen genau sind, werden vier Generationen

von kombinierten Schwerefeldmodellen abgeleitet, die sich in Bezug auf die Anzahl der eingeflossenen Beobachtungen unterscheiden (November 2009 - Juni 2010; November 2009 - April 2011; November 2009 - Juni 2012; November 2009 - Oktober 2013). Die Geoidhöhenfehler der vier kombinierten und bis zum sphärisch-harmonischen Grad 200 aufgelösten Modelle ergeben sich zu 3.62, 3.23, 2.98 und 2.75 cm.

Schlagwörter: GOCE, Schwerefeldmodell, SST-hl, SGG, Ausreißer, systematische Fehler, farbiges Rauschen

Contents

1	Introduction	1
1.1	Motivation	2
1.2	Aim and objectives	4
1.3	Outline of this work	5
2	Global gravity field recovery – theory	7
2.1	Gravitational field model and its derivatives	7
2.2	Least-Squares adjustment	12
2.2.1	Basis of LS adjustment	12
2.2.2	Design matrix	14
2.2.3	Normal matrix	15
2.2.4	Variance/covariance matrix	16
2.3	Parameter pre-elimination technique	17
2.4	Regularization	19
2.5	Data combination	20
2.6	Validation of the gravitational field model	21
2.6.1	Validation in the spectral domain	21
2.6.2	Validation in the space domain	23
2.6.3	Validation by GPS leveling	24
3	Global gravity field recovery from GOCE SST-hl Data	25
3.1	Background of SST-hl technique and related work	25
3.1.1	SST-hl technique	25
3.1.2	Related work	27

3.2	Acceleration approach	30
3.2.1	Theory of the acceleration approach	30
3.2.2	Workflow to process the GOCE SST-hl data	31
3.3	Data usage	32
3.4	Data pre-processing	34
3.4.1	Outlier detection	34
3.4.2	Down-sampling	36
3.4.3	Numerical differentiation	38
3.4.4	Temporal corrections	39
3.5	Data processing	42
3.6	Result Analysis	46
4	Global gravity field recovery from GOCE SGG data	49
4.1	Technique background and related work	49
4.1.1	Introduction to gradiometry	50
4.1.2	Electrostatic Gravity Gradiometer	51
4.1.3	Overview of the recovering approaches for SGG data	53
4.2	The workflow of gravity field recovery from SGG data	55
4.3	Data understanding	57
4.3.1	Data description	57
4.3.2	Properties of the gravity gradients	58
4.3.3	Noise behaviour of the gravity gradients	62
4.4	Pre-processing of the gravity gradients	65
4.4.1	Removal of anomalous observations	65
4.4.2	Detection of outliers	66
4.4.3	Examination of big data gaps	67

4.5	Model recovery	68
4.5.1	Functional model	68
4.5.2	The main steps of model recovery	70
4.5.3	Technical challenges	71
4.6	Result Analysis	73
4.6.1	Effect of model configurations	73
4.6.2	Contribution of each component	76
4.6.3	Results from different amounts of observations	81
4.6.4	Analysis of the gravity gradients at the lowered orbit	81
4.6.5	Final models from only gravity gradients	87
5	Combined gravity field models using all GOCE observations	91
5.1	Combined analysis of different data groups	91
5.2	Evaluation of the IFE models	92
5.2.1	Internal evaluation of the IFE models	93
5.2.2	External evaluation of the IFE models in the frequency domain	96
5.2.3	External evaluation of the IFE models in the space domain	101
6	Conclusions and outlook	105
6.1	Conclusions	105
6.2	Outlook	107
	Appendix A Temporal corrections	109
A.1	Direct tides	109
A.2	Solid Earth tides	110
A.3	Ocean tides	112
A.4	Solid Earth pole tides	113
A.5	Ocean pole tides	114

Bibliography	115
List of Figures	123
List of Tables	127
List of Abbreviations	129
Curriculum Vitae	131
Acknowledgements	133

Chapter 1

Introduction

Gravity is a fundamental force of nature that is responsible for many dynamic processes in the Earth's interior, on and above its surface. The determination of the gravity field thus plays an important role in Earth's science. On the Earth's surface, gravity is the resultant of gravitational force and the centrifugal force due to Earth's rotation. Since the contribution of the centrifugal force is analytical and easy to be computed, the Earth's gravity field determination is commonly referred to the gravitational field determination.

According to Newton's law of gravitation, each celestial body generates its own gravitational field. Assuming a spherically symmetrical body, the strength of the gravitational field at a given point is determined by the body's mass and the distance to the center of the body. Hence, supposing that the Earth is spherically symmetrical, the strength of the gravitational field on the Earth's surface would be constant. In reality, however, this value varies significantly from place to place due to the irregular shape and the heterogeneous mass distribution of the Earth. Instead of a perfect sphere, the shape of the Earth is roughly a slightly flattened ellipsoid with lumpy topography. More specifically, the Earth's radius is 21 km larger at the equator than at the poles, and the height difference between the high mountains and the deep ocean valleys reaches nearly 20 km. In addition, the density of the materials that make up the different layers of the Earth also varies, which further increases the heterogeneity of the gravitational field.

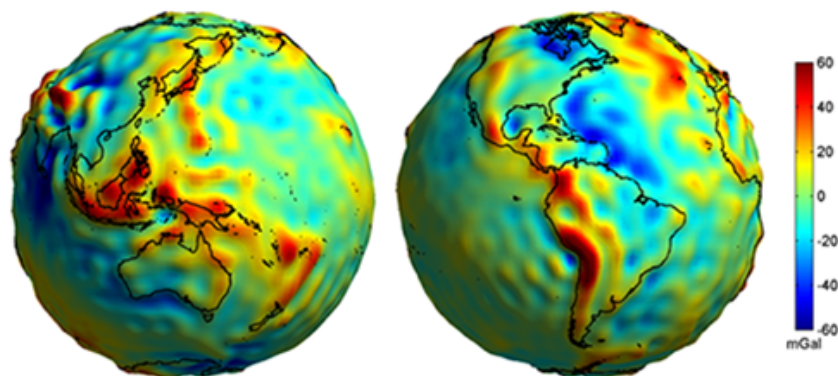


Figure 1.1: Gravity anomalies computed from GOCO03s, showing deviations from the theoretical gravity of an idealized smooth Earth, the so-called earth ellipsoid

An accurate model of the Earth's gravity field is essential for many Earth sciences. On the one hand, gravity anomalies (deviations between the actual field and an idealised Earth body) actually reflect the mass imbalance and dynamics of the Earth's interior. Thus, an accurate gravity field model of the Earth can contribute to a better understanding of geophysical and geodynamical processes, thereby benefiting research on plate tectonics, geological phenomena such as volcanoes and earthquakes, and many more. On the other hand, the geoid (i.e. the equipotential surface at mean sea-level of a hypothetical ocean at rest) which serves as vertical reference surface for any topographic features is completely based on the gravity field model. Hence, an accurate gravity field model will lead to an accurate geoid as well. The accuracy of the geoid is crucial for cases involving small height differences such as in engineering geodesy, or in studies of ice motion, sea-level change, ocean circulation, etc., ([Rummel et al., 2002](#); [Johannessen et al., 2003](#)).

In order to obtain the Earth's gravity field signal, the European Space Agency (ESA) launched the satellite mission Gravity field and steady-state Ocean Circulation Explorer (GOCE) on March 17, 2009. The GOCE mission enables the mapping of the static Earth's gravity field in an unprecedented detail. In this context, this dissertation aims to derive an accurate and precise global gravity field model of the Earth from the GOCE observations, thereby contributing to the multiple related research fields. The following sections outline the research motivation, objectives as well as the structure of this dissertation, intending to draw a clear overall picture of this research.

1.1 Motivation

Despite the consensus that an accurate global gravity field model is necessary for many Earth sciences, the current gravity field models that are derived from various observing techniques still have limitations from different perspectives. Before the launch of the dedicated satellite gravity missions starting in 2000, the gravity field models were mainly determined from terrestrial gravimetry, satellite altimetry and satellite tracking observations, and the recovered models were limited in terms of accuracy and resolution due to the limitation of their corresponding observation types. For example, the terrestrial data suffer from insufficient coverage due to operational or political reasons, and have limited accuracy in many parts of the world. Similarly, satellite altimetry provides accurate information only for the ocean regions, while satellite tracking observations are only sensitive to the very long-wavelength part of the gravity field. With such kinds of "flawed" observations, only limited improvements of the recovered model could be expected with some advanced processing procedures.

Therefore, new observation concepts were required in order to obtain an accurate global gravity field model. The new technology should be able to produce observations that can cover the complete range of the gravity field spectrum down to a short wavelength, and data should be collected all over the Earth. This led to the development of dedicated satellite gravity missions where the gravity sensor (the spacecraft) is installed in a nearly polar orbit at an altitude that is low enough to sense gravity field signals down to short wavelengths and to cover the entire planet within a reasonable time period.

In 2000, the era of dedicated satellite gravity mission began with the launch of the Challenging Minisatellite Payload (CHAMP) satellite (Reigber et al., 2002). CHAMP was operated in a decaying polar orbit with an altitude of about 450 km in the beginning, and the technique of Satellite-to-Satellite tracking in high-low (SST-hl) mode with the Global Navigation Satellite System (GNSS) satellites as “high” counterpart, was firstly realized. The CHAMP mission provided homogeneous observations on a global scale, and led to an improvement of the long-wavelength gravity field with about one order of magnitude (Reigber et al., 2003). However, the nature of gravity attenuation with the altitude prohibited the attainment of high spatial resolution.

To highlight the effect of small-scale features, the idea of differentiation were conceived. Soon, the Satellite-to-Satellite tracking in low-low (SST-ll) mode was firstly applied in the Gravity Recovery And Climate Experiment (GRACE) mission (Tapley et al., 2004) which was launched in 2002. This mission consists of two satellites at the same altitude of about 500 km both in a decaying polar orbit, approximately 220 km apart. The two satellites track each other applying the K-band microwave ranging system and the relative motion between the two satellites is measured with high precision. The GRACE mission has been successfully operated for more than 14 years until now, and delivered millions of observations to the users. Thanks to the huge amount of observations, the best accuracy of the long- and medium-scale features of the Earth’s gravity field have been achieved with GRACE (Mayer-Gürr et al., 2010). However, due to the relatively high altitude and the configuration (repeat cycle) of the satellites, the spatial resolution of the GRACE mission is still limited.

To counteract the attenuation of the Earth’s gravity field with altitude, the Gravity field and steady-state Ocean Circulation Explorer (GOCE) mission was successfully realized in 2009 (Floborghagen et al., 2011). In addition to the adoption of the SST-hl technique for the long-wavelength signal, the GOCE mission also applied gradiometry (differential accelerometry) to improve the gravity field models in the medium- and high-frequency part. The gradiometer on board of the GOCE satellite measures the second-order derivatives of the Earth’s gravitational potential so that the gravity field signals are actually amplified. Moreover, the satellite was

operated at an extremely low altitude of about 250 km which could be realized by a dedicated drag-free control system. The extremely low orbit increased the signal-to-noise ratio of the observations and helped to improve the spatial resolution. Thus, GOCE had the great potential to improve the gravity field in terms of both accuracy and spatial resolution. This dissertation works with the GOCE observations, aiming to derive an accurate (a few centimetres) global gravity field model of the Earth with high spatial resolution down to 80 km (corresponding to a spherical harmonic degree and order of 250) on the Earth's surface.

1.2 Aim and objectives

The aim of this dissertation is to recover a global gravity field model of the Earth with high accuracy and high spatial resolution from the GOCE observations.

During the entire lifetime of the GOCE mission, the GOCE satellite has returned hundreds of millions of observations. However, recovering a high-accuracy and high-resolution global gravity field model of the Earth from the GOCE observations is still a challenging task. The challenges come from several aspects. First, the huge amount of GOCE observations imposes big efforts in terms of numerical computation. Second, the measurement errors contained in the GOCE observations could damage the quality of the recovered gravity field models and have to be properly dealt with. Third, the polar gaps caused by the inclined orbit of the GOCE satellite have a severe influence on the zonal and near-zonal coefficients. In order to derive an adequate global gravity field model of the Earth, these challenges have to be properly handled.

Numerical computation The Earth's gravity field model is supposed to be described by tens of thousands of parameters, and these parameters are determined from the hundreds of millions of GOCE observations by Least-Squares (LS) adjustment. In the framework of the LS technique, the assembly and inversion of the normal matrix are the most challenging tasks in terms of computational complexity. For a model truncated at degree and order (d/o) 250, it would take hundreds of days on a single processing unit to assemble the normal matrix for one gravity gradient component, and a memory of about 30 GB to store the normal matrix. Hence, it is hardly feasible to perform the numerical computation on a personal computer. To cope with this challenge, the computation is carried out on the cluster system of Leibniz Universität IT Services (LUIS). In addition, some parallel computation strategy is applied to reduce the computing time, and the Rectangular Full Package format is used to save memory space.

Measurement errors The measurement errors in the GOCE observations include gross errors (outliers), systematic errors and random errors. They can cause severe problems for the recovered gravity field models if they are not properly handled. With the existence of system-

atic errors, the detection of outliers is especially challenging. The Observed-Minus-Computed (OMC) observations are used for outlier detection. To absorb systematic errors, the functional models are extended to introduce empirical parameters into each short orbit arc. To reduce the effect of random errors which present a typical coloured noise behaviour, the empirical variance/covariance matrix of the observations is constructed from the initial residuals and then used to de-correlate the observations.

Polar gap The GOCE mission leaves gaps with a radius of 6.5° in the polar regions, which severely affects the determination of the zonal and near-zonal coefficients (Sneeuw and van Gelderen, 1997). To handle this issue, some regularization is required. The regularization matrix is determined according to Kaula's rule, while the choice of the regularization parameter that balances the contribution of the observations and the constraints requires extra investigations.

1.3 Outline of this work

The two main types of GOCE observations, i.e., the SST-hl and the SGG observations, are sensitive to different wavelength parts of the Earth's gravity field signal. To obtain a model that has adequate accuracy over the full wavelength spectrum, the two types of observations are firstly used separately to recover two models that are accurate in different wavelength parts, and then combined together for the recovery of the final model. The processing steps form the main structure of this dissertation.

The dissertation starts, in Chapter 2, with the background of global gravity field modelling as well as the related theory and algorithms. Firstly, this chapter describes the representation of the gravitational field and its derivatives, as well as their transformation between different reference frames. This serves as basis to set up the functional models for the SST-hl and SGG data processing. Then, the classical LS technique is briefly reviewed. Considering the computational problem in the GOCE case, special emphasis is put on the theoretical analysis of the construction of the design matrix, normal matrix and the weight matrix, so that the algorithms can be optimised for the computation. Further, the functional model is extended by adding empirical parameters to absorb the systematic errors in the observations, and the corresponding algorithm, namely the parameter pre-elimination technique, is described thereafter. In addition, the regularization issue is discussed to cope with the polar gaps and the joint inversion of different data types is addressed. Last but not the least, the strategy to validate the derived models is described.

Chapter 3 discusses the long-wavelength gravity field recovery from the SST-hl observations. Firstly, the theory of the acceleration approach which is employed in this dissertation is introduced. Then, the pre-processing of the SST-hl data is discussed in detail, which includes the outlier detection for the kinematic orbit data, the numerical differentiation algorithm, the sophisticated down-sampling filters as well as the temporal corrections. With the “clean” input, a GOCE-only long-wavelength gravity field model is derived. The model is then validated in the frequency and space domains.

Chapter 4 discusses the global gravity field recovery from the SGG observations which is sensitive to the medium- and short-wavelength part of the gravity field. In the beginning of this chapter, the background and related work of the GOCE SGG data analysis are briefly summarized. In the following, the SGG observations are analysed in the time, space and frequency domains in order to achieve a thorough understanding of this new observation type. Then, the pre-processing steps are described, which include the removal of the anomalous observations, the detection of the outliers, and the examination of the data gaps. Thereafter, the processing details are addressed, including the functional model and the computational issues in terms of time and memory. Afterwards, the derived models are analysed to reveal the effects of the model configuration (length of the arc, sampling interval, contribution of the VCMs), each single gradient component, data volume as well as the orbit altitude. Finally, the models that are purely derived from the gravity gradients are validated.

The combined analysis of SST-hl and SGG data is discussed in Chapter 5. The Variance Component Estimation (VCE) approach is employed to derive the final gravity field model which covers the full spectrum down to a spatial resolution of 80 km. The derived models reflect four generations depending on different observation time spans. The four generations’ models are validated internally and externally in both the frequency and space domains.

Finally, the results and findings of this research are summarised in Chapter 6, where also directions for potential future work in global gravity field recovery are identified.

Chapter 2

Global gravity field recovery – theory

This chapter introduces the theoretical background and techniques for global gravity field recovery. To start with, section 2.1 covers the base functions, i.e., the representations of the gravitational field and its derivatives, and their transformation between different reference frames. Together they provide the knowledge required to set up the functional model for gravity field recovery. The GOCE mission has provided a huge amount of observations to generate gravity field solutions, while it also poses challenges in several ways. First, the huge amount of observations and large number of unknown parameters form a large-scale linear equation system, which poses a great numerical challenge to derive the solution. Also, the observations contain unknown systematic errors and polar gaps, which affect the final solution. Moreover, different types of observations have to be analysed in a combined way. To cope with these challenges, section 2.2 explains the Least-Squares (LS) technique to work with this large-scale linear equation system. Considering the complicated case for GOCE, special emphasis is put on the theoretical analysis of the construction of the design matrix, normal matrix and weight matrix so that the algorithms can be optimised for the computation. Section 2.3 discusses an approach to introduce empirical parameters to the functional model to absorb the systematic errors, while section 2.4 addresses the regularization strategy to stabilize the solution of the ill-posed problem caused by the polar gaps. Section 2.5 presents the Variance Component Estimation (VCE) approach for a combined analysis of different observations types. Finally, the strategy to validate the derived model is addressed in section 2.6.

2.1 Gravitational field model and its derivatives

The gravitational potential V is a harmonic function outside the Earth's surface that satisfies the Laplace's equation. As a solution to the Laplace's equation in the spherical coordinate system, the gravitational potential V can be represented in a harmonic series (Hofmann-Wellenhof and Moritz, 2006) as

$$V(r, \theta, \lambda) = \frac{GM}{R} \sum_{n=0}^{\infty} \left(\frac{R}{r}\right)^{n+1} \sum_{m=0}^n [\bar{C}_{nm} \cos m\lambda + \bar{S}_{nm} \sin m\lambda] \bar{P}_{nm}(\cos \theta), \quad (2.1)$$

where GM is the gravitational constant of the Earth, R is the equatorial radius of the Earth reference ellipsoid, (r, θ, λ) are the spherical coordinates of a point on the Earth surface (r radius, θ co-latitude, λ longitude), n, m denote spherical harmonic degree and order, $\bar{P}_{nm}(\cos \theta)$ are the fully normalized associated Legendre functions, and $\bar{C}_{nm}, \bar{S}_{nm}$ are the normalized Spherical Harmonic (SH) coefficients which are the unknowns of the gravity field solution.

This dissertation aims to estimate the SH coefficients from satellite gravimetric observations, e.g., gravity gradients. This process is known as *spherical harmonic analysis* (Colombo, 1981; Koop, 1993). In practice, the infinite series expansion is usually truncated at a certain resolvable degree N_{max} . On the one hand, the value of N_{max} determines the spatial resolution D of the recovered gravity field model ($D = 20000/N_{max}$, half-wavelength given in km), cf. Johannessen et al. (2003), and a larger N_{max} can reveal more details of the gravitational field. N_{max} is also constrained by the data type. On the other hand, N_{max} determines the number of coefficients to be estimated by $(N_{max} + 3)(N_{max} - 1)$ ¹ and thus impacts the computational burden. Hence, the determination of N_{max} should be a balance between benefits and costs.

Reversely, using a set of known potential coefficients, e.g., from a reference gravity field model, the gravitational potential V can be calculated following Eq. (2.1). This is referred as *spherical harmonic synthesis* (Colombo, 1981; Koop, 1993). With a slight modification to Eq. (2.1), the spherical harmonic synthesis does not only give the gravitational potential but also many other gravity-related quantities such as gravitational accelerations and the gravity gradients, see Eq. (2.2). For example, an a priori signal that has to be subtracted from the original gravimetric observations in the LS adjustment can be modelled from the known highly accurate SH coefficients.

However, the gravitational potential V is not directly measurable. In practice, one often observes gravitational accelerations or gravity gradients² as alternatives. They correspond to the first- and second-order partial derivatives of the gravitational potential V . In a similar way, gravitational accelerations and gravity gradients can be expressed in a spherical harmonic series by substituting the symbols γ, p, α, β with the corresponding expressions from Table 2.1 (Koop, 1993; Wermuth, 2008),

$$V_{ij} = \frac{GM}{R} \sum_{n=0}^{N_{max}} \gamma \left(\frac{R}{r}\right)^{n+1} \sum_{m=0}^n p [\alpha \cos m\lambda + \beta \sin m\lambda]. \quad (2.2)$$

¹The number of the coefficients to be estimated is $(N_{max} + 1)^2$, which excludes the coefficients \bar{S}_{n0} as their values are 0. In addition, \bar{C}_{00} is usually fixed to 1 and $\bar{C}_{10}, \bar{C}_{11}, \bar{S}_{11}$ are 0 in the case that the origin of the coordinate system coincides with the center of mass of the Earth. Then the total number becomes $(N_{max} + 3)(N_{max} - 1)$.

²The term “gravity gradients” is widely used in literature “instead of “gravitational gradients”, even if the centrifugal contribution caused by Earth’s rotation is not present, e.g., in space. This terminology is also used in this dissertation.

Table 2.1: Expressions of the symbols γ, p, α, β in Eq. (2.2) are given. $\bar{P}'_{nm}, \bar{P}''_{nm}$ denote the first- and second-order derivatives of the Legendre functions w.r.t. θ .

differentiation w.r.t.	γ	p	α	β
r	$-\frac{(n+1)}{r}$	\bar{P}_{nm}	\bar{C}_{nm}	\bar{S}_{nm}
θ	1	\bar{P}'_{nm}	\bar{C}_{nm}	\bar{S}_{nm}
λ	1	$m\bar{P}_{nm}$	\bar{S}_{nm}	$-\bar{C}_{nm}$
rr	$\frac{(n+1)(n+2)}{r^2}$	\bar{P}_{nm}	\bar{C}_{nm}	\bar{S}_{nm}
$r\theta$	$-\frac{(n+1)}{r}$	\bar{P}'_{nm}	\bar{C}_{nm}	\bar{S}_{nm}
$r\lambda$	$-\frac{(n+1)}{r}$	$m\bar{P}_{nm}$	\bar{S}_{nm}	$-\bar{C}_{nm}$
$\theta\theta$	1	\bar{P}''_{nm}	\bar{C}_{nm}	\bar{S}_{nm}
$\theta\lambda$	1	$m\bar{P}'_{nm}$	\bar{S}_{nm}	$-\bar{C}_{nm}$
$\lambda\lambda$	-1	$m^2\bar{P}_{nm}$	\bar{C}_{nm}	\bar{S}_{nm}

Although modelled in a spherical coordinate system, the gravitational accelerations and the gravity gradients are actually measured in a Cartesian coordinate system. Also, the practical work of gravity field recovery involves multiple Cartesian coordinate systems. Hence, the transformations between the spherical coordinate system and Cartesian coordinate systems as well as among different Cartesian coordinate systems are required. For more details about the transformations between different coordinate systems, the reader is referred to (Koop, 1993). For the transformations between the spherical coordinate system and Cartesian coordinate systems, the potential derivatives with respect to the Local North-Oriented reference Frame (LNOF) are firstly derived. LNOF is a right-handed North-West-Up frame with the X-axis pointing North, the Y-axis pointing West and the Z-axis Up (EGG-C, 2014). In the following, the transformation between LNOF and the spherical coordinate system is given in Eq. (2.3) and Eq. (2.4) for gravitational accelerations and gravity gradients, respectively.

For the gravitational acceleration components in three directions x, y, z of LNOF (for convenience, V_i is written for $\frac{\partial V}{\partial i}$), one has

$$\begin{aligned} V_x &= -\frac{1}{r}V_\theta, \\ V_y &= -\frac{1}{r \sin \theta}V_\lambda, \\ V_z &= V_r. \end{aligned} \tag{2.3}$$

And for the gravity gradients V_{ij} in the LNOF (similarly, V_{ij} is written for $\frac{\partial^2 V}{\partial i \partial j}$), it reads:

$$\begin{aligned} V_{xx} &= \frac{1}{r}V_r + \frac{1}{r^2}V_{\theta\theta}, \\ V_{xy} &= \frac{\cos \theta}{r^2 \sin^2 \theta}V_\lambda - \frac{1}{r^2 \sin \theta}V_{\lambda\theta}, \\ V_{xz} &= \frac{1}{r^2}V_\theta - \frac{1}{r}V_{r\theta}, \\ V_{yy} &= \frac{1}{r}V_r + \frac{1}{r^2 \tan \theta}V_\theta + \frac{1}{r^2 \sin^2 \theta}V_{\lambda\lambda}, \\ V_{yz} &= \frac{1}{r \sin \theta}V_{r\lambda} - \frac{1}{r^2 \sin \theta}V_\lambda, \\ V_{zz} &= V_{rr}. \end{aligned} \tag{2.4}$$

Eq. (2.3) and (2.4) make it possible to transform gravitational accelerations and gravity gradients from the spherical coordinate system to a Cartesian coordinate system, i.e., LNOF. In practice however, instead of LNOF, GOCE observations are delivered in other Cartesian coordinate systems, such as the Earth-fixed Reference Frame (ERF, for the orbit) and the Gradiometer Reference Frame (GRF, for gravity gradients). ERF is an orthogonal, right-handed frame with the Z-axis pointing towards the North pole and the X-axis fixed in the equatorial plain in direction to the Greenwich meridian, while GRF is an instrumental three-axis coordinate system in which the gravity gradients are observed (EGG-C, 2014). Thus, the transformation among different Cartesian coordinate systems are required.

The gravitational acceleration components constitute a vector, $\mathbf{a} = [V_x \ V_y \ V_z]^T$. It can be transformed between different Cartesian coordinate systems according to

$$\mathbf{a}_{F2} = R_{F1}^{F2} \mathbf{a}_{F1}, \tag{2.5}$$

where \mathbf{a}_{F1} , \mathbf{a}_{F2} represent the gravitational accelerations in the frames $F1$ and $F2$; and R_{F1}^{F2} is the rotation matrix with dimension of 3×3 from $F1$ to $F2$.

The rotation matrix can be obtained in two ways. First, it can be presented as a product of three basic rotation (also called elemental rotation) matrices as

$$R = R_z(\gamma)R_y(\beta)R_x(\alpha), \quad (2.6)$$

$R_z(\gamma)$, $R_y(\beta)$, $R_x(\alpha)$ represent an extrinsic rotation of which the Euler angles α , β , γ are about the axes x , y , z , respectively. For instance, the rotation matrix from LNOF to ERF can be constructed as follows (EGG-C, 2014)

$$R_{LNOF}^{ERF} = \begin{pmatrix} -\cos\theta \cos\lambda & \sin\lambda & \sin\theta \cos\lambda \\ -\cos\theta \sin\lambda & -\cos\lambda & \sin\theta \sin\lambda \\ \sin\theta & 0 & \cos\theta \end{pmatrix}, \quad (2.7)$$

where θ co-latitude and λ longitude of the spacecraft center of mass in ERF.

Alternatively, the rotation information can be obtained with a unit quaternion which provides a convenient mathematical notation for representing an orientation or rotation of objects in three dimensions. In such manner, the rotation matrix is computed as (EGG-C, 2014)

$$R = \begin{pmatrix} q_0^2 + q_1^2 - q_2^2 - q_3^2 & 2(q_1q_2 - q_3q_0) & 2(q_1q_3 + q_2q_0) \\ 2(q_1q_2 + q_3q_0) & q_0^2 - q_1^2 + q_2^2 - q_3^2 & 2(q_2q_3 - q_1q_0) \\ 2(q_1q_3 - q_2q_0) & 2(q_2q_3 + q_1q_0) & q_0^2 - q_1^2 - q_2^2 + q_3^2 \end{pmatrix}, \quad (2.8)$$

where (q_0, q_1, q_2, q_3) are the elements of a unit quaternion.

The transformation of gravity gradients is similar, except that the rotation has to be applied twice since the gravity gradients constitute a tensor Γ . More details on the gravity gradient tensor are given in Section 4.1. Thus, the transformation of the gradient tensor is written as

$$\Gamma_{F2} = R_{F1}^{F2} \Gamma_{F1} (R_{F1}^{F2})^T, \quad (2.9)$$

where the gravity gradient tensors in frame $F1$ and $F2$ are labelled as Γ_{F1} and Γ_{F2} , R_{F1}^{F2} represents the rotation matrix, it is the same as that in Eq. (2.5).

The explained knowledge of the base functions as well as the transformations between different coordinate systems are the building blocks of global gravity field recovery. With them, the functional models that balance the measurements and the unknown SH coefficients can be set up for further analysis.

2.2 Least-Squares adjustment

Modern satellite technology has provided a huge amount of observations to recover a detailed and accurate Earth's gravity field model that is represented by tens of thousands of parameters. The huge amount of observations and large number of parameters form a large-scale and over-determined linear equation system. The Least-Squares (LS) technique is employed to solve this large-scale linear system, which poses a great numerical challenge. This section will first briefly introduce the LS adjustment, and then put special emphasis on the construction of the design matrix, normal matrix and weight matrix in order to achieve optimised algorithms for the computations in the GOCE case.

2.2.1 Basis of LS adjustment

For a linear equation system, the functional model that expresses the measurements as a function of the unknown parameters can be represented as

$$l + v = Ax, \quad (2.10)$$

where l is the vector of observations, v represents observation residuals, A is the design matrix and x is the vector of unknown parameters. And the stochastic model that describes the accuracy and correlation of the measurements is represented by a full Variance/Covariance Matrix (VCM) Σ_u . It reads

$$\Sigma_u = \begin{bmatrix} \sigma_1^2 & \sigma_{12} & \cdots & \sigma_{1n} \\ \sigma_{21} & \sigma_2^2 & \cdots & \sigma_{2n} \\ \vdots & \vdots & \ddots & \vdots \\ \sigma_{n1} & \sigma_{n2} & \cdots & \sigma_n^2 \end{bmatrix}, \quad (2.11)$$

where σ_i^2 is the variance of the i^{th} measurement; σ_{ij} is the covariance between the i^{th} and j^{th} measurement.

According to the rule of LS adjustment that minimize the sum of squares of the weighted residuals, the solution \hat{x} is estimated by (Koch, 1999)

$$\hat{x} = (A^T P A)^{-1} A^T P l = N^{-1} W, \quad (2.12)$$

where $P = \Sigma_u^{-1}$ is the weight matrix, $N = A^T P A$ is called the normal matrix, and $W = A^T P l$ the right hand side of the normal equation $Nx = W$. The normal matrix N is independent of the observations since the observations only enter the computation of matrix W . In fact, N is only determined by the inner geometry of the data distribution. Hence, its in-

verse \mathbf{N}^{-1} is useful in detecting an ill-posed data distribution for the estimation of unknown parameters.

In addition to the estimated parameters $\hat{\mathbf{x}}$, the residuals $\hat{\mathbf{v}}$ after the adjustment

$$\hat{\mathbf{v}} = \mathbf{A}\hat{\mathbf{x}} - \mathbf{l} \quad (2.13)$$

have to be computed. Analysing the residuals is a useful tool to assess the quality of the observations. First, the residuals are taken as approximations of the errors so that they can be used to detect outliers in the observations. Then, a Power Spectral Density (PSD) of the residuals can reveal the spectral behaviour of the measurement error. Furthermore, the empirical VCM is computed from the residuals when a priori information of the stochastic model is not available. The residuals are also used to calculate the posterior variance of unit weight $\hat{\sigma}_0^2$ which is a measure of the quality of the solution. In theory, it is computed from the residuals by

$$\hat{\sigma}_0^2 = \frac{\hat{\mathbf{v}}^T \mathbf{P} \hat{\mathbf{v}}}{s - r}, \quad (2.14)$$

where s, r are the number of observations and parameters. In practice, however, the large amount of observations would form a rather large design matrix \mathbf{A} . The matrix can become so large that it cannot be stored in memory after the adjustment. To avoid a recomputation, instead of Eq. (2.14), $\hat{\sigma}_0^2$ is actually estimated by

$$\hat{\sigma}_0^2 = \frac{\mathbf{l}^T \mathbf{P} \mathbf{l} - \mathbf{W}^T \hat{\mathbf{x}}}{s - r}. \quad (2.15)$$

The variance/covariance matrix of the coefficients $\Sigma_{\hat{\mathbf{x}}\hat{\mathbf{x}}}$ is computed by

$$\Sigma_{\hat{\mathbf{x}}\hat{\mathbf{x}}} = \hat{\sigma}_0^2 \mathbf{N}^{-1}. \quad (2.16)$$

The square roots of the diagonal of $\Sigma_{\hat{\mathbf{x}}\hat{\mathbf{x}}}$ give the standard deviation (formal errors) of the estimated parameters $\hat{\mathbf{x}}$. Such information is of crucial significance for further use of the model coefficients in terms of error propagation.

The above gives the theory and basic equations of LS adjustment. However, when applying them to the GOCE data, one might come across many issues that are caused by the huge amount of observations and the large number of parameters. These issues will be discussed in the following subsections.

2.2.2 Design matrix

The dimension of the design matrix \mathbf{A} is $s \times r$, where s and r represent the number of the observations and the estimated parameters, respectively. In the context of GOCE data, s reaches hundreds of millions for one gradient component while r equals $(N_{max} - 1)(N_{max} + 3)$ as explained in the beginning of Section 2.1. Specifically, a gravity field model truncated at d/o 250 has $r = 62,997$ unknown parameters. Therefore, the design matrix \mathbf{A} stored in a double-precision floating format would require a memory space of more than 50 Terabyte (TB). This is a large storage challenge even to super computers.

One strategy to handle this challenge is storing the much smaller normal matrix \mathbf{N} instead of \mathbf{A} . This is often used for the recovery of the unknown parameters $\hat{\mathbf{x}}$, since the recovery of $\hat{\mathbf{x}}$ is based on the normal equation system. Another strategy is to store the complete matrix \mathbf{A} as a list of partitioned blocks \mathbf{A}_i , each of which corresponds to one segment of the entire observations. This is also convenient for parallel computation.

With these matrix blocks \mathbf{A}_i , the assembly of the normal matrix \mathbf{N} becomes (Anton, 2010)

$$\begin{aligned} \mathbf{N} = \mathbf{A}^T \mathbf{P} \mathbf{A} &= \begin{bmatrix} \mathbf{A}_1^T & \mathbf{A}_2^T & \cdots & \mathbf{A}_n^T \end{bmatrix} \begin{bmatrix} \mathbf{P}_1 & 0 & \cdots & 0 \\ 0 & \mathbf{P}_2 & \cdots & 0 \\ \vdots & \vdots & \ddots & \vdots \\ 0 & 0 & \cdots & \mathbf{P}_n \end{bmatrix} \begin{bmatrix} \mathbf{A}_1 \\ \mathbf{A}_2 \\ \vdots \\ \mathbf{A}_n \end{bmatrix} \\ &= \mathbf{A}_1^T \mathbf{P}_1 \mathbf{A}_1 + \mathbf{A}_2^T \mathbf{P}_2 \mathbf{A}_2 + \cdots + \mathbf{A}_n^T \mathbf{P}_n \mathbf{A}_n \\ &= \mathbf{N}_1 + \mathbf{N}_2 + \cdots + \mathbf{N}_n \end{aligned} \quad (2.17)$$

and similarly,

$$\mathbf{W} = \mathbf{A}_1^T \mathbf{P}_1 \mathbf{l}_1 + \mathbf{A}_2^T \mathbf{P}_2 \mathbf{l}_2 + \cdots + \mathbf{A}_n^T \mathbf{P}_n \mathbf{l}_n = \mathbf{W}_1 + \mathbf{W}_2 + \cdots + \mathbf{W}_n. \quad (2.18)$$

Note that in Eq. (2.17), the correlations among each two observation segments are treated as 0. This is a simplification of the reality, and it can significantly simplify the calculation process.

Hence, the matrices \mathbf{N}_i and \mathbf{W}_i for each short segment of the observations can be separately assembled with efficient parallel computation. And then the complete matrices \mathbf{N} and \mathbf{W} can be obtained by summing up their respective partitioned blocks.

2.2.3 Normal matrix

The normal matrix \mathbf{N} plays an important role in LS adjustment. First, the unknown parameters can directly be solved based on the normal equation, thus the normal matrix must be assembled and stored. In addition, the inverse of the normal matrix is necessary to estimate the internal quality of the resolved parameters according to Eq. (2.16). Because of the huge number of observations and large number of unknowns, the assembly and inversion of the normal matrix are very numerically challenging. This section gives a theoretical analysis on the computational complexity of \mathbf{N} in terms of time and memory.

Assembling the normal matrix $\mathbf{N} = \mathbf{A}^T \mathbf{P} \mathbf{A}$ is the most time-consuming task. In the most simplified situation, when \mathbf{P} is a unit matrix, $\mathbf{N} = \mathbf{A}^T \mathbf{A}$. The time complexity for this matrix multiplication is $O(sr^2)$. As discussed in Section 2.2.2, s reaches hundreds of millions for the whole mission period, and r is 62,997 for a model truncated at d/o of 250. In a rough estimate, the assembly of the normal matrix for one gradient component would take more than 500 days on a single-core microprocessor with 10 Giga FLOPS (FLOating-point Operations Per Second, a measure of computer performance). Consequently, it is only feasible to first assemble the partitioned blocks \mathbf{N}_i on multiple processors and then retrieve the complete matrix from \mathbf{N}_i following Eq. (2.17). As each assembly of \mathbf{N}_i can be finished in a few hours (varying with the length of the data segment), this parallelism can significantly improve the computational efficiency. The parallel computation will be carried out on a cluster system, more details are given in Section 4.5.3.

Regarding the solving strategy of unknown parameters, there exist indirect and direct methods. The indirect method iteratively constructs a series of solution approximations until convergence is achieved. As representatives, the Preconditioned Conjugate Gradient Multiple Adjustment (PCGMA) is discussed in Schuh (1996) and the Least-Square method using QR decomposition (LSQR) is addressed in Baur (2009). By the indirect method, the assembly of the normal matrix can be avoided. In contrast, the direct approach determines the parameters by inversion of the normal matrix. This is also referred to as “brute-force” approach (Roth et al., 2012). A useful feature of the “brute-force” approach is that it can additionally provide the variance/covariance information of the estimated parameters. Therefore in this dissertation, the “brute-force” approach is applied.

With the “brute-force” approach, the estimation is done following three steps. First, decompose the normal matrix into the product of two triangular matrices, i.e., $\mathbf{N} = \mathbf{R}^T \mathbf{R}$, where \mathbf{R} is an upper triangular matrix. Among the various decomposition algorithms such as LU, QR, etc., the most efficient one to solve a symmetric and positive definite matrix (properties of \mathbf{N}) has been

known as the Cholesky decomposition. The time complexity of the decomposition is $O(\frac{1}{3}r^3)$, cf. Intel (2009), where r is the number of the parameters. Next, the parameters \boldsymbol{x} is solved by a straightforward process of backward or forward substitution, the complexity of which is $O(r^2)$ (Intel, 2009). Finally, the inversion of the normal matrix is calculated by $\boldsymbol{N}^{-1} = \boldsymbol{R}^{-1}(\boldsymbol{R}^{-1})^T$, and the corresponding complexity is $O(\frac{2}{3}r^3)$ (Intel, 2009). Hence, the total time complexity of solving the normal equation by Cholesky decomposition is $O(r^3)$. By a rough estimate, this calculation can be finished in a few of hours on a single-core processor.

Regarding the space complexity, a memory of more than 30 GigaByte (GB) is required to store the complete normal matrix. This is because the matrix has a dimension of $r \times r$, and r is 62,997 for a model truncated at d/o=250. However, the symmetric property of the normal matrix provides an opportunity to save space by storing only the upper or lower triangular part of the matrix. For this purpose, a Rectangular Full Package (RFP) scheme will be introduced in this dissertation, see Section 4.5.3.

2.2.4 Variance/covariance matrix

For independent observations with the same accuracy, their VCM $\boldsymbol{\Sigma}_{ll}$ will be a unit matrix and thus negligible in the LS adjustment. However, such premise is not valid for GOCE observations. Because of the widely accepted fact that the errors of the gravity gradients are highly correlated, the VCM of GOCE observations is a full matrix which must be taken into consideration. Consequently, the computation complexity is significantly increased for two main reasons. First, the direct storage is impractical because the dimension of VCM is $s \times s$, with the number of observations s being hundreds of millions. Second, it implies an additional operation of matrix multiplication to assemble the normal matrix. In this regard, a decorrelation algorithm (Schuh, 2003) is introduced to avoid the direct multiplication of \boldsymbol{A} and $\boldsymbol{\Sigma}_{ll}$.

As the VCM is symmetric and positive definite, it can be decomposed by the Cholesky approach into

$$\boldsymbol{\Sigma}_{ll} = \boldsymbol{F}\boldsymbol{F}^T, \quad (2.19)$$

where \boldsymbol{F} is a lower triangular matrix. Substituting Eq. (2.19) into the assembly of the normal matrix, one gets

$$\boldsymbol{N} = \boldsymbol{A}^T \boldsymbol{P} \boldsymbol{A} = \boldsymbol{A}^T \sigma_0^2 \boldsymbol{\Sigma}^{-1} \boldsymbol{A} = \sigma_0^2 \boldsymbol{A}^T (\boldsymbol{F}\boldsymbol{F}^T)^{-1} \boldsymbol{A} = \sigma_0^2 (\boldsymbol{F}^{-1} \boldsymbol{A})^T (\boldsymbol{F}^{-1} \boldsymbol{A}). \quad (2.20)$$

Define

$$\bar{\boldsymbol{A}} = \boldsymbol{F}^{-1} \boldsymbol{A}, \quad (2.21)$$

then Eq. (2.20) can be written as

$$\mathbf{N} = \sigma_0^2 \bar{\mathbf{A}}^T \bar{\mathbf{A}}. \quad (2.22)$$

Similarly, the vector \mathbf{W} can be rewritten as

$$\mathbf{W} = \mathbf{A}^T \mathbf{P} \mathbf{l} = \sigma_0^2 \mathbf{A}^T (\mathbf{F}^{-1})^T \mathbf{F}^{-1} \mathbf{l} = \sigma_0^2 (\mathbf{F}^{-1} \mathbf{A})^T (\mathbf{F}^{-1} \mathbf{l}) = \sigma_0^2 \bar{\mathbf{A}}^T \bar{\mathbf{l}}, \quad (2.23)$$

where $\bar{\mathbf{l}} = \mathbf{F}^{-1} \mathbf{l}$. Thus, before assembling of the normal matrix, the design matrix \mathbf{A} and the observation vector \mathbf{l} are multiplied by the matrix \mathbf{F}^{-1} which can be interpreted as a de-correlated filter process (Schuh, 2003; Pail, 2014). Finally, the solution of the parameters $\hat{\mathbf{x}}$ is derived by

$$\hat{\mathbf{x}} = \mathbf{N}^{-1} \mathbf{W} = (\sigma_0^2 \bar{\mathbf{A}}^T \bar{\mathbf{A}})^{-1} (\sigma_0^2 \bar{\mathbf{A}}^T \bar{\mathbf{l}}) = (\bar{\mathbf{A}}^T \bar{\mathbf{A}})^{-1} \bar{\mathbf{A}}^T \bar{\mathbf{l}}. \quad (2.24)$$

In this dissertation the de-correlated filter \mathbf{F} is computed by the Cholesky decomposition of the VCM Σ_{ll} , and an empirical Σ_{ll} can be estimated from the observation residuals (see Section 4.3.3) if the true Σ_{ll} is not available. One can also find other methods to design the de-correlated filter \mathbf{F} , such as the inverse Fourier transform of the PSD of the residuals, or digital recursive filters like the Auto-Regressive Moving Average (ARMA) filter in the time domain (Kusche and Klees, 2002; Schuh, 2003; Siemes, 2008; Pail, 2014). Nevertheless, all these methods are supposed to obtain similar de-correlated filters.

2.3 Parameter pre-elimination technique

The previous section described the classical LS adjustment that works well under the condition that only stochastic errors exist in the observations. But it does not hold true for the GOCE case. Thus, systematic errors existing in the GOCE orbit and gravity gradient data call for special treatment when applying the LS adjustment. In this regard, the functional model is extended by adding additional parameters to absorb such systematic errors. In contrast to the estimated spherical harmonic coefficients which are commonly named as the aimed parameters or global parameters, these additional parameters are often referred to as empirical parameters or local parameters. Adding empirical parameters into the functional model Eq. (2.10), one will obtain

$$\mathbf{l} + \mathbf{v} = \mathbf{A}_1 \mathbf{x}_1 + \mathbf{A}_2 \mathbf{x}_2, \quad (2.25)$$

where \mathbf{x}_1 represents the aimed parameters and \mathbf{A}_1 the corresponding design matrix, \mathbf{x}_2 , \mathbf{A}_2 are empirical parameters and their design matrix. By LS adjustment, the assembly of the normal

matrix \mathbf{N} is written as

$$\begin{aligned} \mathbf{N} &= \begin{bmatrix} \mathbf{A}_1 & \mathbf{A}_2 \end{bmatrix}^T \mathbf{P} \begin{bmatrix} \mathbf{A}_1 & \mathbf{A}_2 \end{bmatrix} \\ &= \begin{bmatrix} \mathbf{A}_1^T \mathbf{P} \mathbf{A}_1 & \mathbf{A}_1^T \mathbf{P} \mathbf{A}_2 \\ \mathbf{A}_2^T \mathbf{P} \mathbf{A}_1 & \mathbf{A}_2^T \mathbf{P} \mathbf{A}_2 \end{bmatrix} = \begin{bmatrix} \mathbf{N}_{11} & \mathbf{N}_{12} \\ \mathbf{N}_{21} & \mathbf{N}_{22} \end{bmatrix}, \end{aligned} \quad (2.26)$$

and the right-hand side of the system of normal equations \mathbf{W} is written as

$$\mathbf{W} = \begin{bmatrix} \mathbf{A}_1 & \mathbf{A}_2 \end{bmatrix}^T \mathbf{P} \mathbf{l} = \begin{bmatrix} \mathbf{A}_1^T \mathbf{P} \mathbf{l} \\ \mathbf{A}_2^T \mathbf{P} \mathbf{l} \end{bmatrix} = \begin{bmatrix} \mathbf{W}_{11} \\ \mathbf{W}_{12} \end{bmatrix}. \quad (2.27)$$

With the included empirical parameters, the dimension of the normal matrix \mathbf{N} becomes $(r + p) \times (r + p)$, where r, p are the number of aimed coefficients and empirical parameters, respectively. In a long time span, the number of the empirical parameters may be more than the aimed coefficients. The more empirical parameters are included, the larger the dimension will be, and the more time and space it requires to solve the normal equations, as pointed out in Section 2.2.3.

Since these added empirical parameters are not of real interest for the final solution, here a specific algorithm named Parameter Pre-elimination Technique (Wermuth, 2008; Yi, 2012b) is applied to avoid having to work with the complete normal matrix \mathbf{N} . As the name suggests, this technique eliminates the empirical parameters from the normal equations before inversion. Rewriting the normal equations as

$$\begin{bmatrix} \mathbf{N}_{11} & \mathbf{N}_{12} \\ \mathbf{N}_{21} & \mathbf{N}_{22} \end{bmatrix} \begin{bmatrix} \mathbf{x}_1 \\ \mathbf{x}_2 \end{bmatrix} = \begin{bmatrix} \mathbf{W}_{11} \\ \mathbf{W}_{12} \end{bmatrix}, \quad (2.28)$$

one can solve the second equation of Eq. (2.28) for the empirical parameters \mathbf{x}_2 by

$$\mathbf{x}_2 = \mathbf{N}_{22}^{-1} \mathbf{W}_2 - \mathbf{N}_{22}^{-1} \mathbf{N}_{21} \mathbf{x}_1. \quad (2.29)$$

Substituting Eq. (2.29) into the first equation of Eq. (2.28), \mathbf{x}_1 is then solved by

$$\mathbf{x}_1 = (\mathbf{N}_{11} - \mathbf{N}_{12} \mathbf{N}_{22}^{-1} \mathbf{N}_{21})^{-1} (\mathbf{W}_1 - \mathbf{N}_{12} \mathbf{N}_{22}^{-1} \mathbf{W}_2). \quad (2.30)$$

Defining

$$\begin{aligned} \mathbf{N}^* &= \mathbf{N}_{11} - \mathbf{N}_{12} \mathbf{N}_{22}^{-1} \mathbf{N}_{21}, \\ \mathbf{W}^* &= \mathbf{W}_1 - \mathbf{N}_{12} \mathbf{N}_{22}^{-1} \mathbf{W}_2, \end{aligned} \quad (2.31)$$

the dimension of N^* is the same as N_{11} which is the normal matrix corresponding to the parameters x_1 . When x_1 is estimated from Eq. (2.30), the additional parameters x_2 can be computed by a back substitution of x_1 into Eq. (2.29).

2.4 Regularization

The GOCE satellite runs in a sun-synchronous orbit with an inclination of 96.5° , consequently it cannot cover the two polar regions. The absence of observations from the polar regions is called *polar gaps* (Sneeuw and van Gelderen, 1997), and it results in a distortion of the zonal and near-zonal coefficients and makes gravity field recovery an ill-posed problem.

One strategy to handle this problem is to fill in the gaps with other measurements (such as airborne gravity measurements and GRACE data, etc.), or with pseudo observations such as gravity anomalies that are computed from an a priori gravity field model (Yi, 2012b). One side effect of this strategy is that external information would be introduced.

An alternative strategy is to apply regularization to stabilize the solution. Common regularization methods include for example the Tikhonov regularization of zero-, first- or second-order (Ditmar et al., 2003), regularization using Kaula's rule of thumb for degree variances (Kaula, 2000), and spatially restricted regularization (Metzler and Pail, 2005). Among these methods, Kaula regularization is known for its simplicity and efficiency. Hence, it is applied in this dissertation.

When regularization is applied, the estimation of the parameters is written as

$$\hat{x} = (A^T P A + \alpha R_{reg})^{-1} A^T P l, \quad (2.32)$$

where α is the regularization parameter and R_{reg} represents the regularization matrix. According to Kaula's rule of thumb, the elements r_{ij} of the regularization matrix for spherical harmonic degree n are

$$r_{ij} = \begin{cases} 10^{10} n^4, & i = j \text{ and } m \leq m_{reg}, \\ 0, & \text{otherwise.} \end{cases} \quad (2.33)$$

Because only the zonal and near-zonal coefficients are poorly determined due to the polar gap problem, the maximum order m_{reg} in Eq. (2.33) can be obtained from the rule of thumb presented by Sneeuw and van Gelderen (1997) as

$$m_{reg} = \theta_0 n, \quad (2.34)$$

where θ_0 is the opening angle of the gap in radians, which is approximately 6.5° for GOCE.

As to the regularization parameter α , it is used to weight the normal matrix and the regularization matrix. It can be determined by various methods as discussed in [Kusche and Klees \(2002\)](#), [Koch and Kusche \(2002\)](#), and further optimised to the GOCE case following [Metzler and Pail \(2005\)](#).

In addition to solve the polar gap problem, regularization is also applied to constrain the coefficients of the higher degrees ([Brockmann, 2014](#)). As the gravity field signal attenuates quickly with the height of the satellite, the higher harmonic degrees tend to have a higher amplitude of errors and a poorer signal-to-noise ratio. As a result, Kaula regularization should also be applied to all coefficients above a certain degree.

2.5 Data combination

To recover an accurate gravity field model from GOCE observations, the SST-hl and SGG data must be spectrally combined because they are sensitive to different wavelengths of the gravity field signal. In addition, the regularization matrix should also be combined because of the reason explained in Section 2.4. In this regard, the Variance Component Estimation (VCE) approach ([Koch and Kusche, 2002](#)) is a useful tool for the joint analysis of different types of observations in the LS adjustment. It sums up the normal equation system for each type of observations as follows

$$\left(\frac{1}{\sigma_{sst}^2} \mathbf{N}_{sst} + \frac{1}{\sigma_{sgg}^2} \mathbf{N}_{sgg} + \alpha \mathbf{R}_{reg} \right) \mathbf{x} = \left(\frac{1}{\sigma_{sst}^2} \mathbf{W}_{sst} + \frac{1}{\sigma_{sgg}^2} \mathbf{W}_{sgg} \right), \quad (2.35)$$

where \mathbf{N}_{sst} , \mathbf{W}_{sst} are the pre-processed normal equations for the SST-hl observations group, \mathbf{N}_{sgg} , \mathbf{W}_{sgg} are the normal matrix and vector for the SGG observations group, \mathbf{R}_{reg} represents the regularization matrix. These normal matrices and vectors are summed by weight factors $\frac{1}{\sigma_{sst}^2}$, $\frac{1}{\sigma_{sgg}^2}$, α , where σ_{sst}^2 , σ_{sgg}^2 are variances of unit weight for SST-hl and SGG data, α is the regularization parameter. In practice, they are usually replaced by their posterior variances $\hat{\sigma}_{sst}^2$, $\hat{\sigma}_{sgg}^2$ that are estimated from the individual analysis, since the a priori information is often unknown.

Another issue, which arises from the combination of different observation groups, is their relative contribution to the final result. In this regard, this dissertation will apply the solution proposed by [Schwintzer \(1990\)](#). The products of the inverse normal matrix with the partial

normal matrix sum up to a unit matrix

$$\mathbf{N}\mathbf{N}^{-1} = \sum_{i=1}^n \mathbf{N}_i\mathbf{N}^{-1} = \mathbf{I}, \quad (2.36)$$

here $\mathbf{N} = \frac{1}{\sigma_{sst}^2}\mathbf{N}_{sst} + \frac{1}{\sigma_{sgg}^2}\mathbf{N}_{sgg} + \alpha\mathbf{R}_{reg}$ and \mathbf{N}_i represent the normal matrix for each observation group, e.g., for the SST part it is $\mathbf{N}_i = \frac{1}{\sigma_{sst}^2}\mathbf{N}_{sst}$. The diagonal of $\mathbf{N}_i\mathbf{N}^{-1}$ constitutes of values between 0 and 1, which show the relative contribution of the partial data set to the estimated coefficients.

2.6 Validation of the gravitational field model

After the gravity field model is obtained, validation is required as a further step. Validation can be carried out both internally in the spectral or spatial domain, and externally with other independent observations such as GPS levelling data. Related procedures will be discussed in this section.

2.6.1 Validation in the spectral domain

The analysis of the formal errors is a useful tool to validate the solution of the parameters. In the spectral representation, the errors can be analysed using a two- or one-dimensional spectrum.

Two-dimensional error spectrum

The formal errors of the estimated spherical harmonic coefficients can be obtained by taking the square root of the diagonal elements of the VCM $\Sigma_{\hat{x}\hat{x}}$ which is calculated with Eq. (2.15). If the $\Sigma_{\hat{x}\hat{x}}$ is not computed, the formal errors can be approximately replaced by the differences of the coefficients between the derived and a state-of-the-art model. Next, the obtained formal errors or the coefficient differences can be presented in a two dimensional space formed by degree and order. This is called the two-dimensional error spectrum which can clearly display the error of each coefficient. Often, a logarithmic scale is used for a better representation. The arrangement of the spherical harmonic coefficients is described in Fig. 2.1.

One-dimensional error spectrum

The sum of the squares of the signal/error of the spherical harmonic coefficients at the same degree gives the total signal/error power of the coefficients. Then the two-dimensional error spectrum turns into one-dimensional one. The signal degree variance is calculated from the

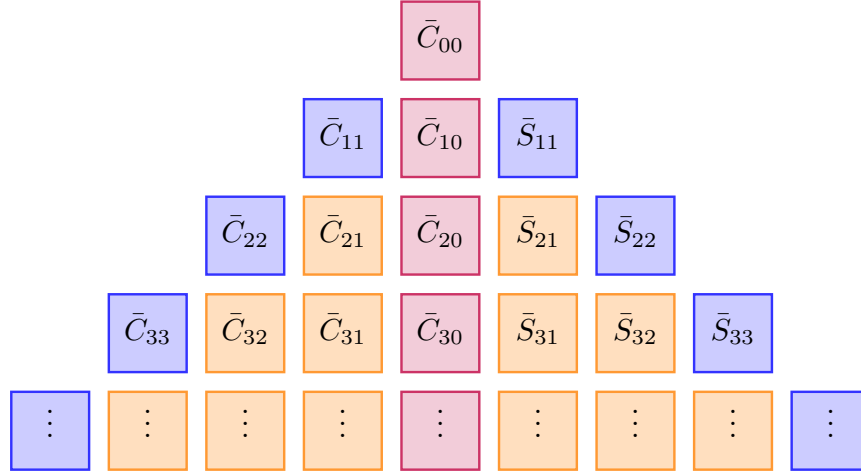


Figure 2.1: The arrangement of the SH coefficients, zonal, sectorial and tesseral coefficients are in different colors.

spherical harmonic coefficients $\bar{C}_{nm}, \bar{S}_{nm}$ by

$$C_n^2 = \sum_{m=0}^n (\bar{C}_{nm}^2 + \bar{S}_{nm}^2), \quad (2.37)$$

and the error degree variance as

$$\sigma_n^2 = \sum_{m=0}^n (\sigma_{\bar{C}_{nm}}^2 + \sigma_{\bar{S}_{nm}}^2). \quad (2.38)$$

Similar as in the two-dimensional error spectrum, the formal errors $\sigma_{\bar{C}_{nm}}^2, \sigma_{\bar{S}_{nm}}^2$ can be replaced by coefficient differences $\Delta\bar{C}_{nm}, \Delta\bar{S}_{nm}$ when the former are not available. For a better understanding, the error degree variance of the unitless spherical harmonic coefficients can be presented in terms of some physical quantities such as the geoid height. According to the error propagation law, the error degree variance of the geoid height is approximated by

$$\sigma_n^2 = R^2 \sum_{m=0}^n (\sigma_{\bar{C}_{nm}}^2 + \sigma_{\bar{S}_{nm}}^2), \quad (2.39)$$

where R is the equatorial radius of the Earth reference ellipsoid.

The average standard deviation of the coefficients at a specific degree n can be derived with the following equation

$$\sigma_n = \sqrt{\frac{\sigma_n^2}{2n+1}}. \quad (2.40)$$

Here σ_n is a representative standard deviation when the error spectrum is isotropic, i.e., it is independent of the order m .

Cumulative geoid height error

The cumulative error, also called commission error, contains all the error power up to a certain degree N . It can be calculated with

$$CUM_N = \sqrt{\sum_{n=0}^N \sigma_n^2} = \sqrt{\sum_{n=0}^N \sum_{m=0}^n (\sigma_{\bar{C}_{nm}}^2 + \sigma_{\bar{S}_{nm}}^2)}. \quad (2.41)$$

The cumulative error in terms of geoid height can be simply obtained by

$$CUM_N = R \sqrt{\sum_{n=0}^N \sum_{m=0}^n (\sigma_{\bar{C}_{nm}}^2 + \sigma_{\bar{S}_{nm}}^2)}. \quad (2.42)$$

As mentioned-above, the formal errors $\sigma_{\bar{C}_{nm}}^2, \sigma_{\bar{S}_{nm}}^2$ can be replaced by the coefficient differences $\Delta\bar{C}_{nm}, \Delta\bar{S}_{nm}$.

2.6.2 Validation in the space domain

The error behaviour of the estimated parameters can also be analysed in the space domain, and many interesting patterns can thus be revealed in a geographic representation of the errors in terms of the disturbing potential, the geoid height, gravity anomalies or gravity gradients. To display the errors geographically, equidistant grid values are computed from the estimated coefficients for the region of interest. Similar as Eq. (2.1), the disturbing potential T can be calculated by

$$T = \frac{GM}{R} \sum_{n=0}^N \left(\frac{R}{r}\right)^{n+1} \sum_{m=0}^n [\Delta\bar{C}_{nm} \cos m\lambda + \Delta\bar{S}_{nm} \sin m\lambda] \bar{P}_{nm}(\cos \theta), \quad (2.43)$$

where $\Delta\bar{C}_{nm}$ and $\Delta\bar{S}_{nm}$ are the coefficient differences w.r.t. the normal gravity field. Note that the normal gravity field in this dissertation is represented by the zonal coefficients of degree 0, 2, 4, 6, 8. The geoid height N is approximated by

$$N = R \sum_{n=0}^N \left(\frac{R}{r}\right)^{n+1} \sum_{m=0}^n [\Delta\bar{C}_{nm} \cos m\lambda + \Delta\bar{S}_{nm} \sin m\lambda] \bar{P}_{nm}(\cos \theta), \quad (2.44)$$

and the gravity anomaly Δg can be calculated by

$$\Delta g = \frac{GM}{Rr} \sum_{n=0}^N \left(\frac{R}{r}\right)^{n+1} (n+1) \sum_{m=0}^n [\Delta\bar{C}_{nm} \cos m\lambda + \Delta\bar{S}_{nm} \sin m\lambda] \bar{P}_{nm}(\cos \theta). \quad (2.45)$$

The gravity gradient component Γ_{rr} is computed by

$$\Gamma_{rr} = \frac{GM}{R^2 r} \sum_{n=0}^N \left(\frac{R}{r}\right)^{n+1} (n+1)(n+2) \sum_{m=0}^n [\Delta\bar{C}_{nm} \cos m\lambda + \Delta\bar{S}_{nm} \sin m\lambda] \bar{P}_{nm}(\cos\theta). \quad (2.46)$$

These quantities can be calculated in pair for both the recovered model and the reference model (normally, one of the state-of-the-art models is chosen as the reference model), and the differences between each pair of quantities can represent the errors of the recovered model. Displaying these differences in space will thus provide useful insight in the spatial behaviour of the errors.

2.6.3 Validation by GPS leveling

External GPS levelling data can be used for an absolute validation of the retrieved gravity model, since the geoid height information derived from GPS geodetic heights and levelled orthometric/normal heights is independent from the derived gravity model. The geoid height can be calculated from ellipsoid heights obtained from GPS with the following equation

$$N = h - H, \quad (2.47)$$

where h is the ellipsoid height, H is the orthometric or normal height, N is the geoid height or quasigeoid height.

As the geoid height can also be calculated from the estimated spherical harmonic coefficients, the differences between the two calculation methods can be regarded as an independent quality assessment measure of the derived gravity model.

Chapter 3

Global gravity field recovery from GOCE SST-hl Data

GOCE is the first satellite mission that measures the Earth's global gravity field with both SST-hl and SGG techniques. The two techniques are designed for different spectral parts of the gravity field. In contrast to the SGG measurements that are sensitive to the medium- and high-wavelength part of the Earth's gravity field, the SST-hl products are mainly responsible for the long-wavelength signal. This chapter is focused on the spherical harmonic analysis of the SST-hl observations. More specifically, Section 3.1 presents a brief introduction about the SST-hl technique as well as the related work about the gravity field retrieval from the SST-hl products. Section 3.2 describes the theory of the acceleration approach and presents the workflow of gravity field recovery based on SST-hl observations. In line with the modules of the workflow, Section 3.3 introduces the data set that is to be used. Section 3.4 discusses the data pre-processing tasks including outlier detection, numerical differentiation and temporal corrections, while Section 3.5 covers the data processing to derive the spherical harmonic coefficients. The derived models are analysed in Section 3.6.

3.1 Background of SST-hl technique and related work

In this section, a brief introduction of the SST-hl technique is given and the main approaches that are used to derive a long-wavelength gravity field model from such SST-hl observations are summarized.

3.1.1 SST-hl technique

Within the concept of Satellite-to-Satellite Tracking in high-low mode (SST-hl), see Fig. 3.1, a Low-Earth Orbit (LEO) satellite is tracked continuously by the high orbiting GNSS satellites, relative to a net of ground stations (Rummel et al., 2002). Non-gravitational forces on the LEO satellite are measured by accelerometry. This technique was firstly implemented in the

CHAMP mission, which was successfully operated from July 2000 to September 2010. During its lifetime, CHAMP provided a large amount of high-quality measurements which covered almost the whole Earth. Based on these measurements, the knowledge about the gravity field was improved by almost one order of magnitude (Reigber et al., 2003; Wernuth, 2008).

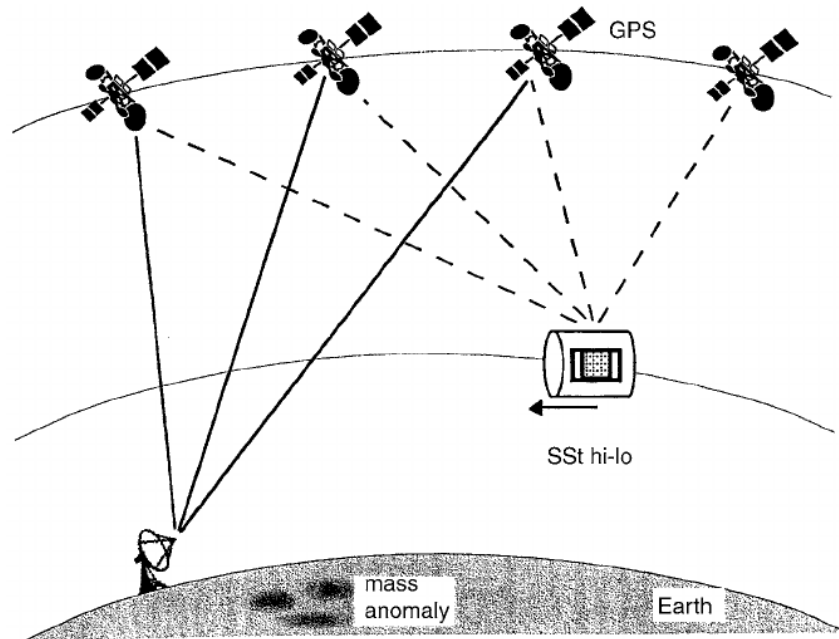


Figure 3.1: Concept of Satellite-to-Satellite Tracking in high-low mode (Rummel et al., 2002)

The same technique was then implemented in the other two satellite gravity missions, i.e., GRACE and GOCE. Launched in March 2002, the GRACE mission consists of two LEO satellites in the same orbit with a distance of 220 km. Both LEO satellites are not only tracked by the high GNSS satellites but also track each other using a K-band microwave ranging system. In other words, GRACE implements both SST-hl and SST-ll in one single mission. This is a great innovation of the GRACE mission, and it yields by far the best global gravity field models at the low-to-medium degrees, e.g., ITG-Grace2010s (Mayer-Gürr et al., 2010). In contrast, the biggest innovation of the GOCE mission is that it implements Satellite Gravity Gradiometry (SGG) and SST-hl in one single mission. SGG, which will be explained in detail in the next chapter, is sensitive to the medium- and high-frequency gravity field signal. And as a spectral complement, SST-hl is employed to recover the low-frequency signal. In this way, the GOCE mission has the potential to derive a high-accuracy gravity field model at higher degrees.

The GOCE satellite is equipped with two 12-channel dual-frequency Lagrange GPS receivers, which ensured uninterrupted tracking of the GOCE spacecraft by the GPS satellites. The scientific orbit products are delivered by GOCE High Performance Facility (HPF), including the Precise Reduced-Dynamic (PRD) and Precise Kinematic (PKI) orbit solutions. Validation shows that both solutions are at a comparable accuracy level of about 2 cm (Bock et al., 2011, 2014).

With the aim to derive a GOCE-only long-wavelength gravity field model, the spherical harmonic analysis based on these orbit products is thus the main topic of this chapter.

3.1.2 Related work

In order to recover the long-wavelength gravity field, several methods have been developed to handle SST-hl observations. These methods are now briefly explained with their pros and cons.

1. Celestial mechanics approach

The celestial mechanics approach is extended from a general orbit determination module within the Bernese software. It has been successfully applied to determine the long-wavelength gravity field from SST-hl observations, see [Jäggi et al. \(2010, 2011\)](#).

Based on the computed a priori orbits $\mathbf{r}_0(t)$, gravity field recovery from kinematic positions is set up as a generalized orbit improvement problem ([Beutler et al., 2010](#)). The actual orbits $\mathbf{r}(t)$ are expressed as a truncated Taylor series

$$\mathbf{r}(t) = \mathbf{r}_0(t) + \sum_{i=1}^n \frac{\partial \mathbf{r}_0(t)}{\partial p_i} \cdot \Delta p_i, \quad (3.1)$$

where a priori orbit $\mathbf{r}_0(t)$ is computed from the initial parameters p_{i0} , the parameters p_i include the arc-specific orbit parameters and the unknown SH coefficients, and $\Delta p_i = p_i - p_{i0}$ denote the corrections to the initial parameters. With the linear form of the functional model, as described in Eq. (3.1), the design matrix can be constructed. And then the normal matrix is assembled in divided arcs, and is finally summed up to the final one. The normal matrix is eventually inverted to obtain the corrections to the a priori gravity field.

When the celestial mechanics approach is used, one should keep in mind that 1) it leads to a more rigorous solution; 2) it is complex to compute the partial derivative in Eq. (3.1), that involves solving a variational equation, see [Beutler et al. \(2010\)](#); 3) the computation cost is high because the variational equation has to be solved for each iteration.

2. Short arc approach

The short arc approach is also called the integral equation approach. It was proposed as a general method of orbit determination by [Schneider \(1968\)](#), and then modified for the gravity field determination by [Schneider \(1969\)](#). This approach was first applied to real SST-hl data analysis by [Ilk et al. \(2005\)](#). In recent years, the short arc approach was widely used to derive the gravity field model from CHAMP data ([Mayer-Gürr et al.,](#)

2005), and then successfully applied to GRACE data (Mayer-Gürr et al., 2010) as well as to the GOCE mission (Yi, 2012b; Baur et al., 2014; Schall et al., 2014).

This approach reformulates the Newton's equation of motion as a boundary value problem (Schneider, 1968). Due to the discontinuities of the kinematic orbit, the whole data set is divided into short arcs. In each arc, the integral equation is written as

$$\mathbf{r}(\tau) = (1 - \tau)\mathbf{r}_A + \tau\mathbf{r}_B - T^2 \int_{\tau'=0}^1 K(\tau, \tau') \mathbf{f}(\tau') d\tau', \quad (3.2)$$

where $\mathbf{r}_A, \mathbf{r}_B$ represent the boundary values at starting time t_A and end time t_B , τ is the normalized time variable, the kernel $K(\tau, \tau')$ is a function of the normalized time τ , and $\mathbf{f}(\tau')$ indicates the specific forces acting on the satellite. In the processing, the perturbing sources should be reduced from $\mathbf{f}(\tau')$ and then be parametrized as SH coefficient corrections w.r.t values of a reference model. The normal equation in individual arcs can be set up in parallel and then combined into a complete one. The corrections to the SH coefficients are estimated from the inversion of the complete normal matrix.

One special feature of the short arc approach is that it is directly based on the orbit positions. It avoids numerical differentiation which is the key to the acceleration approach and the energy balance approach, that are introduced in the following.

3. Acceleration approach

The acceleration approach is directly based on Newton's law of motion, which balances the satellite accelerations with the first-order derivatives of the gravitational potential. In practice, this approach has two concrete realizations: the point-wise acceleration approach and the averaged acceleration approach. These two realizations are different in the computation of the satellite acceleration but are essentially the same for the gravity field recovery. The former was discussed by Reubelt et al. (2003a) and successfully applied to SST-hl data analysis of CHAMP (Reubelt et al., 2006) and GOCE (Baur et al., 2012). The latter was also successfully applied to the analysis of CHAMP data (Ditmar et al., 2006; Liu, 2008) and was further applied to process GOCE and GRACE data (Farahani et al., 2013).

The theory of the acceleration approach can be simply written as

$$\ddot{\mathbf{x}} - \mathbf{a}_f = \nabla V, \quad (3.3)$$

where $\ddot{\mathbf{x}}$ denotes the satellite accelerations that is computed by numerical differentiation of the orbit data, and \mathbf{a}_f represents the accelerations caused by the perturbing forces, V is the gravitational potential.

Compared to the celestial mechanics approach and short arc approach, the functional model of the acceleration approach is more explicit and the design matrix can be set up more easily. The critical part of the acceleration approach, however, is to determine the satellite accelerations from the positions, since the differentiator would inevitably amplify the high-frequency noise of the observations. In order to obtain accurate accelerations from positions, a sophisticated differentiator and low-pass filter has to be integrated to suppress the noise amplification.

4. Energy balance approach

The energy balance approach also known as the energy integral approach is derived from the principle of energy conservation. It was considered for the purpose of gravity field recovery since the beginning of the satellite era (O’Keefe, 1957; Bjerhammar, 1969). A comprehensive description of the application of this approach to SST observations can be found in Jekeli (1999) and Visser et al. (2003). This approach was soon successfully implemented to process CHAMP SST-hl data by several working groups, see Gerlach et al. (2003), Weigelt (2007), Wermuth (2008). Later, it was applied to process GOCE SST-hl data, and led to the first three releases of the GOCE time-wise models (Pail et al., 2011).

According to the energy conservation law, the sum of kinetic and potential energy of a satellite should remain constant given that the satellite is only subject to conservative forces. In reality, non-conservative forces like atmospheric drag, solar radiation pressure, etc. also influence the motion of the satellites, and the subsequent energy accumulation or dispersion has to be considered in order to conserve total energy. Hence, the conservation of energy of one satellite can be written as

$$E_{kin} + E_{pot} - E_{rot} - E_f = C, \quad (3.4)$$

where E_{kin} , E_{pot} represent the kinetic and potential energy, E_{rot} is the so-called “potential rotation”, E_f is the energy accumulated or dissipated due to the non-conservative forces, C is a constant value.

The functional model of the energy balance approach is a linear equation, which makes it simple to construct the design matrix. The main input of this approach is the satellite velocity which is obtained by numerical differentiation, thus this approach also suffers from the problem of noise amplification just like the acceleration approach. Besides, the energy balance approach transforms the vectorial Newton’s equation into a scalar one, which reduces the dimension of the equation system. Although the reduced dimension facilitates the assembly of normal equations thereby simplifying the computational tasks,

it also reduced the number of observations, which may degrade the accuracy of the recovered gravity field.

These approaches are essentially the same because they all originate from Newton's law of motion. However, there is a general consensus that the energy balance approach would provide a slightly worse result than the other three, because the translation of the vectorial function into a scalar one results in a loss of information so that the gravity field model is degraded by $\sqrt{3}$ (Baur et al., 2014). In this dissertation, the acceleration approach will be applied because of its explicit functional model as well as its comparable performance. As explained above, the accurate determination of the satellite acceleration is a big challenge of this approach, since the required numerical differentiation will amplify the high-frequency noise. Thus, the key of applying the acceleration approach is to suppress the noise amplification with appropriate algorithms.

3.2 Acceleration approach

The theory of the acceleration approach is described in detail in this section. Based on the acceleration approach, also the workflow of global gravity field recovery from the GOCE SST-hl data is presented.

3.2.1 Theory of the acceleration approach

It is well known that Newton's law of motion is set up in the Inertial Reference Frame (IRF). The IRF is an orthogonal, right-handed frame with the Z-axis pointing towards the celestial pole and the X-axis fixed in the equatorial plane in direction to the vernal equinox (EGG-C, 2014). For a unit mass, the equation of motion is written as

$$\ddot{\mathbf{x}} = \nabla V, \quad (3.5)$$

where ∇V is the first-order derivative of the gravitational potential and $\ddot{\mathbf{x}}$ is the acceleration of the satellite. In reality, perturbing forces acting on the satellite, e.g., direct tides, indirect tides, drag forces, etc., have to be taken into account. Thus, Eq. (3.5) is extended to

$$\ddot{\mathbf{x}} - \mathbf{a}_f = \nabla V, \quad (3.6)$$

where \mathbf{a}_f represents the perturbing acceleration that has to be subtracted from the satellite acceleration.

Furthermore, all terms in Eq. (3.6) have to be computed in the same reference frame in practice. For example, the GOCE satellite orbit \mathbf{x} is given in the Earth-fixed Reference Frame (ERF) while the derivative of the gravitational potential V is conveniently modelled in the Local North-Oriented Frame (LNOF). Both of them should be transformed into the IRF. As a result, Eq. (3.6) is finally written as

$$\frac{d^2(R_{ERF}^{IRF}\mathbf{x})}{dt^2} - R_{ERF}^{IRF}\mathbf{a}_f = R_{ERF}^{IRF}R_{LNOF}^{ERF}\nabla V, \quad (3.7)$$

where R_{ERF}^{IRF} represents the rotation matrix from ERF to IRF and R_{LNOF}^{ERF} from LNOF to ERF. The rotation matrix between ERF and IRF is constructed from the SST_IAQ data, cf. Eq. (2.8), and the rotation matrix between LNOF and ERF is determined from latitude and longitude of the satellite position according to Eq. (2.7). The first-order derivative of the gravitational potential V is modelled in LNOF following Eq. (2.3). Based on Eq. (3.7), the functional model that relates the satellite orbit with the spherical harmonic coefficients can be set up.

3.2.2 Workflow to process the GOCE SST-hl data

The workflow of recovering the gravity field model from GOCE SST-hl observations using the acceleration approach is depicted in Fig. 3.2. It consists of four modules that are *input*, *pre-processing*, *processing* and *output*.

To extract the long-wavelength gravity field signal from GOCE orbit data, the PKI orbit serves as the main input since it is independent from any external information, while the smooth and continuous PRD orbit serves as a reference to detect the outliers of the PKI orbit. The SST_IAQ_2 product is also required as it provides the rotation information between ERF and IRF.

The satellite's acceleration, the main input for the next module, must be obtained from the PKI orbit. This is done in the pre-processing module with the following steps. First, the outliers of the PKI orbit are detected based on the orbit difference between the PRD and PKI. Afterwards, a sophisticated down-sampling algorithm is applied on the original 1 s data, in order to suppress the potential amplification of the high-frequency noise in the numerical differentiation. A double differentiation is then applied to the down-sampled and "clean" PKI orbit to determine the satellite accelerations. In addition, the temporal corrections caused by the perturbing forces are computed and subtracted from the satellite accelerations.

In the processing module, the obtained accelerations from the previous step are used to derive the spherical harmonic coefficients in two iterations. In the first iteration, the weight matrix is

treated as an identity matrix to assemble the normal matrix. The normal matrix is then inverted for an initial estimation of the spherical harmonic coefficients. Based on the estimation, the residuals are calculated to obtain the empirical VCM. The inverse of the empirical VCM is afterwards used as the new weight matrix for the second iteration.

The derived model contains the estimated spherical harmonic coefficients and their standard deviations. The quality of the model is then evaluated by analysing the error spectrum of the coefficients.

3.3 Data usage

This section introduces the GOCE SST-hl data which is used to determine the long-wavelength part of the Earth's gravity field.

The level 2 SST-hl data identified as SST_PSO_2 product consists of two different precise orbits: kinematic (SST_PKI_2) and reduced-dynamic (SST_PRD_2) orbit. The kinematic orbit is a purely geometrical solution based on GNSS observations without including any gravitational and non-gravitational force models. It is represented by unconstrained position estimates for each observation epoch (1 s sampling interval). The reduced-dynamic orbit on the other hand is based on the numerical integration of the equations of motion, which requires gravitational and non-gravitational force models acting on the satellite as input. Therefore, it is constrained by an a priori gravity field model. The reduced-dynamic orbit solution contains the estimates of the satellite positions and velocities which are given in a sampling interval of 10 s. Because of the different strategies to derive the orbit solutions, the reduced-dynamic orbit is a continuous and smooth solution while the kinematic orbit is non-continuous because of the data gaps of GPS tracking. In addition, in order to support the use of the orbit solutions in the IRF, the rotation information between ERF and IRF is included in the SST_IAQ_2 product.

The kinematic orbit will be used to recover the long-wavelength GOCE gravity field because it is independent of any external information. The smooth and continuous reduced-dynamic orbit is taken as a reference which plays a role in the outlier detection of the kinematic orbit. During mission lifetime, the altitude (mean semi-major axis minus the Earth radius at the equator) of the GOCE satellite is mainly divided into two phases: 1) the altitude was at about 259 km (from November 2009 to July 2012), 2) the altitude was lowered in several steps from 259 km to 229 km (August 2012 to October 2013). The daily altitude of the satellite over the lifetime is shown in Fig. 3.3. In line with the GOCE officially published models, different amounts of kinematic orbit data are used to derive several generations of GOCE long-wavelength models in this dissertation.

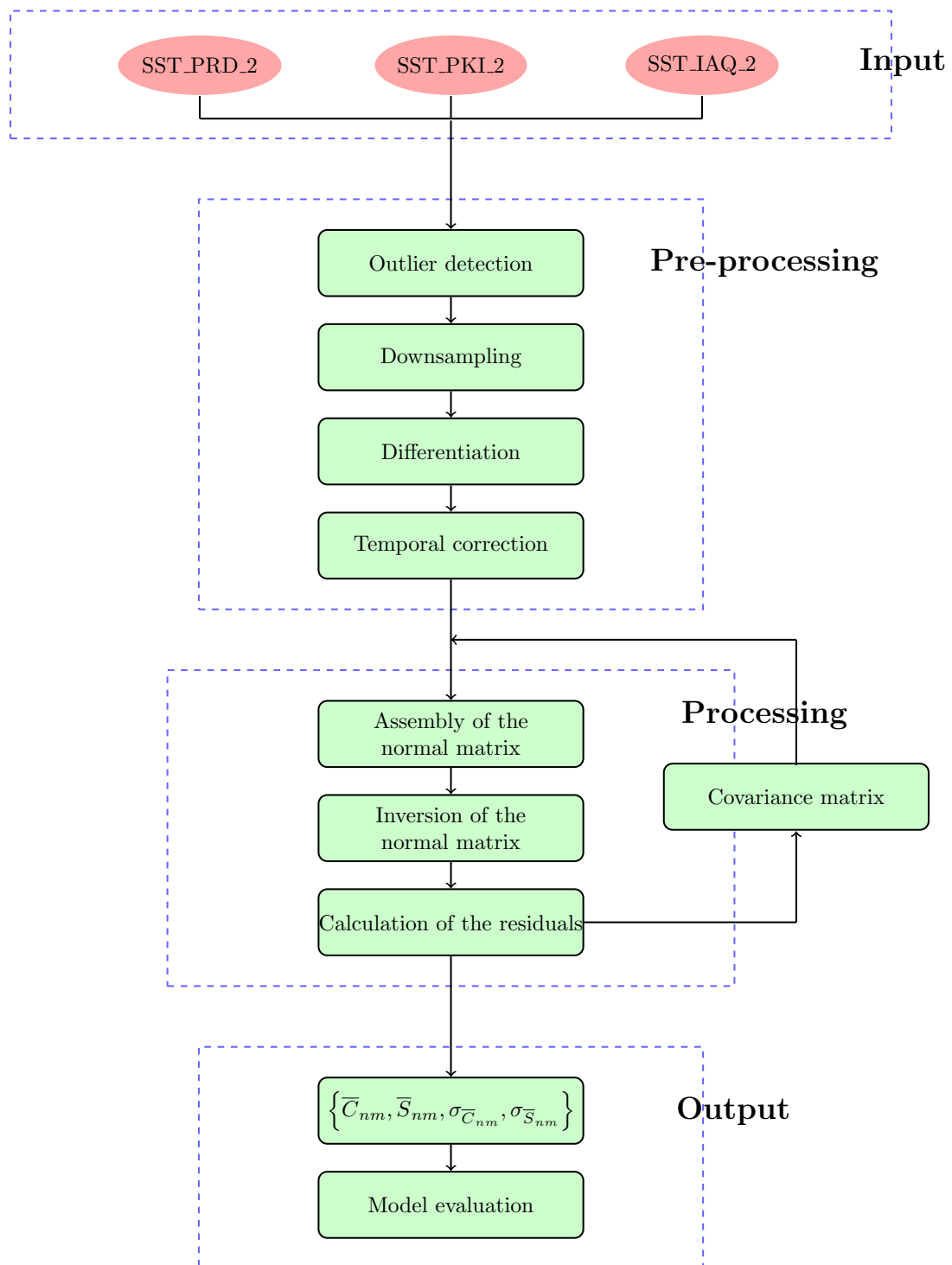


Figure 3.2: Flowchart of global gravity field recovery from GOCE SST-hl data

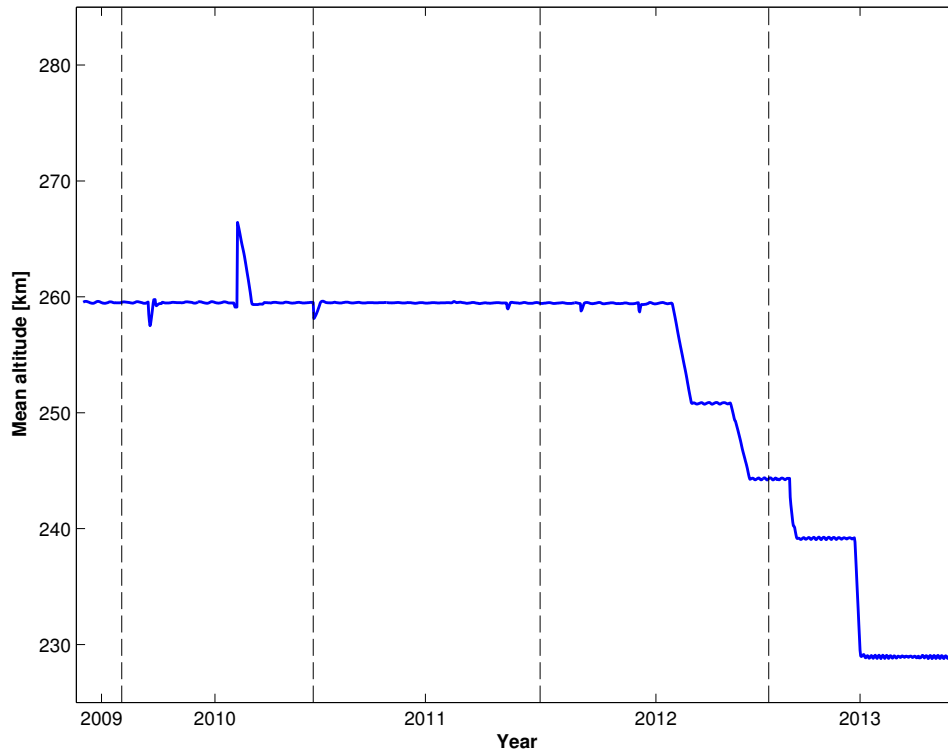


Figure 3.3: The daily altitudes of the GOCE satellite from November 2009 to October 2013

3.4 Data pre-processing

As depicted in the workflow, the pre-processing of SST-hl data include four steps. First, the outliers of the kinematic positions should be detected based on the differences to the PRD data. The cleaned observations then are down-sampled to improve the computation performance while maintaining the accuracy. Next, the acceleration can be calculated by numerical differentiation, and the last step of pre-processing involves temporal corrections. The four steps will be introduced one by one in the following.

3.4.1 Outlier detection

According to [Barnett and Lewis \(1994\)](#), outliers are observations that appear to be inconsistent with the remainder of the dataset. They can be caused by instrument malfunctions, misreading, calculation errors, etc. Unlike the reduced-dynamic orbit determination, the kinematic orbit is purely derived from the GNSS raw measurements, i.e., Carrier-Phase or Code-Phase observations, without applying any force models of the satellite's dynamics. It naturally appears to be more noisy with numerous outliers, jumps and spikes. As proved by [Götzelmann et al. \(2006\)](#), the acceleration approach is very sensitive to outliers so that they have to be detected and eliminated as first step.

In this dissertation, the outlier detection process comprises a pre-detection, which takes place before the numerical differentiation, and a post-detection, which takes place after the numerical differentiation. The pre-detection is based on the raw kinematic positions. An outlier is defined as a kinematic position of which the difference to the PRD orbit is larger than a certain threshold. The post-detection is based on the differentiation results, i.e., the accelerations. In this case, the computed accelerations are compared with the reference accelerations that are computed from an existing gravity field model such as EGM2008. An outlier is also identified when the difference between the two accelerations exceeds a certain threshold. Both the pre- and post-detections ensure an adequate sensitivity to the outliers. The details and results of both detection processes are explained in the following.

For the pre-detection first the PRD orbit is interpolated into the time epoch of the PKI orbit. The differences between the two orbits are then calculated. The orbit differences in all three directions are approximately normally distributed, which is shown in Fig. 3.4 where the probability densities of the orbit differences in November 2009 are examined as an example. Given that it is normally distributed, the next step is to estimate the expectation μ and standard deviation σ of the difference. The thresholds are thus defined as $\mu \pm k\sigma$. Here, k is conservatively chosen as 5 so that only the very large outliers are detected and removed. This avoids to yielding too many data gaps.

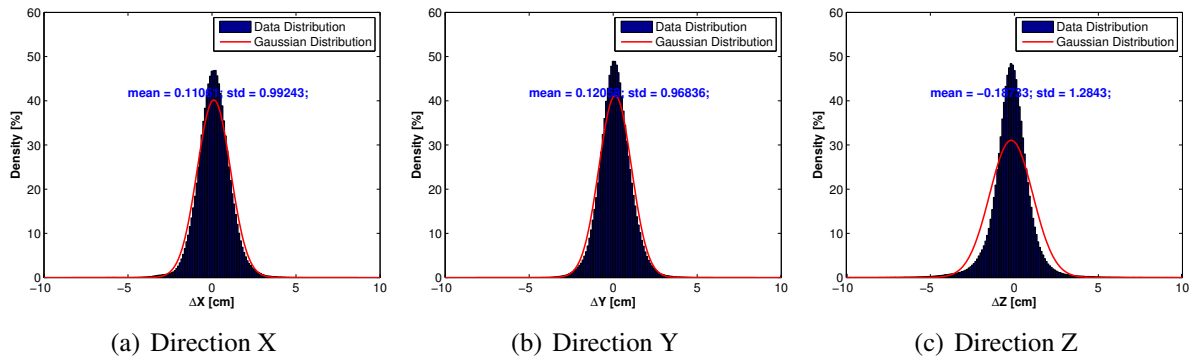


Figure 3.4: The probability density distribution of the orbit differences between PKI and PRD

Taking the PKI orbit of November 2009 as an example, 13,452 observations (0.52%) are labelled as outliers from the 2,579,938 data records. The spatial distribution of the detected outliers is shown in Fig. 3.5. It is clear from the figure that most of the outliers appear in the high-latitude regions. This is due to the poorer GNSS geometry there. Another important factor that affects the accuracy of the orbit is the L2 signal loss (Van den IJssel et al., 2011). This signal loss is the most severe at the magnetic poles.

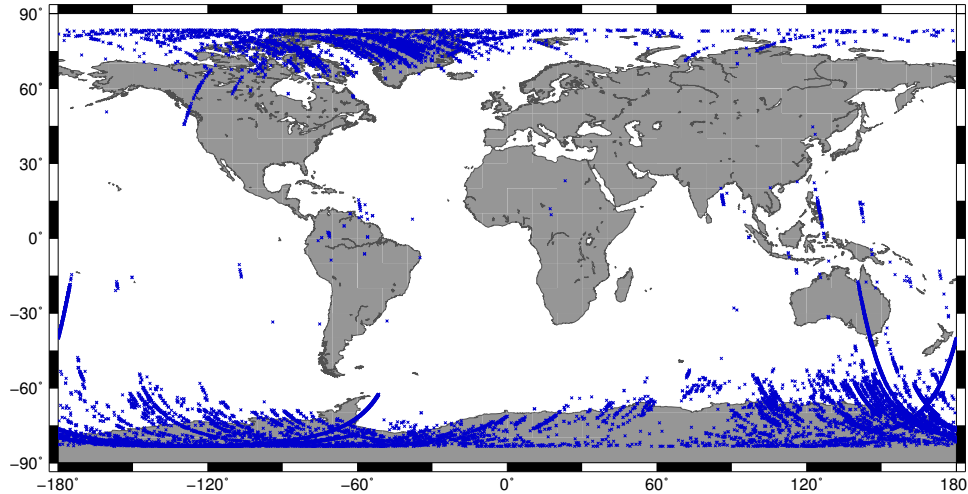


Figure 3.5: Spatial distribution of the outliers of PKI orbit (November 2009)

By numerical differentiation, the accelerations have been derived from the PKI orbit and are ready for the post-detection. The post-detection first generates the reference accelerations from an existing model. Considering that the accelerations are mainly determined by the low-degree coefficients due to the attenuation of the gravity signal, the reference accelerations are actually computed from a truncated EGM 2008 at d/o 60. Afterwards and similarly as for pre-detection, in post-detection the differences between the two accelerations are examined and outliers are identified as those computed accelerations where the differences exceed a given threshold. Here, 3σ is chosen empirically. The post-detection process with the same example data of November, 2009 identifies another 5,042 outliers, which corresponds to 0.19% of the entire observations.

Together, pre- and post-detection give that less than 1% of the entire observations are outliers. These outliers are then removed from the original dataset to avoid a potential propagation of related errors and ensure a good data quality for the following processing.

3.4.2 Down-sampling

Because the gravity field signal attenuates exponentially with the satellite's altitude, the SST-hl technique is only sensitive to the long-wavelength part of the signal. In the case of CHAMP, the Signal-to-Noise Ratio (SNR) of the recovered spherical harmonic coefficients is equal to one at a degree of $N \approx 90$ (Baur et al., 2012). GRACE is supposed to have a similar performance because the satellites of both missions run at a comparable altitude. The situation for GOCE is slightly different because it was at an extremely low altitude, i.e., 259 km, which is about half the altitude of the CHAMP and GRACE satellites. Therefore, the GOCE SST-hl technique is able to sense the gravity field information at a higher degree. Optimistically, the SNR of the

SST-hl observations is supposed to be one at a degree of $N \approx 150$ for the GOCE mission.

The spectral resolution of the gravity field is highly related to the sampling interval Δt . An empirical relation is $N \approx f_N \cdot T$, where N is the maximum resolvable spherical harmonic degree, f_N is the Nyquist frequency which equals to $1/(2\Delta t)$, and T is the revolution period. For instance, the sampling interval of CHAMP is 30 s, which corresponds to a Nyquist frequency of 1/60 Hz, and the revolution period is about 5500 s. Thus, the spectral content of the orbit data fits well with the spectral resolution of the gravity field with $N \approx 90$. For GOCE, the sampling interval of the kinematic orbit is $\Delta t = 1$ s and the period of revolution is about 5400 s. The spectral content of the GOCE orbit data corresponds to gravity field features up to degree $N \approx 2700$ which is significantly larger than the maximum spectral resolution of SST-hl technique. Thus, from the signal processing point of view, the GOCE orbit is oversampled when it is applied for the purpose of long-wavelength gravity field recovery. The spectral content (signal and noise) above the gravity field resolution of GOCE SST-hl will introduce aliasing effects to the lower SH coefficients. Additionally, the differentiator which is used to derive the accelerations from the satellite positions can amplify the high-frequency contributions. The high-frequency contributions of the GOCE orbit data would heavily affect the gravity field recovery, and hence calls for some tailored processing.

A straightforward method to reduce the influence of the high-frequency content of the GOCE orbit data on the long-wavelength gravity field recovery is to down-sample the data. Down-sampling can be regarded as low-pass filtering. An orbit with a larger sampling interval, e.g., 10 s, can be obtained by picking up one observation every 10 sampling points. The drawback of this approach is that a large proportion (depends on the down-sampling interval) of the measurements will be discarded. To cope with this problem, an improved approach named Extended Differentiation Filter (EDF) was proposed by [Baur et al. \(2012\)](#), the scheme of which is depicted in Fig. 3.6. This approach designs a differentiation filter which moves along the original 1 s orbit with a selected down-sample interval. In this way, the influence of the high-frequency content can be mitigated without big loss of measurements.

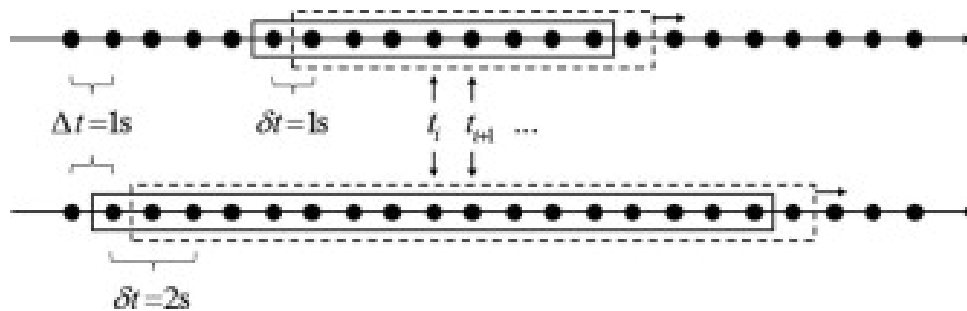


Figure 3.6: The scheme of the EDF, cited from [Baur et al. \(2012\)](#)

Baur et al. (2012) also discussed another strategy which applies a sophisticated low-pass filter using the Infinite Impulse Response (IIR) technique to remove the high-frequency signal content of the orbit. With defined passband and stopband frequencies as well as the maximum damping in the passband and stopband, an appropriate filter can be designed. Their research proves that the IIR filter and EDF can provide similar results of spherical harmonic coefficients. However, EDF is more flexible as it only requires the definition of the down-sampling interval. Therefore, the EDF approach is finally applied in this dissertation.

3.4.3 Numerical differentiation

The acceleration approach requires the satellite accelerations as main input which has to be derived from the PKI positions by numerical differentiation. An ideal differentiator to derive the accelerations can be described by the spectral transfer function $H(e^{i\omega T})$ as

$$H(e^{i\omega T}) = i\omega^2, \quad 0 \leq |\omega| \leq f_N, \quad (3.8)$$

where ω is the frequency, f_N represents the Nyquist frequency and i the imaginary number. According to Eq. (3.8), the high-frequency components of the observations are amplified during the procedure of numerical differentiation. In order to suppress such amplification, a sophisticated numerical differentiator has to be employed.

The most common way of computing numerical derivatives of discrete data is using an analytical function to fit the sampled points and to determine the derivative by analytically differentiating the function. Normally, a polynomial is chosen as the analytical function. For example, a polynomial of order $r = m - 1$ is used to fit m sample points. Various methods can be used to solve such polynomial coefficients, such as Newton-Gregory, Gauss, Lagrangian, etc. Reubelt et al. (2003a) presented time series expressions of the second-order derivative of Newton's interpolation formula for equidistant sampling points. Weigelt (2007) mentioned the Taylor differentiator, which is a central finite difference approximation based on a Taylor series. Although the way to calculate the polynomial coefficients are different, these methods are equivalent since the polynomial coefficients are theoretically uniquely determined. Furthermore, if the order of the polynomial fulfils $r < m - 1$, the polynomial coefficients can be solved by LS adjustment. This approach is successfully applied by Savitzky and Golay (1964) for smoothing and differentiation of equidistant sampling data, and the polynomial coefficients are listed in look-up tables. Additionally, from the signal processing point of view, the differentiators are anti-symmetric Finite Impulse Response filters of type III so that the differentiator coefficients can be determined from the required frequency specifications. For example, a smooth and noise-robust differentiator which is designed from the desired frequency responses

and also exactness on polynomials is presented in [Holoborodko \(2008\)](#).

The above-mentioned numerical differentiators provide sufficient options to derive the satellite accelerations. However, previous studies have shown that the 9-point Taylor differentiator performs best in processing the SST-hl observations of CHAMP ([Reubelt et al., 2003a,b](#)). As the name suggests, the Taylor differentiator is constructed based on a Taylor series, which relates the value of a differentiable function at any point to its first- and higher-order derivatives at a reference point. Consequently, the first- or higher-order derivatives at the reference point can be obtained in terms of the sampled values of the function. A closed-form expression for the finite difference approximations of the first- and higher-order derivatives is described in [Khan and Ohba \(1999\)](#). The second-order derivative is applied in this dissertation. Based on a central difference approximation of order $2n$ (e.g., $2n = 8$ for 9 data points), it reads

$$f_i'' = \frac{1}{T^2} \sum_{k=-n}^n g_k f_{k+i}, \quad (3.9)$$

where, f_i'' is the second-order derivative of the i^{th} observations, f_i indicates the i^{th} observation, T is the sampling interval, and g_k are the differentiator coefficients which are calculated by

$$g_k = \begin{cases} -2 \sum_{k=1}^n g_k, & k = 0, \\ (-1)^{k+1} \frac{2!}{k^2} \frac{(n!)^2}{(n-k)!(n+k)!}, & k = \pm 1, \pm 2, \dots, \pm n. \end{cases} \quad (3.10)$$

Fig. 3.7 shows the frequency behaviour of the ideal differentiator and the employed 9-point Taylor differentiator. The red line denotes the ideal differentiator which is identical to a parabola since for double differentiation any signal needs to be multiplied by ω^2 , as described in Eq. (3.8). The blue line denotes the 9-point Taylor differentiator when it is applied to the original 1 s GOCE orbit data. The blue line is identical to the ideal differentiator up to a frequency of 0.25 Hz, and then a damping effect is visible. According the empirical rule mentioned previously, the frequency of 0.25 Hz corresponds to the gravity field up to d/o of about 1350, which is significantly higher than the sensitivity of the SST-hl technique. Thus, the high-frequency component is strongly amplified and needs to be filtered. The down-sampling procedure is employed, as discussed in Section 3.4.2.

3.4.4 Temporal corrections

According to Eq. (3.7), the accelerations caused by the perturbing forces (e.g., tidal forces, non-conservative forces, etc.) have to be removed from the measurements. In this dissertation, the effects caused by the direct tides (only those caused by the Moon and Sun are considered,

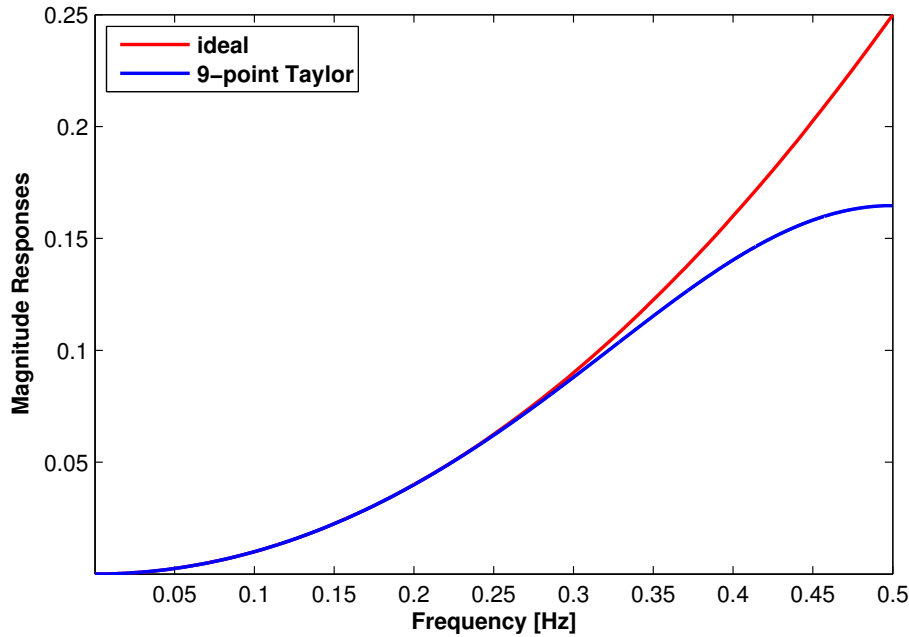
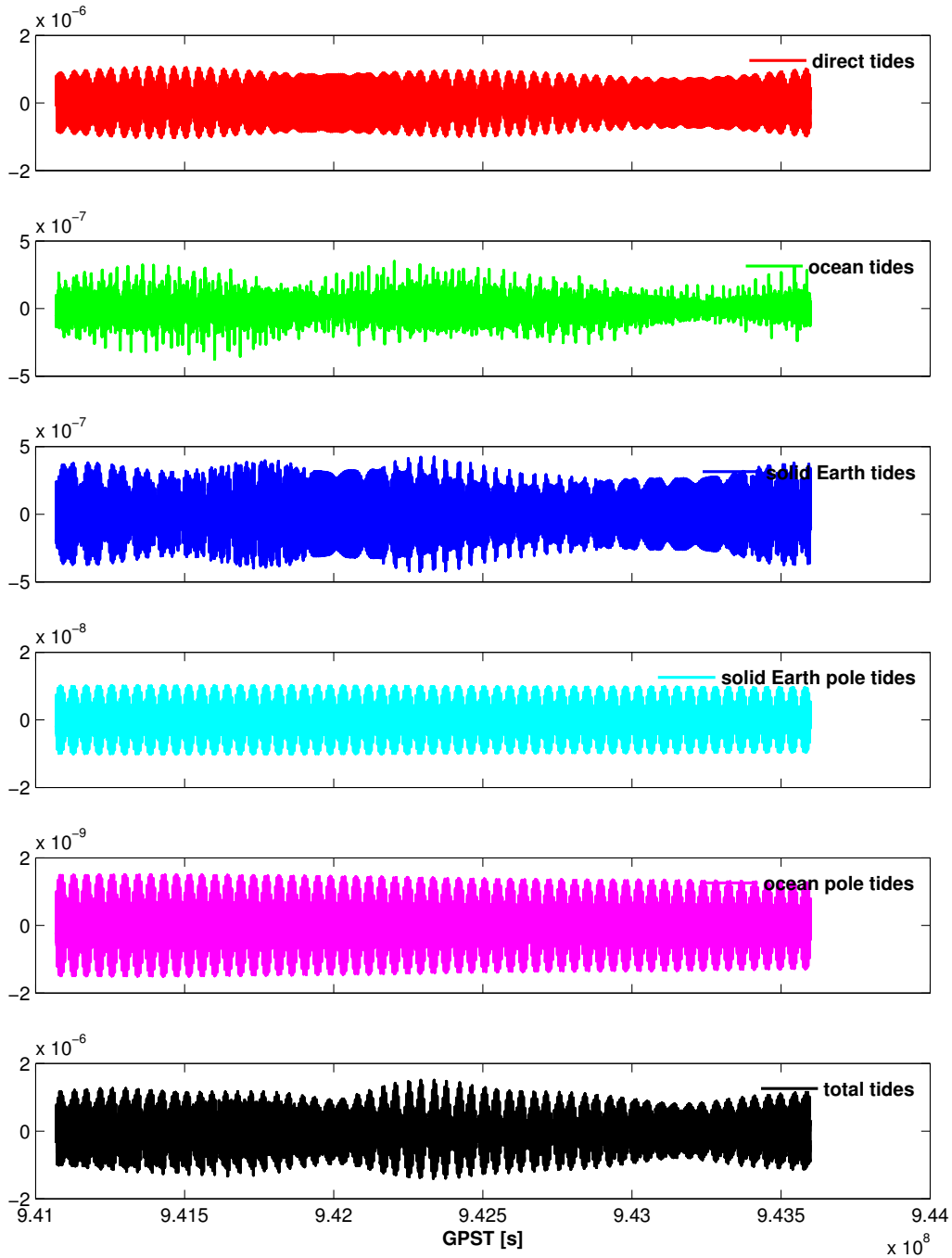


Figure 3.7: Frequency responses of the second-order differentiators

they are biggest due to the short distance of the Moon and huge mass of the Sun), the solid Earth tide, the ocean tide, the solid Earth pole tide and the ocean pole tide are also considered. More details of the computation are given in Appendix A.

Taking a_z as an example, Fig. 3.8 shows the time-series plots of the computed tidal accelerations for November 2009. The contributions of the direct tides are the largest, at the level of 10^{-6} m/s^2 . Followed by the ocean tides and the solid Earth tides, their contributions are at a comparable level but about one magnitude less than the contribution of the direct tides. The pole tides, including the ocean pole and the solid Earth pole tides, are the smallest, about two magnitudes less than the direct tides. Fig. 3.9 shows the root PSDs of these tidal accelerations. It clearly shows that the signals of the tide corrections are biggest at the very long-wavelength part, e.g., at multiples of cycle per day (cpd) and cycle per revolution (cpr). It indicates that the tidal accelerations may affect the very low-degree gravity field coefficients if they are not reduced. In addition, the spatial distribution of the corrected accelerations in three directions are shown in Fig. 3.10. The patterns of a_x and a_y are similar. On contrary, a_z presents an adverse pattern. The magnitude of corrections on a_z is at the same level as of a_y , both of which are almost twice of a_x .

Unlike the tidal forces, the effects caused by the non-conservative forces are left without correction. The non-conservative forces mainly include the atmospheric drag and solar radiation pressure and they can be measured by the accelerometer. In the GOCE mission, the satellite was kept in “free-fall” by a drag-free control system. The non-conservative forces (mainly air drag) in the along-track direction were compensated to a large extent. The remaining residual

Figure 3.8: Tidal accelerations a_z in November 2009, unit is m/s^2

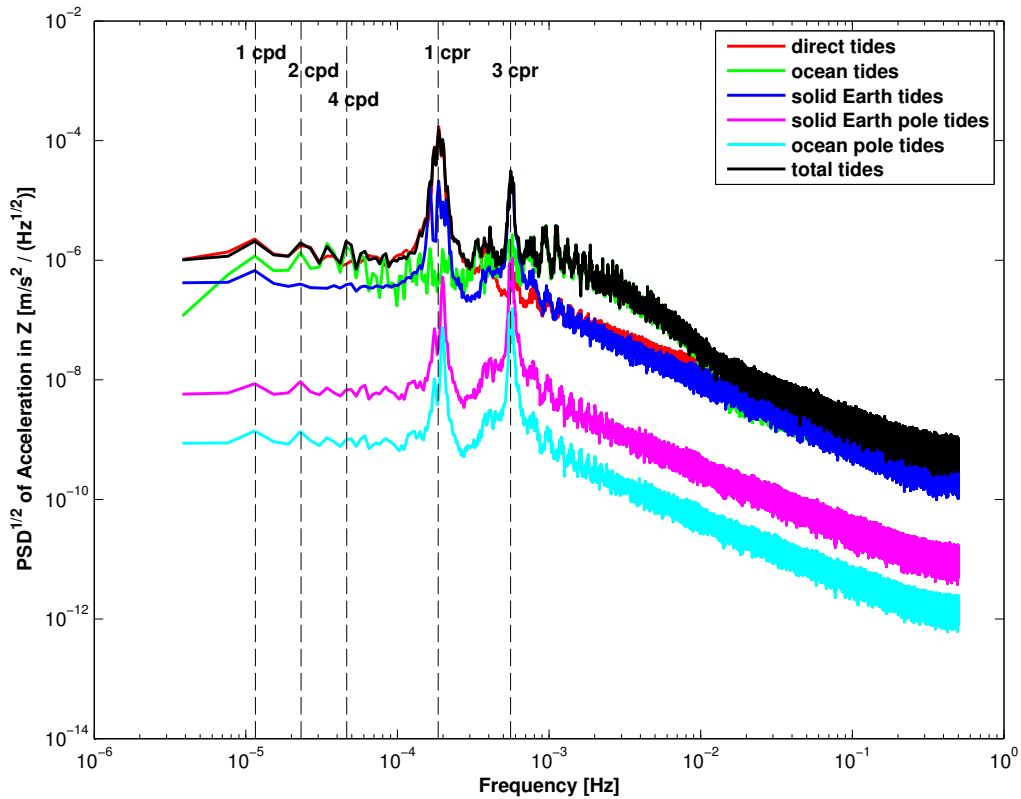


Figure 3.9: Root PSDs of the tidal accelerations a_z in November 2009

disturbances can be derived by half the sum of the accelerations measured by the accelerometers of one arm that are known as the Common Mode Accelerations (CMA). They are contained in the product EGG_NOM_1b.

Some previous studies have demonstrated that the recovery of the long-wavelength gravity field from LEO is largely insensitive to non-conservative perturbations. [Ditmar et al. \(2006\)](#) concluded that removing the non-conservative effects from the satellite accelerations does not lead to an improvement of the estimated SH coefficients. These findings were also supported by [Weigelt et al. \(2011\)](#) in which no prior knowledge of the non-conservative forces was used. Consequently, the non-conservative forces are left without any corrections in this dissertation.

3.5 Data processing

The pre-processing module provides “clean” satellite accelerations from the GOCE PKI orbit data. Thereafter, the processing module works with these accelerations in order to recover a long-wavelength global gravity field model.

Theoretically, the main steps to derive the gravity field model from the accelerations include the assembly of the normal matrix, the inversion of the normal matrix, and a matrix multiplication

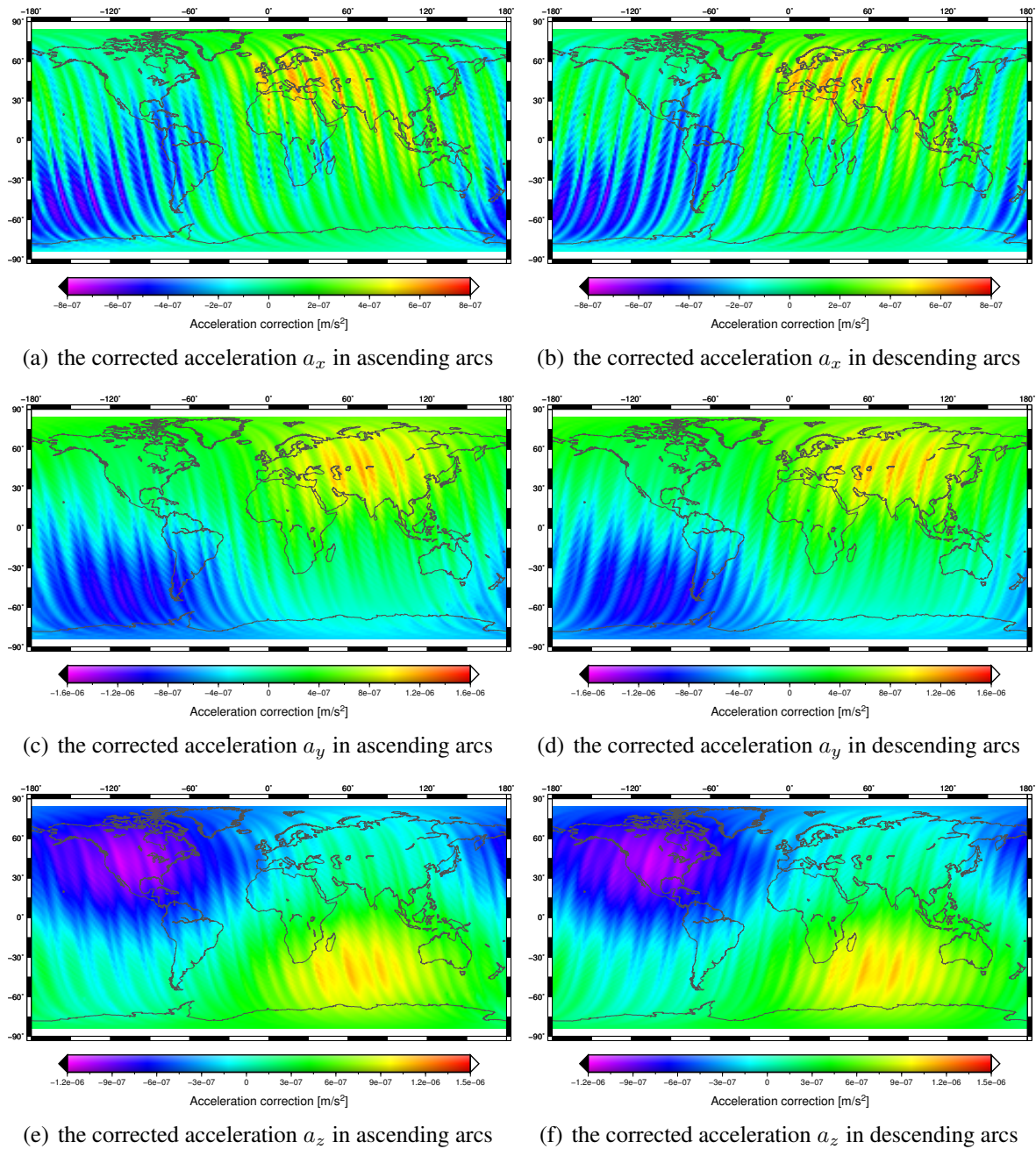


Figure 3.10: Spatial distribution of the tidal corrections in November and December, 2009

to obtain the estimations of the SH coefficients. However, an appropriate assembly of the normal matrix is based on the knowledge of the quality of the observations, which is missing in the starting phase.

To handle this problem, this dissertation designs the processing module as an iteration procedure. In the first iteration, the quality of all observations are assumed as equal and an identity matrix is taken as the weight matrix to assemble the normal matrix. Afterwards, the normal matrix is inverted to get the first estimation of the SH coefficients.

Instead of directly adopting this first and rough estimation of the SH coefficients, these estimated coefficients are only used to calculate the residuals of the observations. The residuals are empirically treated as an estimate of the true errors. The Root PSDs of the residuals are shown in Fig. 3.11. It clearly shows that the errors of the three acceleration components present coloured noise behaviours over the aimed spectral bandwidth. As already discussed in Section 2.2.4, a proper stochastic model of the observations has to be applied in the LS adjustment to handle such coloured noise. The empirical VCMs are thus computed from the residual observations, see more details about the computation in Section 4.3.3. The inverse of the empirical VCM is used as new weight matrix and triggers the second iteration for model recovery. In the end of the second iteration, a new estimation of the SH coefficients as well as their standard deviations are obtained. The estimated coefficients and the standard deviations are the output of the processing module.

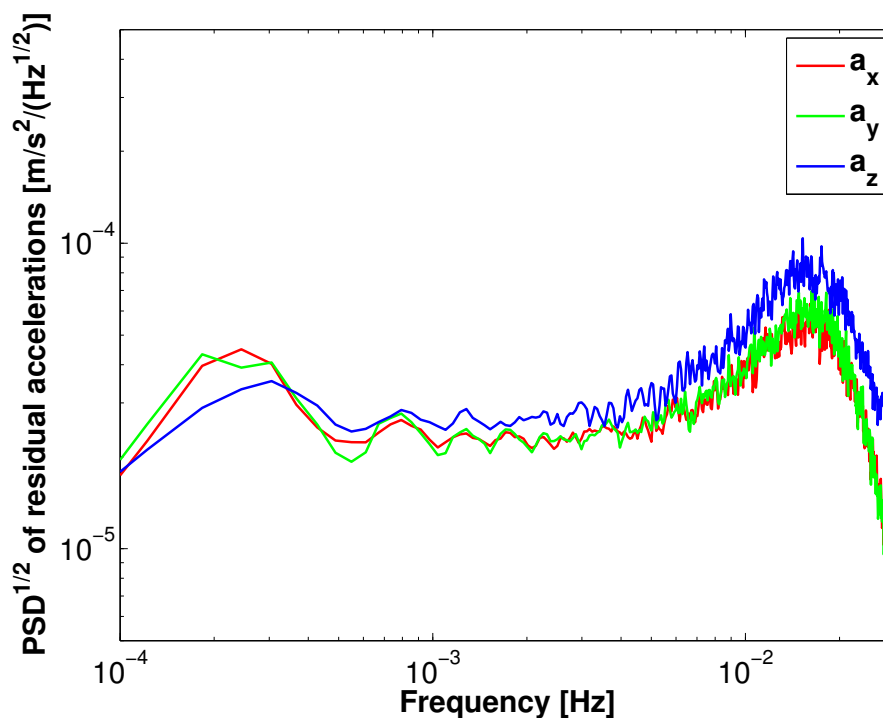


Figure 3.11: Root PSDs of the residual accelerations

The assembly of the normal matrix is performed arc-wisely by dividing the whole data set into many short satellite arcs. Firstly, this facilitates the parallel computation. Multiple processing units are distributed in a convenient way to process the data of different arcs at the same time. Then, one empirical parameter (a constant) is added to absorb systematic errors of the observations in one arc, which implicitly assumes having the same systematic errors for all observations of one arc. In addition, the empirical VCMs of the observations are also computed in each arc. Hence, the length of the arc becomes crucial for the quality of the recovered model. If the length is too short, the empirical parameters would absorb not only the systematic errors but also the very long-wavelength gravity field signal. If the length is too large, the systematic errors can not be fully absorbed. In this dissertation, the arc length is chosen as 35 minutes by trial and error.

The computation for the above-mentioned steps is mostly realized in the cluster system of Leibniz Universität IT Services (LUIS). More details about the cluster system are given in Section 4.5.3. Supposing that 40 jobs (based on the achievable resources) are running in parallel to assemble the normal matrix, the wall time that is required to process 2-month observations with 1 s sampling interval is shown in Fig. 3.12(a). It takes about 1.58 hours to assemble the normal matrix for one acceleration component if the model is truncated at d/o 150. Compared with the assembly of the normal matrix, the inversion of the normal matrix can be finished in 15 minutes which takes only a small proportion of the total computational time. In addition, the memory space that is required to store the normal matrix is depicted in Fig. 3.12(b). More than 2 GB is needed to store the normal matrix if the model is truncated at d/o 150.

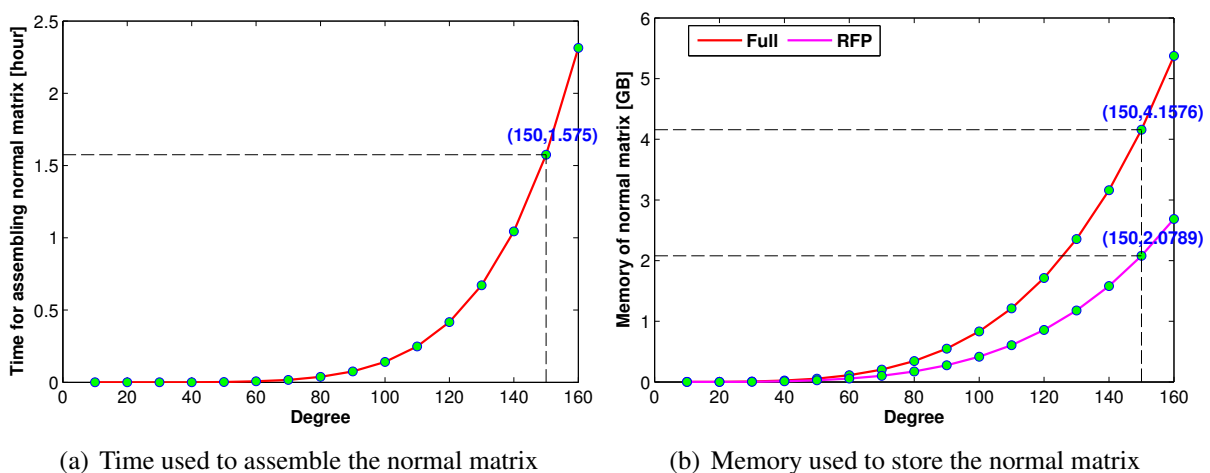


Figure 3.12: Time and memory used to assemble the normal matrix. The computation is based on a single acceleration component from November and December, 2009. The sampling interval is 1 s.

3.6 Result Analysis

Applying the introduced processing steps, a gravity field model is obtained from the complete GOCE PKI orbit. The model is recovered up to d/o 150. In this section, the obtained model is analysed with reference to the most accurate long-wavelength gravity field model ITG-Grace2010s.

First, Fig. 3.13 shows the two-dimensional error spectrum of the estimated coefficients. It demonstrates that the performance of the zonal and near-zonal coefficients are poorly determined due to the polar gaps. This is in agreement with the empirical rule that is addressed by Sneeuw and van Gelderen (1997). Hence, these degraded coefficients are not included in the following analysis. It also clearly shows that the coefficients at lower degrees are determined more accurately than the higher-degree part. This agrees with the fact that the SST-hl observations are more sensitive to the long-wavelength gravity field signals.

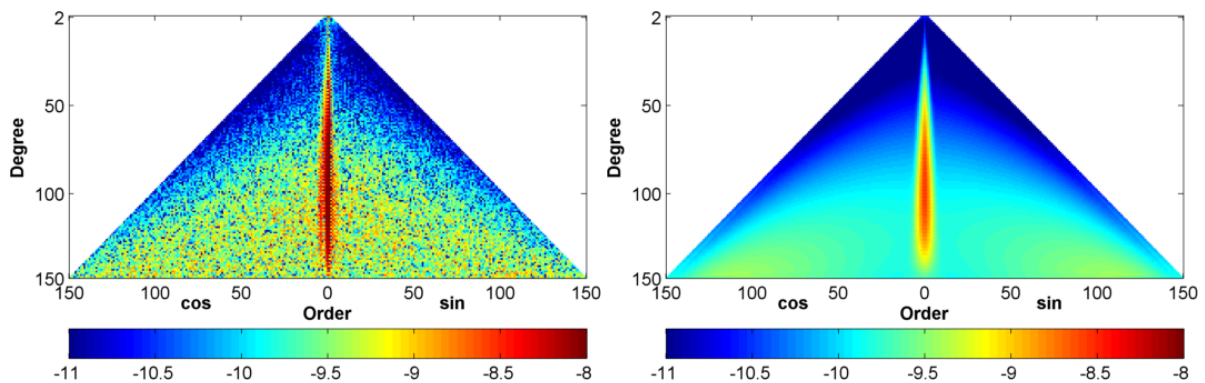


Figure 3.13: Two-dimensional error spectrum of the estimated coefficients (unitless). Left: coefficient differences w.r.t. ITG-Grace2010s; right: formal errors. Both are in logarithmic scale.

Second, the one-dimensional error spectrum of the estimated coefficients is calculated following the formulas provided in Section 2.6.1. The results are shown in Fig. 3.14 which includes the Degree-Error RMS (DE-RMS) and the degree median values. According to both figures, the signal-to-noise ratio of the recovered gravity field model is approximately one at d/o 150. The pattern of the formal errors coincides with the coefficient differences w.r.t. ITG-Grace2010s, except for the degree-2 coefficients. A large difference is visible there, which indicates the GOCE SST-hl observations or the employed acceleration approach is not sensitive to the degree-2 coefficients.

Furthermore, Fig. 3.15 shows the cumulative geoid height error w.r.t. ITG-Grace2010s. The geoid height error up to d/o 100 is about 7.76 cm.

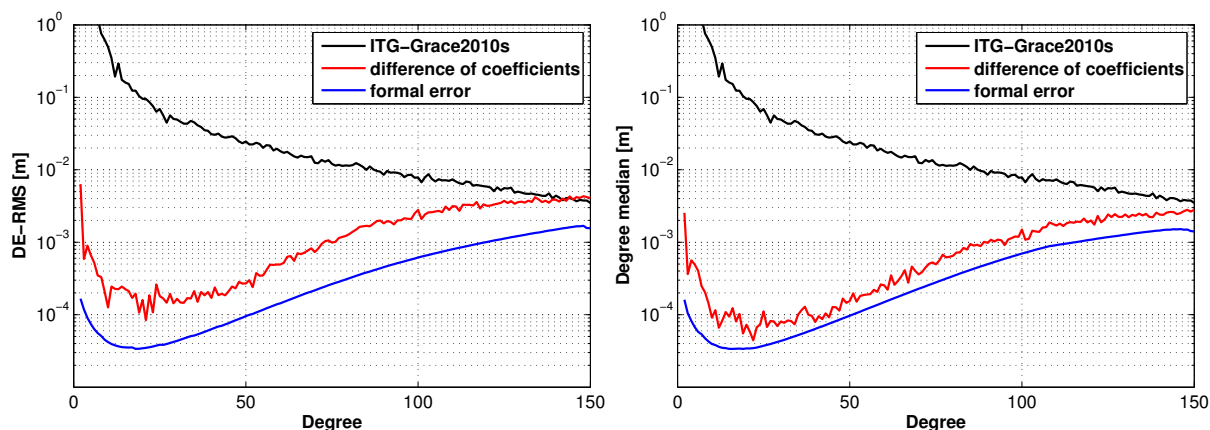


Figure 3.14: One-dimensional error spectrum of the estimated coefficients, left: DE-RMS; right: degree median values. The red curves represent the coefficient differences and the blue curves represent formal errors.

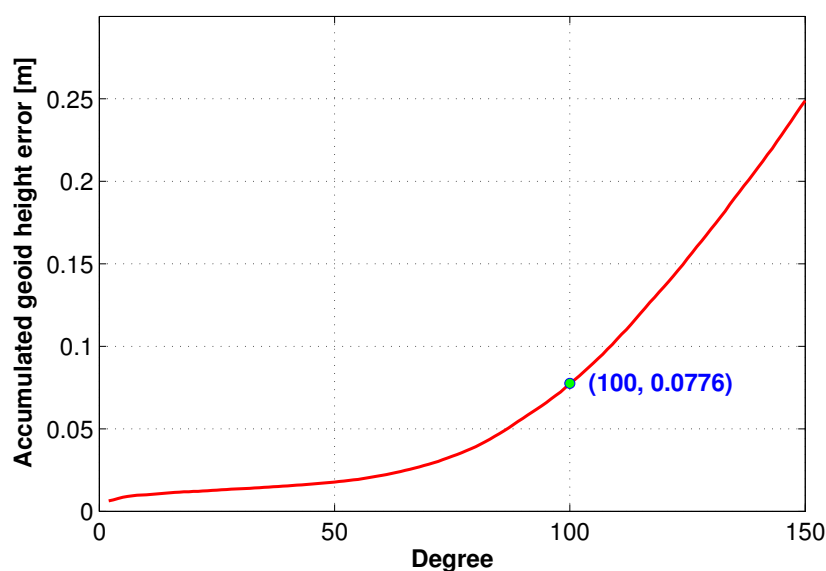


Figure 3.15: The cumulative geoid height error w.r.t ITG-Grace2010s

In addition, in order to understand the influence of data volumes on the recovered model, a series of four models, named as SST_R2, SST_R3, SST_R4, SST_R5, are derived from the PKI orbits with different data volumes. The data volumes for the four models are 8 months, 16 months, 32 months and 47 months, respectively. These time periods correspond to the second to fifth generation of the officially GOCE published models. The comparison results of these models are presented in Figs. 3.16 and 3.17. The figure shows that the high-degree coefficients (above d/o 50) are slightly improved with the increasing amount of observations from SST_R2 to SST_R5. However, the performances of the low-degree coefficients (below d/o 50) are at a similar level. Therefore, increasing the number of observations can improve the medium-wavelength signal, while it contributes little to the improvement of the very long-wavelength part of the gravity field.

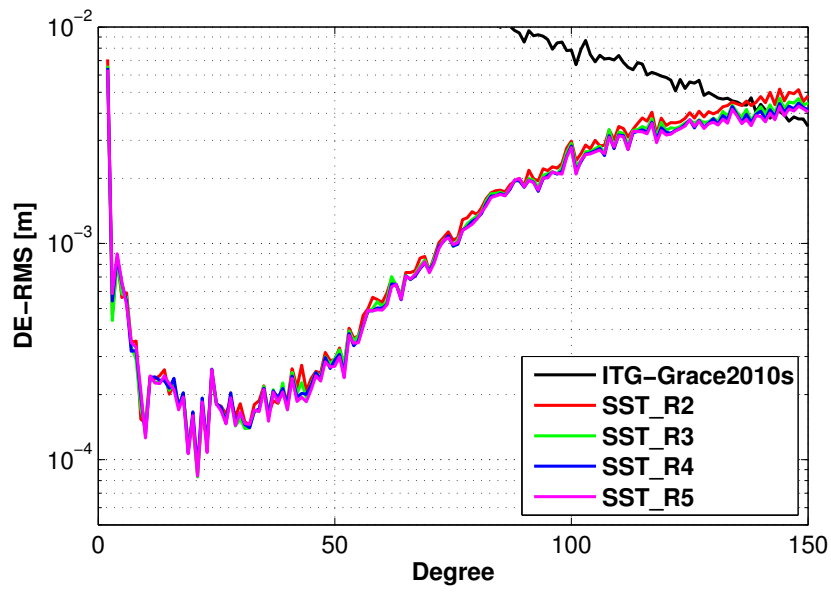


Figure 3.16: The DE-RMS of the SST only solutions w.r.t. ITG-Grace2010s

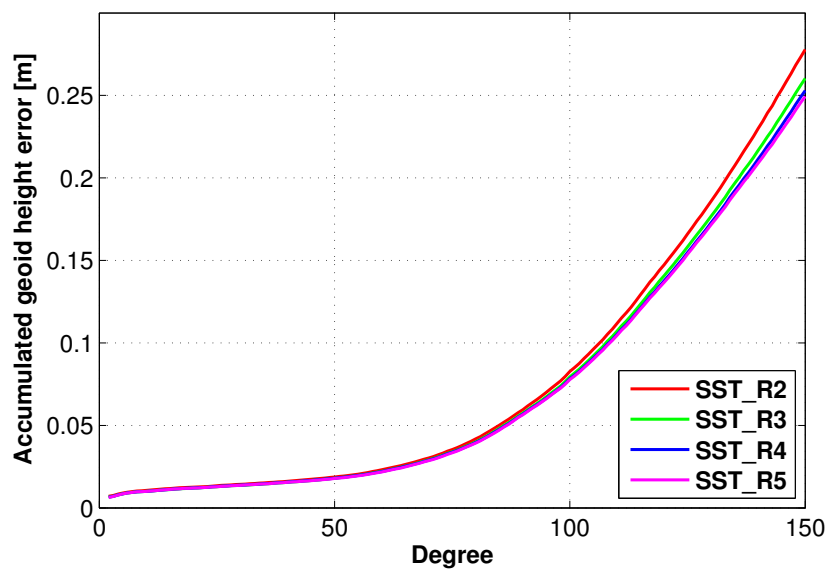


Figure 3.17: The cumulative geoid height errors of the SST only solutions

Chapter 4

Global gravity field recovery from GOCE SGG data

In Chapter 3, the SST-hl observations are comprehensively studied to determine the spherical harmonic coefficients of lower degree and order. The derived model can represent the major irregularities (deviations from a spherically shaped gravitational field) of the Earth's gravity field. The smaller deviations that reflect the detailed structures of the Earth's gravity field are represented by higher degree and order coefficients. Knowledge of the gravity field down to a fine-grained scale helps to better understand the physics of the interior of the Earth, the dynamics of the oceans, the unification of the height systems, etc. (Rummel et al., 2002). Therefore, this chapter aims to determine the spherical harmonic coefficients of higher degree and order from the GOCE Satellite Gravity Gradiometry (SGG) data.

First, the technique background and related work of GOCE SGG are briefly summarized in Section 4.1. Section 4.2 presents the workflow of gravity field recovery based on SGG data. This task is divided into four modules, namely data understanding, data pre-processing, model recovery, and model evaluation. The four modules are described separately in Sections 4.3 to 4.6.

4.1 Technique background and related work

The GOCE SGG data, i.e., the gravity gradients, are observed by the Electrostatic Gravity Gradiometer (EGG) that is an implementation of gradiometry and was first carried on board a spacecraft. To provide some technique background for this chapter, this section first introduces the gradiometry technique (Section 4.1.1) and the EGG implementation (Section 4.1.2). The GOCE SGG data has been intensively studied by many researchers in the past. Thus, this section also summarizes the methods that have been used in literatures (Section 4.1.3).

4.1.1 Introduction to gradiometry

In order to detect the Earth's gravity field at a fine-grained scale, various kinds of techniques have been applied during the past decades, such as terrestrial gravimetry, airborne gravimetry and satellite gravimetry. Terrestrial gravimetry can obtain the full-spectrum signal of Earth's gravity with high accuracy, but it is both expensive and time-consuming to cover large areas. In addition, due to the complex topography of the Earth, such as high mountains and oceans, it is not feasible to apply terrestrial gravimetry at a global scale. Compared with terrestrial gravimetry, airborne gravimetry is more efficient, while its application is also restricted to local regions. In contrast, satellite gravimetry provides an opportunity to measure the whole Earth within short time with one single mission and in homogeneous quality. A shortcoming of this technique is that the signal of the Earth's gravity field attenuates quickly as the altitude of the satellite increases, with the attenuation effect approximated as $(\frac{R}{R+h})^n$, where R is equatorial radius of the Earth, h is satellite altitude and n denotes the spherical harmonic degree.

As noted above, the gravity signals that are represented by higher degree coefficients attenuate much. Gradiometry was proposed to overcome the problem caused by attenuation. It measures the second-order derivatives of the gravitational potential (Rummel, 1986; Rummel et al., 1993). When expressed in a spherical harmonic series, double differentiation roughly results in an amplification of the coefficients by a factor of n^2 . Thus, signals represented by higher degree coefficients can be significantly amplified compared to those by lower degree coefficients.

An instrument that measures the gravity gradients is called a gradiometer. The first gradiometer was realized by the Hungarian physicist Eötvös at the beginning of 20th century. With a so-called torsion balance, he measured the Earth's gravity gradients with a precision of 1 E ($E = 10^{-9} \text{ s}^{-2}$), cf. Koop (1993). A torsion balance consists two proof masses that are asymmetrically suspended to an arm of balance. Gravity gradients produce a torque on the balance, resulting in a rotation of the beam. The gravity torque is counterbalanced by a restoring torque with which the beam is kept suspended. The restoring torque is a measure for the gravity gradients.

In practice, the gradiometer is built using another technique, namely differential accelerometry (Rummel, 1986; Rummel et al., 2011). It measures the change of the distance between two falling proof masses. Supposing the falling masses are held in a fixed position relative to each other and their distance remains constant during their free fall, then the force needed to constrain the motion is measurable and can be used as a measure of the gravity gradients, i.e., the variation of gravity in the direction of the line connecting the two masses. This is the principle used in spaceborne gradiometry, with the GOCE payload EGG as the first realization.

4.1.2 Electrostatic Gravity Gradiometer

EGG is one of the core instruments on board GOCE satellite. It consists of six capacitive accelerometers arranged orthogonally and in pairs at a distance of 50 cm, with each pair forming a gradiometer arm (see Fig. 4.1). Within an accelerometer, a proof mass is floated in a small cage and is kept in the center of the cage by electrostatic forces. These voltages are representative for the accelerations sensed by the proof mass and are the initial input to a long chain of processing steps (Cesare, 2008; EGG-C, 2006).

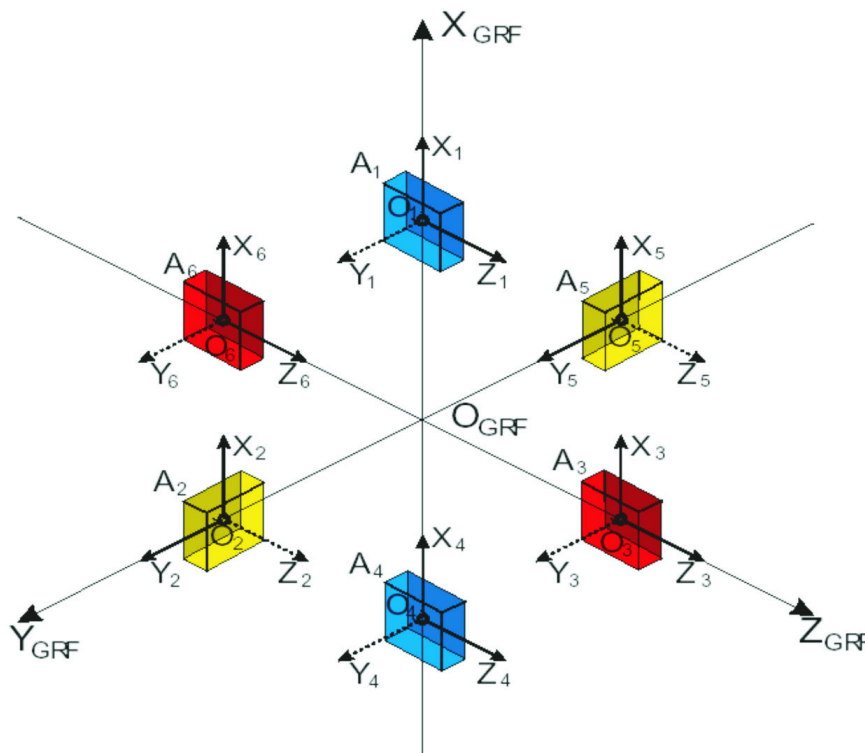


Figure 4.1: Configuration of EGG. 6 accelerometers in pairs are orthogonally mounted in three gradiometer arms. Each accelerometer has 3 axes, with 2 ultra sensitive axes indicated by solid arrows and 1 less sensitive axis as dashed arrow (EGG-C, 2006).

The combination of the accelerations measured by the individual accelerometers provide some useful scientific products, such as Common Mode Accelerations (CMA) and Differential Mode Accelerations (DMA). CMA amounts to the mean average of the two accelerations of each arm, and it represents the external, non-gravitational forces that the satellite is subjected to. Hence, the CMA information is used by the electric propulsion system to continuously counteract (in a closed loop) the atmospheric drag in in-flight direction, so that the GOCE satellite is able to run in a drag-free mode and stays in its orbit. In contrast, DMA amounts to the mean deviation of the two accelerations of each arm, and it can be used to derive the gravity gradients by removing the effects of angular motion, e.g., the centrifugal motion and Euler motion (Rummel, 1986;

Müller, 2001; Cesare, 2008),

$$\Gamma = D - \Omega\Omega - \dot{\Omega}, \quad (4.1)$$

where Γ represents the gravity gradients, D are the differential mode accelerations divided by the distance between the two accelerometers, Ω are the angular velocities, the centrifugal part and Euler part are denoted as $\Omega\Omega$ and $\dot{\Omega}$, respectively. The angular velocity and acceleration can be derived from an optimised combination of the star tracker observations and the DMA. This is beyond the scope of this dissertation, more details can be found in the thesis of [Stummer \(2013\)](#).

EGG can theoretically provide nine gravity gradient components. These gradient components form a tensor that can be expressed by a 3×3 matrix in a Cartesian coordinate system as

$$\Gamma = \begin{bmatrix} V_{xx} & V_{xy} & V_{xz} \\ V_{yx} & V_{yy} & V_{yz} \\ V_{zx} & V_{zy} & V_{zz} \end{bmatrix}. \quad (4.2)$$

In practice, however, only six of these nine gradients (the upper triangular components) are actually delivered since the gravity gradient tensor is symmetric (one of the basic properties of the Earth's gravitational field, cf. [Stummer \(2013\)](#)).

In addition, as depicted in [Fig. 4.1](#), each accelerometer mounted on the gradiometer has two ultra sensitive axes with a precision of $10^{-12} \text{ ms}^{-2}/\sqrt{\text{Hz}}$ and one less sensitive axis with a precision of $10^{-10} \text{ ms}^{-2}/\sqrt{\text{Hz}}$. Because V_{xx} , V_{yy} , V_{zz} and V_{xz} are only determined from the ultra sensitive DMA, they are delivered in a high accuracy. In contrast, V_{xy} and V_{yz} are less accurate because they are influenced by at least one less sensitive DMA ([Gruber and Rummel, 2006](#); [Floberghagen et al., 2011](#); [Stummer, 2013](#)).

It is not possible to map the gravity field at all spatial scales with the same quality by using this gradiometer. In fact, the accuracy can only be ensured over the Measurement Band Width (MBW) which ranges from 5 mHz to 100 mHz. According to the pre-launch analysis, the root Power Spectral Density (PSD) of the trace of the main diagonal gradients is $11 \text{ mE}/\sqrt{\text{Hz}}$ in the MBW, cf. [Cesare \(2008\)](#). And outside the MBW, it shows an increase of $1/f$ towards lower frequencies and an increase of f^2 above MBW. The trace of the main diagonal gradients is theoretically zero (Laplace's equation), and in practice, it can be taken as error measure of the main diagonal gradients. Thus, the root PSD of the noise from the whole spectrum presents a typical behaviour of the coloured noise. In other words, the time series of the gravity gradients are not statistically independent. Their correlations must be considered in the LS adjustment, which poses a great challenge to GOCE gravity field recovery.

4.1.3 Overview of the recovering approaches for SGG data

The gravity gradient is a new type of observation that is used for gravity field recovery. In the past two decades, several methods have been developed to extract the gravity field signal from this type of observations. In this subsection, the main approaches are briefly reviewed.

1. Space-Wise approach

The main idea behind the space-wise (SPW) approach is to derive the SH coefficients of the gravity field by using the estimated grids of gravity gradients at mean satellite altitude (Migliaccio et al., 2010; Pail et al., 2011). The spherically gridded values are interpolated from the local patches of data by a sophisticated collocation algorithm (Reguzzoni and Tselfes, 2009). Then, a harmonic analysis by numerical integration is applied to derive the SH coefficients (Colombo, 1981). In this way, the numerical complexity is reduced. But an exact error covariance propagation is not feasible, as a consequence, the error covariance matrix of the estimated coefficients is derived by using Monte Carlo technique (Migliaccio et al., 2009).

2. Direct approach

The direct (DIR) approach solves the unknown SH coefficients from the band filtered gravity gradients in the framework of LS adjustment (Pail et al., 2011; Bruinsma et al., 2013, 2014). The normal equation systems of each short data segment (e.g., daily arcs) are assembled in parallel and then summed up. The resulting normal matrix is inverted to retrieve the SH coefficients, e.g., using Cholesky decomposition. With regard to the coloured noise, a bandpass filter is applied to the measurements to only use the information inside the MBW. The noise inside the MBW is approximately white (Cesare, 2008). Thus, the weight matrix in the LS adjustment is reduced to an identity matrix.

3. Time-Wise approach

The time-wise (TIM) approach treats the gravity gradients as time-series measurements along the satellite orbit (Pail et al., 2010, 2011; Brockmann et al., 2014) so that the high correlation of observations has to be taken into account in the LS adjustment. In difference to the direct approach applying a bandpass filter, the strategy of the time-wise approach is to decorrelate the observations over the entire bandwidth. A cascade of filters is designed for this purpose (Schuh, 2003; Siemes, 2008; Pail, 2014). After decorrelation, the noise of the observations is approximately white and the weight matrix in the LS adjustment is again treated as an identity matrix. The normal matrix is then assembled and inverted, similar to the direct approach. To avoid introducing any a priori informa-

tion, the decorrelated filters are usually constructed from the observation residuals. This means at least one iteration of the LS adjustment process is required.

4. Tensor invariants approach

The above-mentioned three approaches are performed at the level of individual gradients. The tensor invariants approach is an alternative strategy. The tensor invariants are formed by the combination of individual gradients (Baur et al., 2008). The tensor invariants are scalar-valued gravity field functionals and independent of the gradiometer orientation in space so that the transformation between different reference frames can be avoided (Baur et al., 2010). It also has some disadvantages. The combination of gradients may cause a loss of information because the vectorial equations are reduced into a scalar one. In addition, the stochastic model is more complex.

5. Torus approach

The Torus approach, also called semi-analytical approach, is usually classified as either space-wise or time-wise under certain approximations and assumptions (Sneeuw, 2000; Xu et al., 2008). It attempts to reduce the computational complexity of the gravity field recovery. Firstly, the time series of the observations are transformed to the spectral domain so that the Fast Fourier Transform (FFT) technique can be applied to increase the computational efficiency. Then, the normal matrix is reduced to be block diagonal under the assumption of a circular orbit. This saves memory and also time for the computation. Since this approach provides the solution quickly it is adopted as a quick-look gravity field analysis tool (Pail and Wermut, 2003; Pail et al., 2011).

From the above review, the differences between these approaches are mainly from three aspects: 1) the set up of the observational equations; 2) strategy to cope with the coloured noise of the observations; 3) numerical strategy to derive the SH coefficients. Among them, the SPW, DIR and TIM approaches have been adopted by the GOCE High Performance Facility (HPF) to derive the official models (Pail et al., 2011).

The approach applied in this dissertation is more or less the same as the TIM and DIR approach. The difference is given by the strategy to handle the coloured noise. Without applying any bandpass filter to the original observations or designing a cascade of filters to decorrelate the observations, instead, an appropriate stochastic model is applied in the LS adjustment. With this stochastic model, the observations are weighted and decorrelated. Since the true stochastic model is not available, it is computed empirically from the initial residuals.

4.2 The workflow of gravity field recovery from SGG data

Fig. 4.2 shows the workflow for the recovery of a gravity field model with a high spatial resolution based on GOCE SGG data. It separates the task of gravity field recovery into four modules, namely data understanding, data pre-processing, model recovery and model evaluation. These modules will be briefly introduced in this section and then explained in detail in the rest of this chapter.

In order to estimate gravity field coefficients, three types of data from four kinds of GOCE products are required. The most essential ones are the gravity gradients from the EGG_GGT_2 product. In addition, the orbit data from the SST_PRD_2 product is needed to geo-locate the gravity gradients, and the attitude quaternions from the SST_IAQ_2 and EGG_IAQ_2 products are required to construct the rotation matrices between different reference frames. The data input will be explained and analysed in detail in Section 4.3.

The observations have to be pre-processed before they can be used for the assembly of the normal matrix. First, the orbit and quaternions have to be interpolated to the epochs of gravity gradients. Then, the gravity gradients have to be processed to deal with anomalous observations, outliers and big data gaps. Finally, the data set should be down-sampled to reduce the time for computation. Details about pre-processing will be explained in Section 4.4.

The model recovery module deals with the determination of the unknown SH coefficients. This is the key module to derive the gravity field model. The main steps in this module include the assembly of the normal matrix, inversion of the normal matrix, calculation of the residuals and determination of the variance/covariance matrix. While the related algorithms have been introduced in Chapter 2, Section 4.5 is more concerned with the technical challenges of implementing these algorithms.

Finally, Section 4.6 presents the derived model with the determined SH coefficients and their formal errors. In addition, influences of various kinds of model settings are also compared and discussed. This comparison and discussion provide rich findings that will benefit future research and applications.

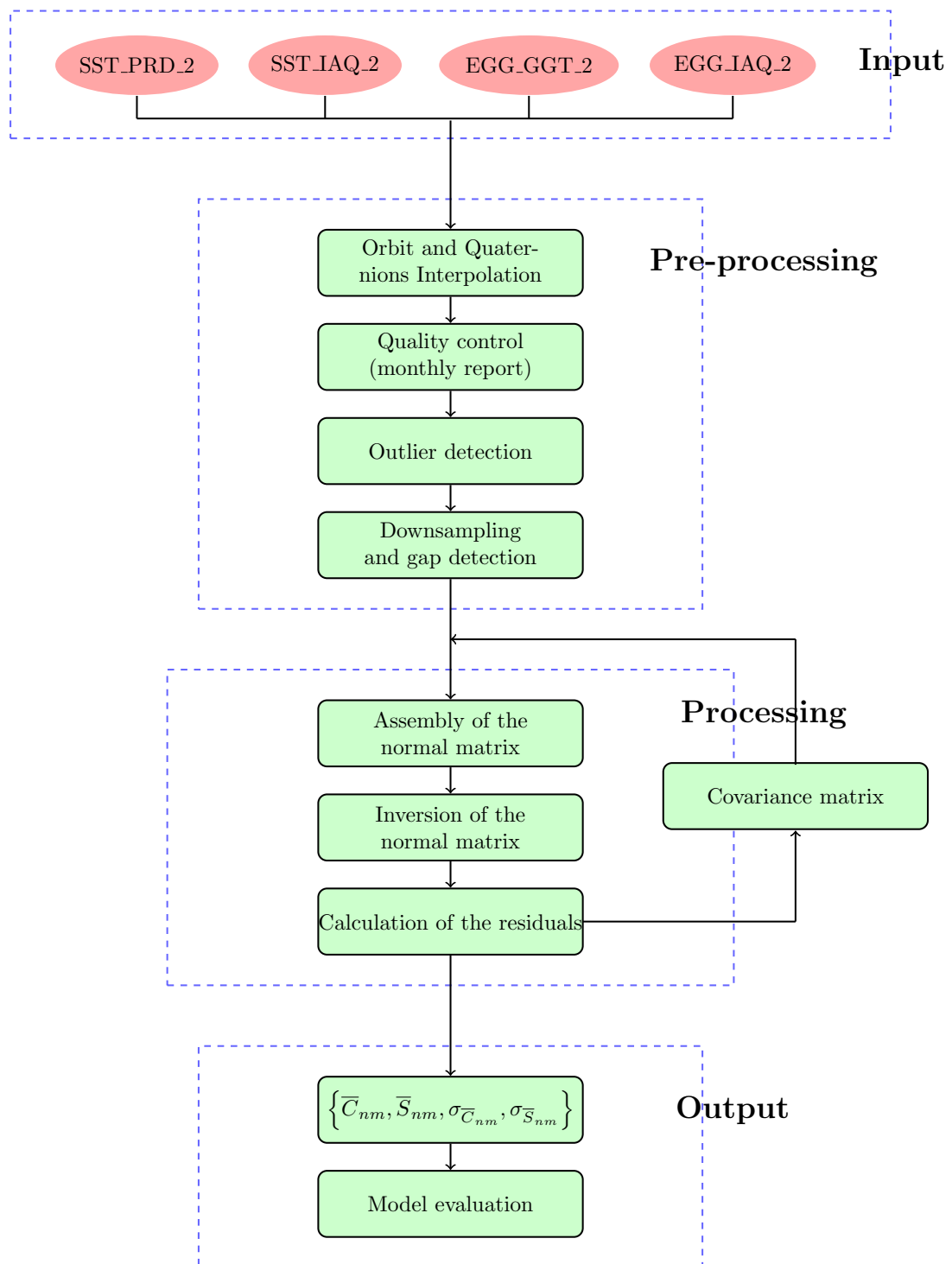


Figure 4.2: Flowchart of gravity field recovery from GOCE SGG data

4.3 Data understanding

The four types of GOCE products that will be used are explained in Section 4.3.1. Among the four products, gravity gradients from the EGG_GGT_2 product is the most essential one, and a comprehensive understanding of the gravity gradients is necessary for the recovery process. Therefore, Section 4.3.2 performs a thorough analysis of the Level 2 gravity gradients in the time, space and frequency domains. Additionally, Section 4.3.3 discusses the noise behaviour of the gravity gradient data as well as the strategy to handle the noise.

4.3.1 Data description

Spherical harmonic analysis from gravity gradients requires three types of data from four kinds of GOCE products, as listed in Section 4.2.

The gravity gradients, which are the core data of the recovery, are taken from the EGG_GGT_2 product, which is one of the GOCE Level 2 (L2) products. The L2 gravity gradients have been externally calibrated and can be directly used for gravity field determination (EGG-C, 2014). Although the L2 gravity gradients are provided in both the Gradiometer Reference Frame (GRF) and the Local North-Oriented Frame (LNOF), only the ones in GRF are applied for the recovery, because the ones in LNOF have external gravity field models introduced to compute the long-wavelength part of the gradients.

In addition, orbit data is required to geo-locate the gradients. The GOCE HPF provides two kinds of precise orbits: PKI and PRD. Both are at the same level of accuracy (Bock et al., 2014). The PKI orbit does not include any external gravity field information but is discontinuous with many data gaps, while the PRD solution is smooth and continuous but may introduce some external gravity field information. Since the orbit data here is only used for geo-locating, the contained external information will not affect the solution of gravity field. Therefore, the continuous PRD orbit is adopted for the geo-locating purpose.

Moreover, Inertial Attitude Quaternions (IAQ) are necessary to provide the rotation information between different reference frames. In this regard, the SST_IAQ_2 product provides the rotation information between Inertial Reference Frame (IRF) and Earth-fixed Reference Frame (ERF), and the EGG_IAQ_2 product provides the rotation information between GRF and IRF. Together, the mentioned rotation information enables the construction of the second-order derivatives of the gravitational model in GRF.

The GOCE satellite has delivered a huge amount of observations during its four years' scientific

mission. Based on these observations, ESA officially published five generations of gravity field models. The duration of observation periods for these five generations are approximately 71 days, 8 months, 16 months, 32 months and 48 months, respectively. More specifically, Table 4.1 lists the detailed duration periods for the official models with the ending date of the observations, since the starting date for all models is the same, it is November 1, 2009.

Table 4.1: Data volumes that are used for the recovery of the five generations of gravity field models (only the end dates are given)

	R1	R2	R3	R4	R5
TIM	01/11/2010	07/05/2010	04/17/2011	06/19/2012	10/20/2013
DIR	01/11/2010	06/30/2010	04/19/2011	08/01/2012	10/20/2013

For the purpose of pre-processing in Section 4.4, observations from November to December 2009 are used to conduct preliminary studies. For computing the gravity field model (Section 4.5), all GOCE observations are first grouped bimonthly to derive independent models of the gravity field, and then grouped again according to the timespan of the GOCE official models, to derive equivalent five generations of gravity field models. The evaluations of the derived models will then be discussed in Section 4.6.

4.3.2 Properties of the gravity gradients

Gravity gradients are measured by the gradiometer at a sampling interval of 1 s, thus they can be conveniently plotted in time-series graphs. The resulting graphs can clearly reveal basic properties of the gravity gradients, such as the magnitudes, the trend of changes, etc. These graphs are additionally useful for performance diagnosis of the observations. For example, they can be used to detect anomalous measurements or evident jumps (see Section 4.4 for detailed explanations).

Fig. 4.3 shows the time series of the gravity gradients for one single day (November 1, 2009). It comprises six subplots, with each subplot corresponding to one unique component of the gravity gradients, as explained in Section 4.1.2. According to the figure, the magnitudes of gravity gradients are about -800 E, -2760 E and 2500 E for the three main diagonal gradients (V_{xx} , V_{yy} and V_{zz}), and about -1570 E, -50 E and -28250 E for the other three components (V_{xy} , V_{xz} and V_{yz}). The observed magnitudes deviate from their theoretical counterparts, which are, for example, -1360 E, -1360 E and 2720 E for V_{xx} , V_{yy} and V_{zz} respectively¹. In practice,

¹The EGM2008 is chosen as the background model and truncated at d/o 360 to simulate the gravity gradients. The modelled values are considered as theoretical values. V_{xx} , V_{yy} have a magnitude of about -1360 E, V_{zz} of about 2720 E. V_{xz} , V_{yz} are about two orders of magnitude smaller, whereas V_{xy} is about three orders of magnitude smaller.

these deviations are treated as systematic errors and expected to be absorbed by empirical parameters in the LS adjustment. In addition, all the six subplots present 16 oscillations each day, which corresponds to the satellite's period of orbital revolution. According to Yi (2012b) and Stummer (2013), these oscillations are caused by the Earth's flattening and the eccentricity of the satellite orbit.

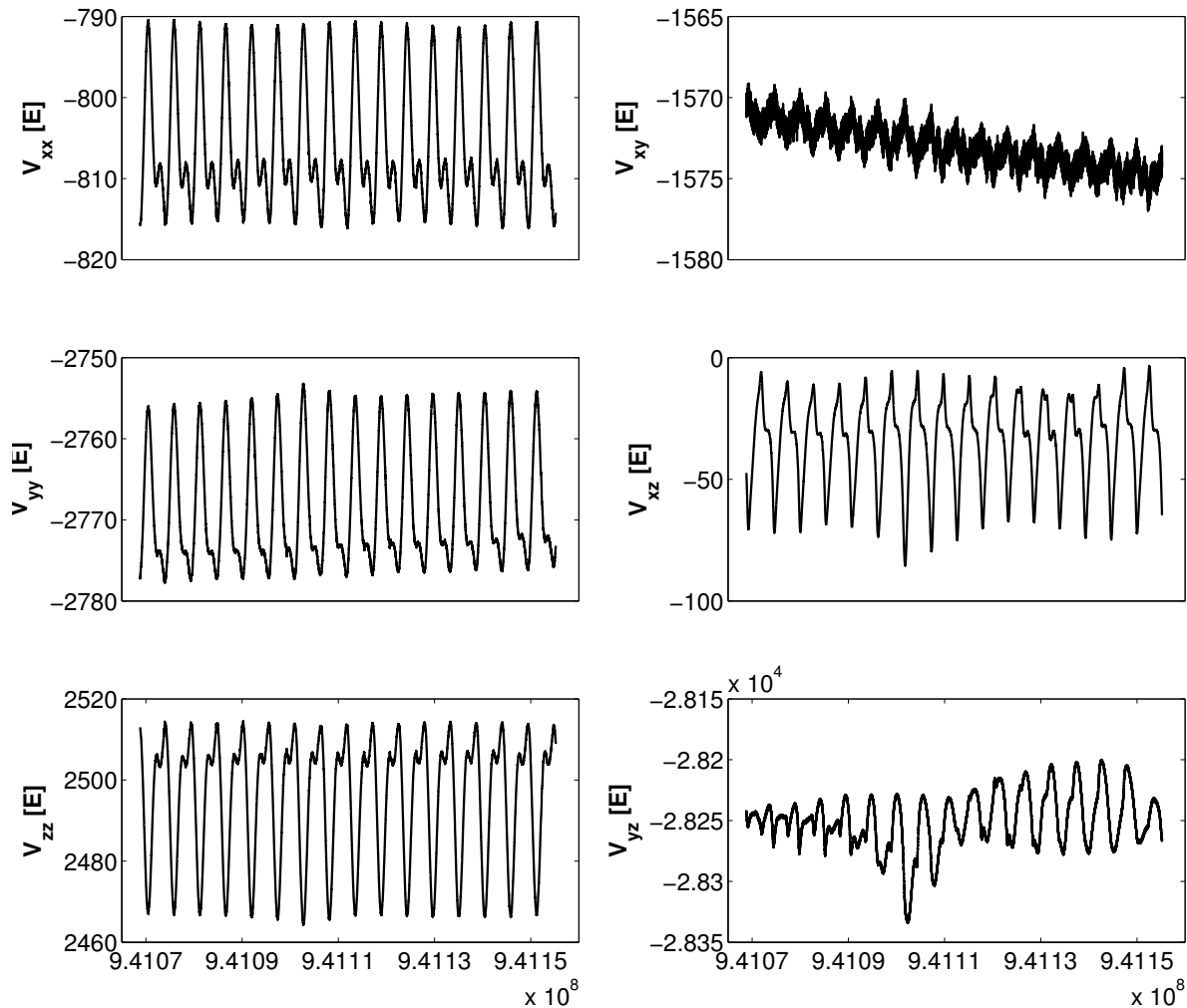


Figure 4.3: Time series of the gravity gradients on November 1, 2009

The above analysis in the time domain shows how the gravity gradients change over time. By applying a Fourier Transformation of the same time-series, further properties of the gravity gradients can be revealed in the frequency domain. The root PSDs of the six components are displayed in Fig. 4.4.

In general, the root PSD of V_{yy} is the smallest of the main diagonal gradient components. For frequencies higher than about 30 mHz and lower than about 200 mHz, the root PSDs are approximately flat, with a level of about $10 \text{ mE}/\sqrt{\text{Hz}}$ for V_{xx} , V_{yy} and about $20 \text{ mE}/\sqrt{\text{Hz}}$ for V_{zz} . At the lower part of the MBW (between 5 mHz and 30 mHz), the gravity field contribution

(signal and noise) starts from about $1000 \text{ mE}/\sqrt{\text{Hz}}$ at 5 mHz and decreases to a level of $10 \text{ mE}/\sqrt{\text{Hz}}$ with a rather steep descent. Below the MBW, the root PSDs show periodic distortions at one cycle per revolution (cpr) and multiple cprs, which is induced by the orbital revolution². Beyond the MBW (above 200 mHz), the root PSDs decrease sharply to a low level so that the contribution from this spectral band can be neglected. The frequency-domain behaviour of the other highly accurate component V_{xz} is similar to the main diagonal gradients, see Fig. 4.4(b). The root PSDs of the two less accurate components V_{xy} and V_{yz} are flat between 5 mHz and 200 mHz, with a magnitude of about 600 and 800 $\text{mE}/\sqrt{\text{Hz}}$, respectively. The different behaviour of V_{xy} and V_{yz} compared with those of the other four components again demonstrates that the gradients V_{xy} and V_{yz} are heavily affected by measurements with less accurate EGG axes, thus are not qualified for gravity field recovery.

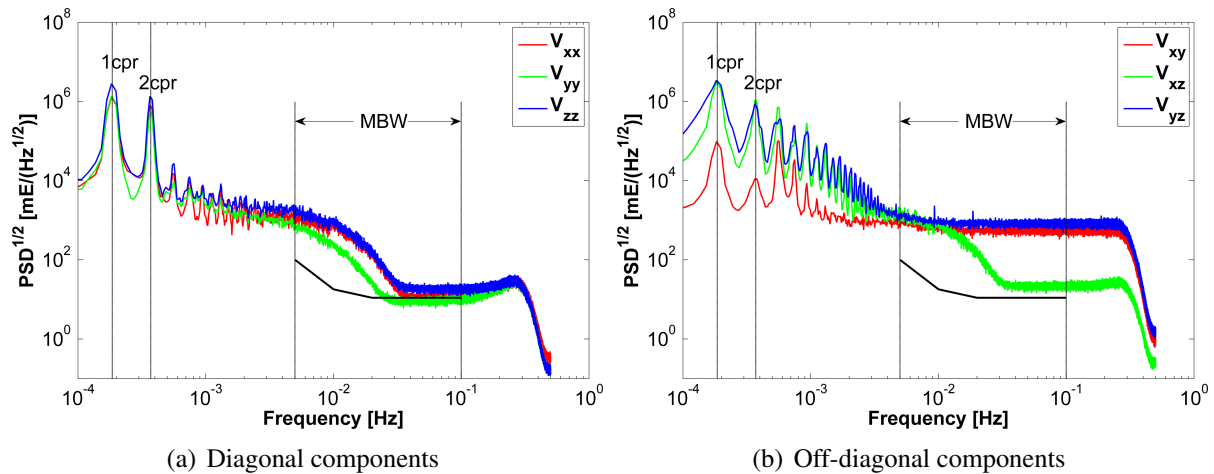


Figure 4.4: Root PSDs of the gravity gradients on November 1, 2009

In order to reveal how the gravity gradients change in space, further analysis is carried out in the space domain. Fig. 4.5 depicts the spatial distribution of the gradient tensor on November 1, 2009. According to the figure, the magnitudes and trends of the measurements between adjacent tracks are consistent for the four accurate components and significantly inconsistent for the two inaccurate components. Regarding the main diagonal gradients, their minimal values appear in the high-latitude regions of the southern hemisphere which corresponds to the highest altitude of the GOCE orbit, while their maximal values appear in the regions near the equator which corresponds to its lowest altitude. It is mainly caused by the orbit eccentricity. This indicates that the magnitudes of V_{xx} , V_{yy} , V_{zz} are negatively correlated with the altitude of the satellite. Moreover, the measurements in ascending passes are significantly different from those in descending passes. This is due to the different orientation of the gradiometer in ascending and descending passes. Since the gravity gradients observed from both passes at the

²One satellite revolution takes 5384 s. Thus, one cpr corresponds to the frequency of 1.86×10^{-4} Hz.

same point should be identical, the observations in the cross-over points can be compared to assess the quality of the gravity gradients (Brieden and Müller, 2014).

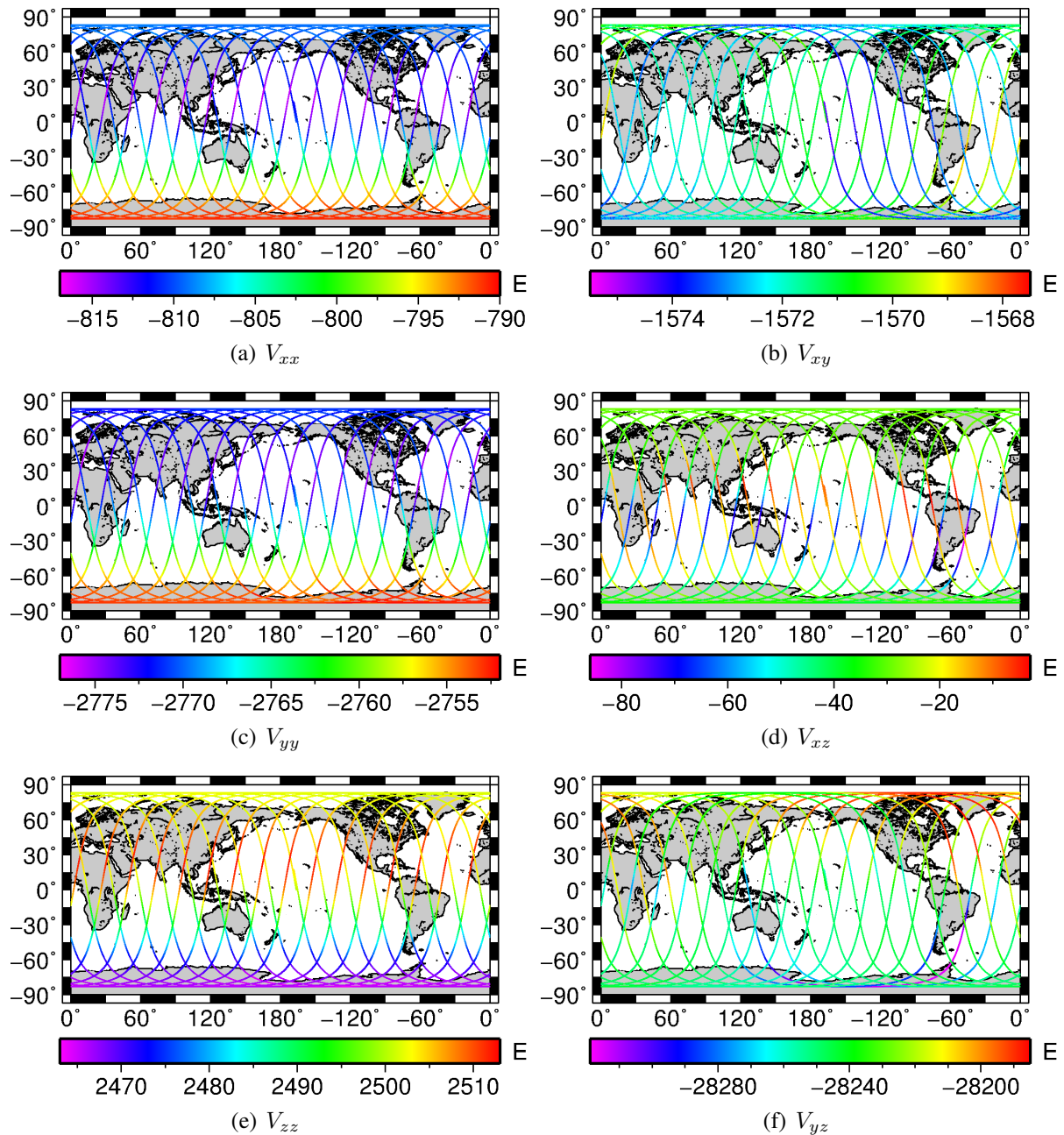


Figure 4.5: Spatial representation of the gravity gradients on November 1, 2009

4.3.3 Noise behaviour of the gravity gradients

In theory, the trace of the main diagonal gradient components fulfils the Laplace's condition (Rummel, 1986; Hofmann-Wellenhof and Moritz, 2006), i.e.,

$$V_{xx} + V_{yy} + V_{zz} = 0. \quad (4.3)$$

However, this theoretical equation does not hold true for the real observations because of the errors in the measurements. More specifically, the sum of the main diagonal gradients is often regarded as indicator of the magnitude of the measurement errors. It is a useful tool to analyse the noise behaviour of the gravity gradients.

The noise of the gravity gradients has been already identified as coloured in the pre-launch phase, when the requirements of the error spectral density of the trace was defined (Cesare, 2008). This coloured feature of the noise is further confirmed by the real observations, as shown in Fig. 4.6(a).

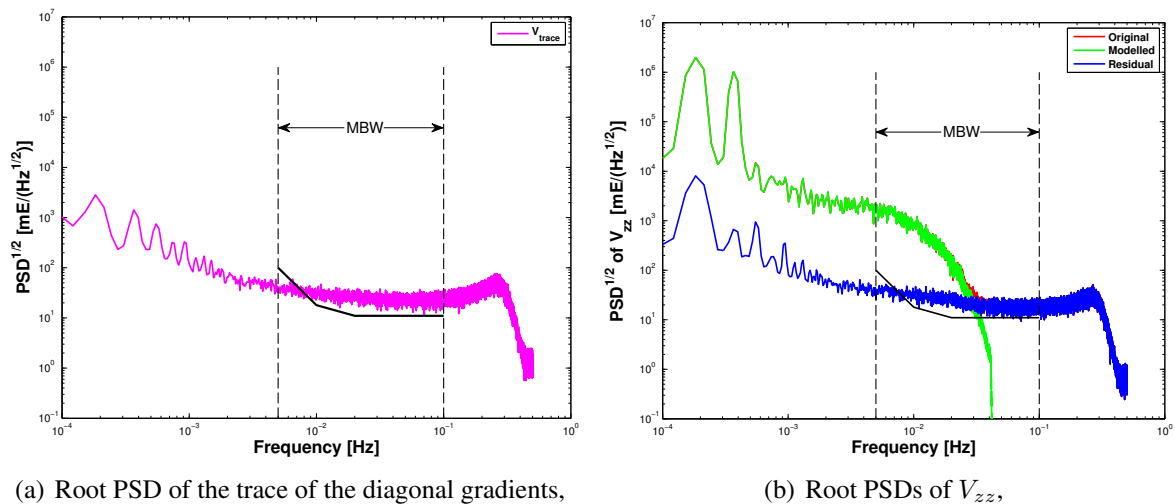


Figure 4.6: Coloured noise behaviour of the gravity gradients

Fig. 4.6(a) shows the root PSD of the trace of the diagonal gradients on November 1, 2009. The root PSD of the trace in the upper part of the MBW (above 30 mHz) is about $20 \text{ mE}/\sqrt{\text{Hz}}$, which is slightly higher than the expected value of $11 \text{ mE}/\sqrt{\text{Hz}}$. Over this part, the root PSD is almost flat that indicates the noise is approximately white. Towards the lower part of the MBW, the noise increases slightly and reaches about $60 \text{ mE}/\sqrt{\text{Hz}}$ at 5 mHz, which is below the level of the pre-defined performance of $100 \text{ mE}/\sqrt{\text{Hz}}$. It confirms that the main diagonal gradients in the MBW have high quality (the same conclusion can also be drawn for V_{xz}). Below the MBW, the noise increases with a $1/f$ characteristic. And some periodic distortions are superimposed

that are induced by the orbit and altitude periodic effects at one cpr and multiple cprs. Above the MBW, the noise shows a slight increase first and then a sharp decrease, that may be caused by low-pass filtering in the internal processing before publishing the gradient products.

Although the root PSD of the trace of the diagonal components indicates the high quality of the measured gradients, it only presents the combined error of the three components V_{xx} , V_{yy} and V_{zz} . Based on the Error Propagation Law, the variance of the trace is the sum of the variances of the three components, when assuming that the three components are independent. This is formally described as

$$\sigma_{V_{trace}}^2 = \sigma_{V_{xx}}^2 + \sigma_{V_{yy}}^2 + \sigma_{V_{zz}}^2. \quad (4.4)$$

In order to analyse the noise behaviour of each individual gradient component, the Observed Minus Computed (OMC) value should be used. Here, the computed gradients can be derived from an official reference model (e.g., EGM 2008) using the spherical harmonic synthesis. These computed gradients are considered as signals, while the OMC value as regarded as an estimation of the errors. Fig. 4.6(b) shows the root PSD of OMC values, taking V_{zz} as an example. The figure demonstrates that the spectral behaviour of the OMC V_{zz} is similar to that of the trace, only with a slight jump around 0.03 Hz due to the computed gradients are from the reference model with a truncated degree. Both figures in Fig. 4.6 show that the main diagonal gradient components are in high quality in the MBW.

Fig. 4.6 also shows that the noise below the MBW is higher for both the trace and the individual gradient. This indicates that the noise at the lower frequencies must be handled properly to ensure the extraction of the gravity field signal. Generally speaking, three approaches are widely used for this purpose. The most intuitive one is to remove the low-frequency noise with a bandpass filter. This approach has been successfully applied in the DIR approach where bandpass filters are designed for both the design matrix and the observations. Another strategy, that has been successfully applied in the TIM solutions, de-correlates the observations with various kinds of filters. The third approach handles the low-frequency noise by first removing all low-frequency observations with a high-pass filter and then restoring them using modelled signals.

In line with the TIM approach, the second strategy is applied here. However, instead of the commonly used filters, e.g., ARMA filter, this dissertation applies the variance/covariance matrix (VCM) of the observations in the LS adjustment, where the VCM can be used to down-weight and de-correlate the observations. As the true VCM cannot be obtained, empirical VCMs that are computed from the initial residuals of the observations are applied.

Similar to the normal matrix that is assembled arc-wisely to enable parallel computation and the integration of empirical parameters, the empirical VCMs are also computed arc-wisely. The observation residuals in one arc is denoted as $[v_0 \ v_1 \ \dots \ v_{N-1}]$, where N is the length of arc. Correspondingly, the empirical auto-covariance vector is written as

$$r = [r_0 \ r_1 \ \dots \ r_i \ \dots \ r_{N-1}], \quad (4.5)$$

where the individual auto-covariance r_i is estimated from the residual observations as

$$r_i = \frac{1}{N} \sum_{n=0}^{N-1-|i|} v_n \cdot v_{n+i}, \quad (4.6)$$

or

$$r_i = \frac{1}{N - |i|} \sum_{n=0}^{N-1-|i|} v_n \cdot v_{n+i}. \quad (4.7)$$

Eq. (4.6) provides a biased estimation of r_i while Eq. (4.7) provides an unbiased one. A comparison of these two kinds of estimations can be found in [Koch et al. \(2010\)](#), where the authors recommend the biased version which is also adopted in this dissertation.

Alternatively, the co-variance vector can be computed from the inverse Fourier transformation of the PSD of the residuals. This is based on the Wiener-Khinchin theorem, which points out that the spectral density and the auto-covariance function form a Fourier transformation pair. This approach is applied by, e.g., [Schall et al. \(2014\)](#). Nevertheless, these two approaches are essentially the same and can be used in practice at ease.

Assuming that the covariance between the observations with the same distance is identical, i.e.,

$$r_1 = r_{v_1, v_2} = r_{v_2, v_3} = \dots = r_{v_{n-2}, v_{n-1}}, \quad (4.8)$$

the VCM is thus constructed based on the auto-covariance vectors as

$$\Sigma = \begin{bmatrix} r_0 & r_1 & r_2 & \dots & r_{N-1} \\ r_1 & r_0 & r_1 & \dots & r_{N-2} \\ r_2 & r_1 & r_0 & \dots & r_{N-3} \\ \vdots & \vdots & \vdots & \ddots & \vdots \\ r_{N-1} & r_{N-2} & r_{N-3} & \dots & r_0 \end{bmatrix}. \quad (4.9)$$

Eq. (4.9) shows that the VCM is a Toeplitz matrix that is symmetric and positive definite ([Schuh, 1996](#)). Hence, the VCM can be decomposed into a multiplication of two triangular

matrices with the Cholesky method. The triangular matrix then works to de-correlate the observations and the design matrix. More about the decorrelation is discussed in Section 2.2.4.

4.4 Pre-processing of the gravity gradients

In order to obtain high-quality input for the gravity field recovery, the gravity gradients must be pre-processed. The main tasks of preprocessing include the removal of the anomalous observations, the detection of outliers and the examination of big data gaps. Each of these tasks is discussed separately in this section.

4.4.1 Removal of anomalous observations

According to the monthly quality reports of the GOCE Level 1b product that is available on the official website³, special events, such as beam-out events, anomalous oscillations, etc., happen from time to time. These special events result in anomalous observations of gravity gradients that can potentially affect the gravity field recovery and should be removed from the raw data.

The anomalous observations caused by these special events are remarkably distinct from their adjacent observations and can be clearly identified in the time-series. For instance, according to the quality report, a beam-out event occurred on February 5, 2010. As a result, an anomalous oscillation can be observed at that date (Fig. 4.7(a)). Two days later, the accelerometers' control voltages show a series of spurious zeros, which corresponds to another special event in the quality report. As a consequence, extreme values of the gravity gradients are returned, which is depicted in Fig. 4.7(b).

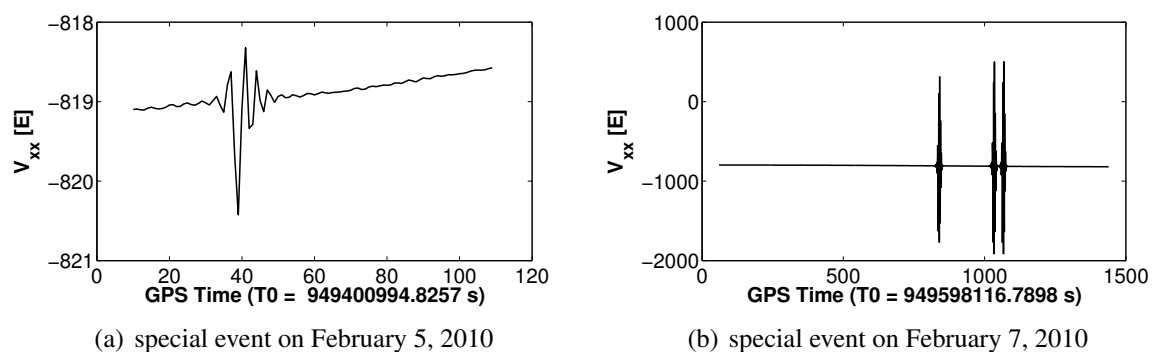


Figure 4.7: Time series plot of gradients, with anomalous observations on February 5 and 7, 2010

Hence, with the help of the monthly quality reports and the time-domain analysis of the observed gradients, it is straightforward to identify and remove the anomalous observations.

³<https://earth.esa.int>

4.4.2 Detection of outliers

Studies have demonstrated that even a small number (e.g., $< 0.2\%$) of undetected outliers of the gravity gradients can have adverse influences on the coefficient estimates (Kern et al., 2005). Thus, the outliers have to be identified and removed from the raw gravity gradients.

In the literature, several kinds of methods have been applied to identify the outliers of the gravity gradients, such as statistical methods, the wavelet outlier detection algorithm (Kern et al., 2005) and track-wise and area-wise approaches (Albertella et al., 2000). This dissertation applies the statistical method with moving windows, and identifies the outliers by setting both the upper and lower bounds in each moving window.

According to Albertella et al. (2000), the signal-to-noise ratio of the observations should be decreased so that the outliers could have a more distinct visual appearance. Thus, instead of the observed gradients, residual gradients, i.e., the OMC gradients, are used for outlier detection, where the computed gradients are obtained from the EGM2008 up to d/o 220. The outliers in a moving window w of size m are formally defined as:

$$out(\mu_m, \sigma_m, k, m) := \{i = 1, \dots, m : |x_i - \mu_m| > k\sigma_m\}, \quad (4.10)$$

where $x_i = \{x_1, \dots, x_m\}$ are OMC gradients in the window, μ_w and σ_w are estimates of the mean and standard deviation of OMC gradients in the same window, and the parameter k determines the range of the threshold region.

Eq. (4.10) shows that the result of outlier detection relies heavily on the settings of the parameters k and m . The parameter k is often set as a positive integer. A smaller k enables a more sensitive detection of outliers with the drawback that also some correct measurements are removed. Common settings for m are 1, 2, 4, 8, 16 revolutions, where each revolution corresponds to observations of 5400 s. In general, a smaller m enables a better tolerance of systematic errors at the cost of insufficient sampling points. Based on the comparison of a group of detection results with various settings of k and m , they are empirically set as 4 and 1 revolution, respectively.

With the specified settings, less than 0.1% of the observations are identified as outliers. For instance, among the gradients from 5,251,244 total epochs for November and December 2009, 374 of them are identified as outliers. The spatial distribution of these outliers are depicted in Fig. 4.8 as blue points. The identified outliers are then removed from the observations so that they would not affect the gravity field recovery.

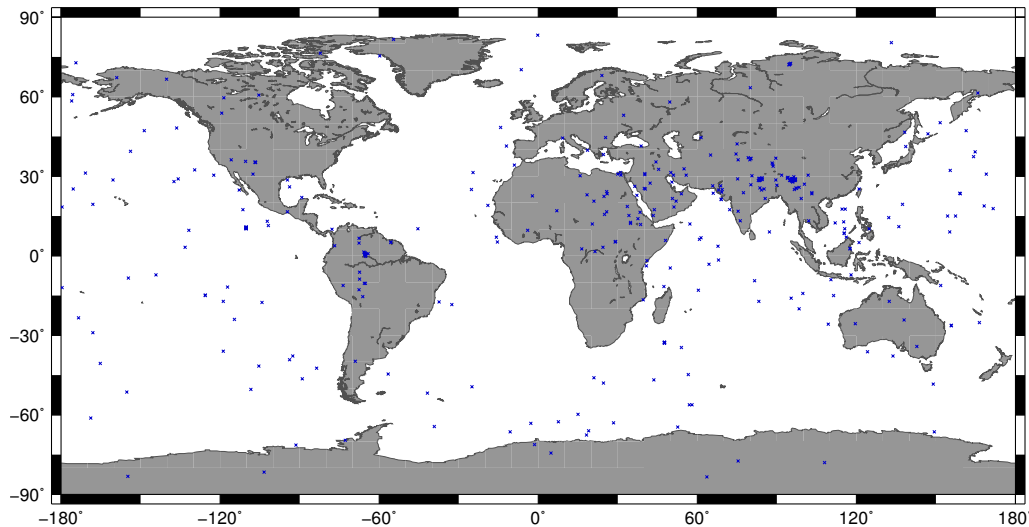


Figure 4.8: Spatial distribution of the outliers in November and December 2009, represented by the blue dots

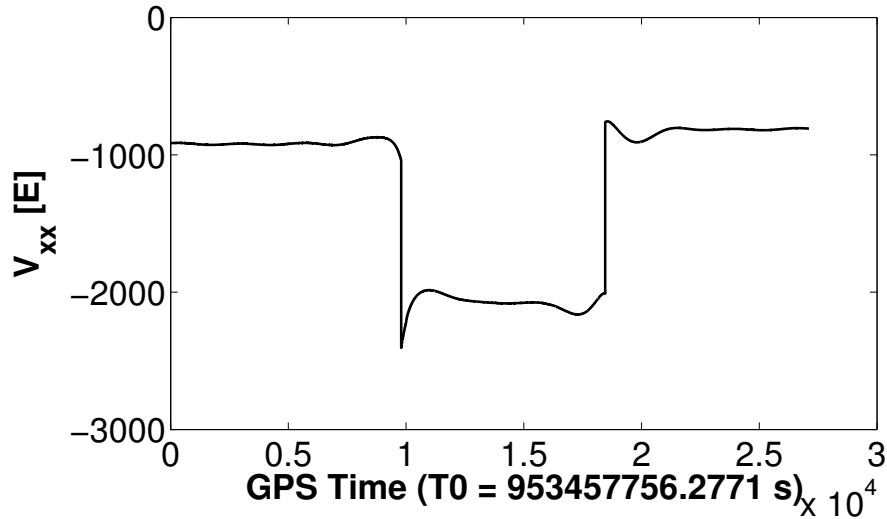
4.4.3 Examination of big data gaps

After the removal of anomalous observations and outliers as described in the previous two sections, the remaining measurements can be regarded as “clean” input for gravity field recovery. However, they require further pre-processing because of the existence of big data gaps.

Data gaps widely exist in the data set. They can be caused by various reasons, such as the calibration of the gradiometer, anomalies of the instruments (e.g., the science operations were interrupted by a severe anomaly of the GPS receiver that occurred in January 2011), the removal of the outliers, and so on. They also have different size. The influence of small data gaps (e.g., less than 10s) are believed to be negligible, while that of big ones is unpredictable. This is because systematic errors may not be consistent with the existence of big data gaps, thus they cannot be absorbed by the same empirical parameters. Therefore, big data gaps should be handled properly before gravity field recovery.

As mentioned in Section 2.3, the observations will be divided into short segments so that empirical parameters can be added to absorb the unknown systematic errors. This implies that the observations in each segment are supposed to have similar systematic errors, which does not hold true when the segment contains a big data gap.

For example, Fig. 4.9 shows a big data gap in March 2010. This data gap caused a remarkable drift of the V_{xx} component, with its magnitude slumped from -800 E to -2000 E. The empirical parameters estimated from a data segment with such a big gap are not reliable. In such cases a new segment should start to exclude the gap.

Figure 4.9: Data gap of V_{xx} in March, 2010

4.5 Model recovery

The previous module of data pre-processing provides “clean” gravity gradients for computing the gravity field model. Now, the unknown spherical harmonic coefficients will be determined. In this section, the functional model is described in Section 4.5.1, Section 4.5.2 explains the main steps and their coupling mechanisms. Although the algorithms for these main steps are introduced in Chapter 2, the huge amount of GOCE observations brings great challenges in the technical aspect. Thus, Section 4.5.3 deals with the technical challenges of implementing these algorithms.

4.5.1 Functional model

The gravity gradients V_{ij} are point-wise measurements of the second-order derivatives of the gravitational potential V

$$V_{ij} = \frac{\partial^2 V}{\partial x_i \partial x_j}. \quad (4.11)$$

They are delivered in the Gradiometer Reference Frame (GRF) which is defined by the axes x_i , with $i, j = 1, 2, 3$ denoting the X, Y and Z direction of the GRF. The gravitational potential is represented by a spherical harmonic series as described by Eq. (2.1), and its second-order derivatives in the Cartesian Coordinate system, e.g., LNOF, are given by Eq. (2.4). In order to set up the functional model, the observations, i.e., gravity gradients, and the base functions, i.e., the second-order derivatives of the gravitation potential, have to be transformed into the same reference frame.

Theoretically, the functional model can be set up in either LNOF or GRF. One option to unify the reference system is to transform the gravity gradients from GRF to LNOF, so that the functional model can be conveniently set up in LNOF. The shortcoming of this option is that the transformation of gravity gradients would map the less accurate components V_{xy} and V_{yz} into the accurate components, thereby affecting the accuracy of the recovered model (Fuchs and Bouman, 2011). Hence, the alternative option is applied, which transforms the base functions from LNOF to GRF and set up the functional model in GRF. In this way, the functional model can be written as

$$V_{ij} = R_{LNOF}^{GRF} V_{ij}^{LNOF} (R_{LNOF}^{GRF})^T, \quad (4.12)$$

where the rotational matrix R_{LNOF}^{GRF} is computed by

$$R_{LNOF}^{GRF} = R_{IRF}^{GRF} R_{ERF}^{IRF} R_{LNOF}^{ERF}. \quad (4.13)$$

The rotation matrices R_{IRF}^{GRF} between GRF and IRF, and R_{ERF}^{IRF} between IRF and ERF can be computed based on Eq. (2.8), with the quaternions given by the EGG_IAQ_2 and SST_IAQ_2 products. The matrix R_{LNOF}^{ERF} between ERF and LNOF is computed from the latitude and longitude of the satellite position following Eq. (2.7).

By introducing an initial observation, the functional model is written as

$$V_{ij} = V_{ij}^0 + \sum_{n=2}^N \sum_{m=0}^n A_{\hat{x}_{nm}} \cdot \hat{x}_{nm}, \quad (4.14)$$

where the initial gradients V_{ij}^0 are computed from a normal gravity field model. The SH coefficients $\bar{C}_{00}, \bar{C}_{20}, \bar{C}_{40}, \bar{C}_{60}, \bar{C}_{80}$ of EGM2008 are used to describe the normal gravity field in this dissertation. \hat{x}_{nm} are the unknown SH coefficients of degree n and order m . They are arranged in the sequence as

$$\hat{x}_{nm} = \{\bar{C}_{nm}, \bar{S}_{nm}\} = \{\Delta\bar{C}_{20}, \bar{C}_{21}, \dots, \Delta\bar{C}_{40}, \dots, \bar{C}_{nn}, \bar{S}_{21}, \dots, \bar{S}_{nn}\}. \quad (4.15)$$

Correspondingly, the coefficients $A_{\hat{x}_{nm}}$ are computed from

$$A_{\hat{x}_{nm}} = R_{LNOF}^{GRF} \frac{\partial V_{ij}^{LNOF}}{\partial \hat{x}_{nm}} (R_{LNOF}^{GRF})^T, \quad (4.16)$$

and with $\frac{\partial V_{ij}}{\partial \hat{x}_{nm}}$ in LNOF computed by

$$\begin{aligned}
\frac{\partial V_{xx}}{\partial \bar{C}_{nm}} + i \cdot \frac{\partial V_{xx}}{\partial \bar{S}_{nm}} &= \alpha [\bar{P}_{nm}''(t) - (n+1)\bar{P}_{nm}(t)] e^{i \cdot m\lambda}, \\
\frac{\partial V_{yy}}{\partial \bar{C}_{nm}} + i \cdot \frac{\partial V_{yy}}{\partial \bar{S}_{nm}} &= \alpha \left[\frac{\cos \theta}{\sin \theta} \bar{P}_{nm}'(t) - (n+1)\bar{P}_{nm}(t) - \frac{m^2}{\sin^2 \theta} \bar{P}_{nm}(t) \right] e^{i \cdot m\lambda}, \\
\frac{\partial V_{zz}}{\partial \bar{C}_{nm}} + i \cdot \frac{\partial V_{zz}}{\partial \bar{S}_{nm}} &= \alpha [(n+1)(n+2)\bar{P}_{nm}(t)] e^{i \cdot m\lambda}, \\
\frac{\partial V_{xy}}{\partial \bar{C}_{nm}} + i \cdot \frac{\partial V_{xy}}{\partial \bar{S}_{nm}} &= \alpha \left[\frac{m}{\sin \theta} \bar{P}_{nm}'(t) - \frac{m \cos \theta}{\sin^2 \theta} \bar{P}_{nm}(t) \right] e^{i \cdot (m\lambda + \frac{\pi}{2})}, \\
\frac{\partial V_{xz}}{\partial \bar{C}_{nm}} + i \cdot \frac{\partial V_{xz}}{\partial \bar{S}_{nm}} &= \alpha [(n+2)\bar{P}_{nm}'(t)] e^{i \cdot m\lambda}, \\
\frac{\partial V_{yz}}{\partial \bar{C}_{nm}} + i \cdot \frac{\partial V_{yz}}{\partial \bar{S}_{nm}} &= \alpha \left[\frac{m(n+2)}{\sin \theta} \bar{P}_{nm}(t) \right] e^{i \cdot (m\lambda + \frac{\pi}{2})},
\end{aligned} \tag{4.17}$$

where, $\alpha = \frac{GM}{R} \cdot \frac{1}{r^2} \cdot \left(\frac{R}{r}\right)^{n+1}$, $t = \cos \theta$.

After the partial derivative coefficients of the six gradient components are computed in the LNOF, they are assembled into a tensor matrix and then transformed into the GRF. For example, the coefficients $A_{\Delta \bar{C}_{20}}$ corresponding to the unknown parameter $\Delta \bar{C}_{20}$ in the GRF are computed by

$$\begin{pmatrix} A_{xx} & A_{xy} & A_{xz} \\ A_{yx} & A_{yy} & A_{yz} \\ A_{zx} & A_{zy} & A_{zz} \end{pmatrix} = R_{LNOF}^{GRF} \begin{pmatrix} \frac{\partial V_{xx}}{\partial \Delta \bar{C}_{20}} & \frac{\partial V_{xy}}{\partial \Delta \bar{C}_{20}} & \frac{\partial V_{xz}}{\partial \Delta \bar{C}_{20}} \\ \frac{\partial V_{yx}}{\partial \Delta \bar{C}_{20}} & \frac{\partial V_{yy}}{\partial \Delta \bar{C}_{20}} & \frac{\partial V_{yz}}{\partial \Delta \bar{C}_{20}} \\ \frac{\partial V_{zx}}{\partial \Delta \bar{C}_{20}} & \frac{\partial V_{zy}}{\partial \Delta \bar{C}_{20}} & \frac{\partial V_{zz}}{\partial \Delta \bar{C}_{20}} \end{pmatrix}_{LNOF} (R_{LNOF}^{GRF})^T. \tag{4.18}$$

The partial derivative coefficients for each accurate gradient component are then arranged in the same sequence as the unknown parameters to set up the coefficients vector or design matrix. The normal matrix can then be computed based on Eq. (2.12).

4.5.2 The main steps of model recovery

The model recovery module requires an iteration step to consider the empirical VCM in the recovery. In the first round, the normal matrix $\mathbf{N} = \mathbf{A}^T \boldsymbol{\Sigma}^{-1} \mathbf{A}$ is assembled by simplifying the VCM $\boldsymbol{\Sigma}$ as a unit matrix, because the a priori errors of the observations are unknown yet. Simultaneously, the parameter pre-elimination technique is applied to eliminate the empirical parameters from the normal equations, cf. Section 2.3. The normal matrices are computed in parallel on numerous processors and summed up to the full one. The full normal matrix is then directly inverted to derive the spherical harmonic coefficients, together with their standard de-

viations. The residuals are computed as an approximation of the true error of the observations. In the second round, an empirical VCM can be computed based on the residuals and used in the assembly of the normal matrix, and the de-correlation algorithm is applied to cope with the VCM, cf. Section 2.2.4. The resulting full normal matrix is inverted again to derive the estimates of the coefficients and the formal errors which serves as the final output.

4.5.3 Technical challenges

Resolving the global gravity field model is a challenging task because of its high computational requirements in terms of both time and memory. The computation in this dissertation is mainly accomplished by using the cluster system of Leibiz Universität IT Services (LUIS). Table 4.2 lists the details of the three main clusters that are employed for the computation.

Table 4.2: Available computing power of the three main clusters

name	number of nodes	cores per nodes	clock rate of each core	memory
Lena	80	16	2.4 GHz	64 GB
Tane	96	12	2.9 GHz	48 GB
Taurus	54	12	2.66 GHz	48 GB

Among the four main steps of gravity field model computation, the assembly of the normal matrix is the most time-consuming part. According to the theoretical analysis that is given in Section 2.2.3, it would take more than 500 days on a single-core microprocessor to assemble the normal matrix of one gradient component. Therefore, the technique of parallel computing must be introduced to assemble the normal matrix. With parallel computing techniques, multiple calculations can be carried out on different processing units at the same time. In this way, the overall computation time can be significantly reduced.

In order to enable parallel computing, preparations from several aspects are required. First, the observations have to be reasonably divided into a series of segments. Second, the results from the observation segments can finally be combined in a lossless way. Third, specialised libraries are required to optimize the computational efficiency. Fourth, dozens of independent processing units are indispensable. The first two requirements have been discussed in Chapter 2, explaining the algorithms to assemble the design matrix and normal matrix from a list of their partitioned blocks. Regarding the third requirement, the computational efficiency of two standard libraries, namely the Linear Algebra Package (LAPACK), cf. Anderson et al. (1999) and the Math Kernel Library (MKL, cf. Intel (2009)), is compared. To test the efficiency, the task of computing the inversion of a symmetrical matrix with a dimension of 4000×4000 by Cholesky Decomposition is done. The result shows that MKL is about five times faster than

LAPACK. The MKL is finally used. As for the fourth requirement, on average, about 40 jobs can be run simultaneously in the cluster of LUIS.

Under the condition that 40 jobs run simultaneously, and each job uses the most optimised library of MKL, the time needed to assemble the normal matrix of a single gradient component is shown in Fig. 4.10(a). The observations are taken from November to December, 2009 and down-sampled to an interval of 2 s.

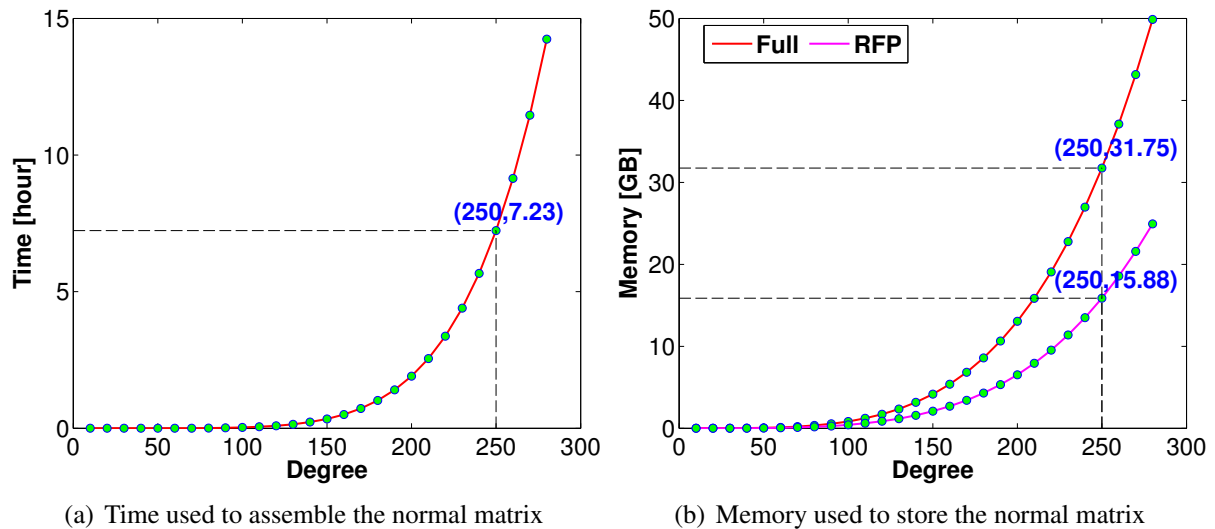


Figure 4.10: Time and memory that are required to assemble the normal matrix. The computation is based on a single gradient component from November and December, 2009. The sampling interval is reduced to 2 s.

Fig. 4.10(a) shows that the computational time increases with the truncated degree and order. If the model is resolved up to d/o 250, it takes about 7.2 hours for each job to assemble the normal matrix, while the exact time may slightly differ in different computation nodes of the cluster system. Thus, it requires about one week to assemble the normal matrix of one single gradient component for the entire four years' observations.

Assembling the normal matrix is not only the most time-consuming but also the most memory demanding task. For a model truncated at d/o 250, it requires more than 30 GB to store the normal matrix by the standard two-dimensional arrays. Storing only the upper or lower triangular part of the symmetric normal matrix instead of the full matrix by the standard packed format arrays can save almost half of the storage space. However, the computational performance is poor because no libraries support efficient computation with this packed format. To ensure both storage space and computational performance, a special format named the Rectangular Full Packed Format (RFPF) is employed. A symmetric matrix stored in RFPF requires only half of the space for the same matrix stored in the full standard format. In addition, RFPF can

provide a high computational performance (Gustavson et al., 2010).

Given that the matrix elements are stored in a double-precision floating-point format, Fig. 4.10(b) shows the space that is required to store the same normal matrix as in Fig. 4.10(a). It demonstrates that when the model is truncated at d/o 250, about 15.9 GB is required to save the normal matrix in RFPF, which is about half of the size of the full normal matrix.

4.6 Result Analysis

Following the approaches and algorithms that are explained in the previous sections, the global gravity field model can be obtained in the form of the determined SH coefficients together with the formal errors. The analysis of the models that are derived under different model configurations or from different groups of gravity gradients can provide valuable insight to the research field such as optimised model configurations, design of the satellite mission, etc. Therefore, this section performs a thorough analysis of the derived models to understand the influences of model configurations (Section 4.6.1), the contributions of each gradient component (Section 4.6.2), the influences of data volume (Section 4.6.3) and the effect of orbit altitude (Section 4.6.4). Section 4.6.5 then presents the final gravity field model that is purely derived from GOCE gravity gradients.

4.6.1 Effect of model configurations

Several questions regarding the model configurations can occur during the model recovery. For instance, what influence does the sampling interval have on the model accuracy and how should it be set? How should the length of the arc be set? How would the quality of the VCM affect the quality of the derived gravity field model? Answers to these questions will be given in this part, while they are essential for an accurate recovery of the gravity field model.

The designed sampling interval of the GOCE mission is 1 s. Thus, the satellite produced a huge amount of observations during its four years' lifetime. As explained in Section 4.5.3, the assembly of the normal matrix for such a huge amount of data is a very challenging task, even when parallel computing techniques are applied. A possible solution to this problem is to down-sample the original data and reduce the data amount. Prior to applying this solution, the influence of the down-sampling on the model accuracy must be determined, so that it is possible to find a balance between computation efficiency and model accuracy. To this end, the gradients of a single component, V_{zz} , between November and December 2009 are re-sampled at the intervals of 1 s, 2 s and 5 s. For the three data sets, gravity models are derived and compared in Fig. 4.11, which displays the Degree-Error RMS (DE-RMS) of the estimated coefficients

w.r.t. GOCO05s and the degree median. The zonal and near-zonal coefficients that are affected by the polar gaps are not used in the calculation of the DE-RMS, and will not be used in the following analysis of this chapter.

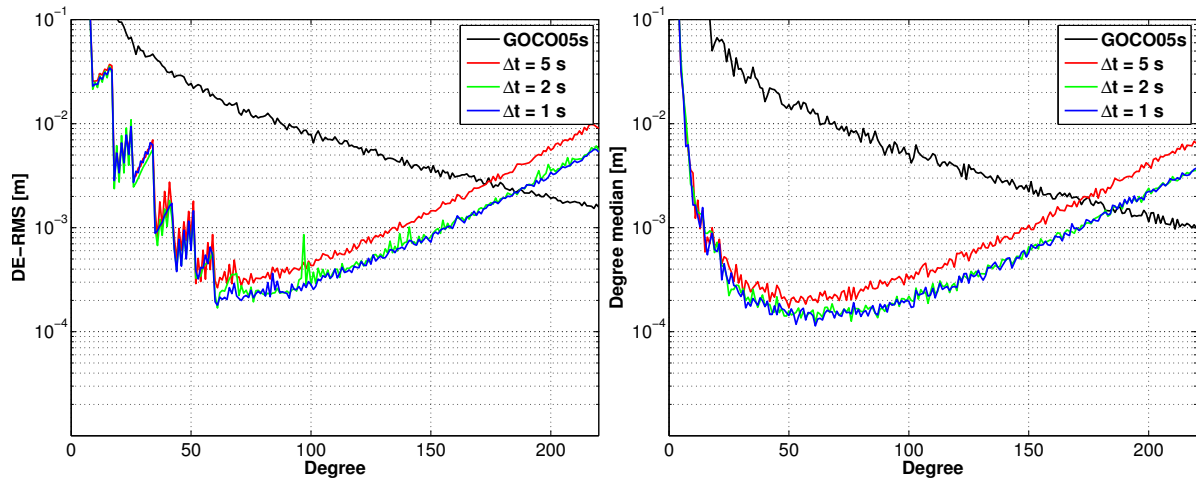


Figure 4.11: DE-RMS and degree median of the gravity field model recovered from V_{zz} with sampling intervals of 1 s, 2 s and 5 s. The time period is November and December 2009.

It is obvious that the performance of the solution derived from the data set with 5 s interval is poorer than the other two solutions, especially above d/o 50. The degradation approximately follows the $\frac{1}{\sqrt{N}}$ rule. The loss of observations has significant influence on the quality of the model for the 5 s data set. However, the accuracy of the solution based on the 2 s data set is only slightly lower than that for the 1 s data set. On the balance between the computational time and the accuracy, the original data is thus down-sampled to 2 s for the final gravity field determination in this study.

The assembly of the normal matrix is carried out arc-wise. Within each arc, the same empirical parameters are added to absorb the systematic errors, and only the correlation between the observations in the arc is considered. Thus, the length of the arc may affect the quality of the recovered model. To explore the effect of the arc length, Fig. 4.12 compared three gravity models with the arc length taken as 12 minutes, 15 minutes and 18 minutes, respectively. All three gravity models are recovered from the same gradient that is the V_{zz} component from November to December 2009.

According to the figure, the solution derived with an arc length of 18 minutes is slightly poorer than the other two solutions. Considering that the systematic errors in a longer arc tend to be more complicated, the poorer quality might be caused by the residual systematic errors that cannot be absorbed by the empirical parameters. The other two solutions show comparable performances. However, a shorter length of arc will introduce more empirical parameters in the recovery, which will increase the computational complexity. Additionally, more low-frequency

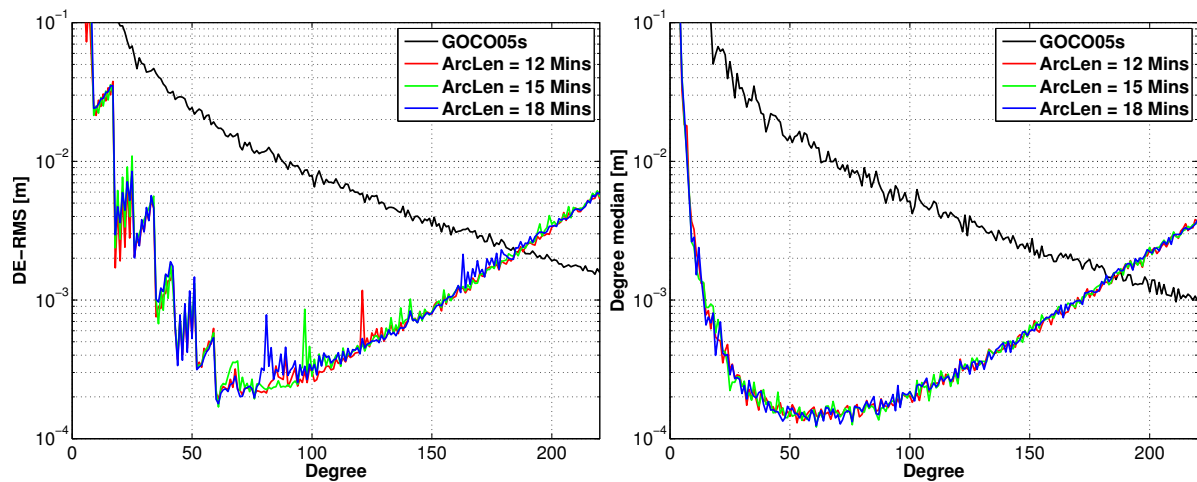


Figure 4.12: DE-RMS and degree median of the gravity field model recovered from V_{zz} with different arc lengths of 12 minutes, 15 minutes and 18 minutes. The time period is November and December 2009.

signals tend to be affected by the empirical parameters. Therefore, the length of the arc will be taken as 15 minutes in the following analysis of gravity gradients.

The coloured noise of the gravity gradients is supposed to be de-correlated by the VCM of the observations. Since the true VCM is not available, the empirical one estimated from the initial residuals is used. The effect of the VCM on the recovered model is shown in Fig. 4.13, where the solutions are derived from the observations of November and December, 2009. The four accurate gradient components are down-sampled to 2 s and used to derive the model with a maximum d/o of 220. The improvement of the solution is evident in both DE-RMS and degree median curves.

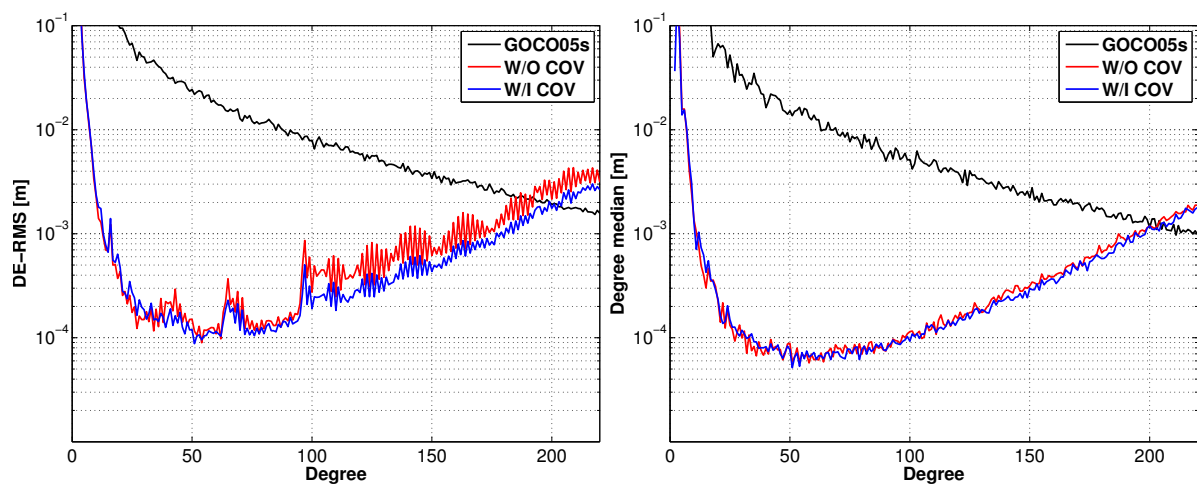


Figure 4.13: Comparison of the gravity field models recovered with and without consideration of VCM, left: DE-RMS, right: degree median

Furthermore, the quality of the empirical VCM should be considered. Since the VCM is estimated from the initial residuals, the accuracy of the residuals may affect the quality of the VCM, and thus the quality of the resulting gravity field model. A 8-month data set (from November 2009 to June, 2010) and the whole data set (from November 2009 to October 2013) are used to derive an a priori gravity field model, and the residuals are calculated correspondingly. Taking V_{zz} as an example, the 8-month data set is then used to derive the gravity field model by applying different VCMs (estimated from different residual sets). The gravity field models are determined up to d/o 250 and compared in Fig. 4.14. The gravity model derived from a superior VCM (the one estimated from 46-month data) has much better quality than the other, especially for the coefficients above d/o 50.

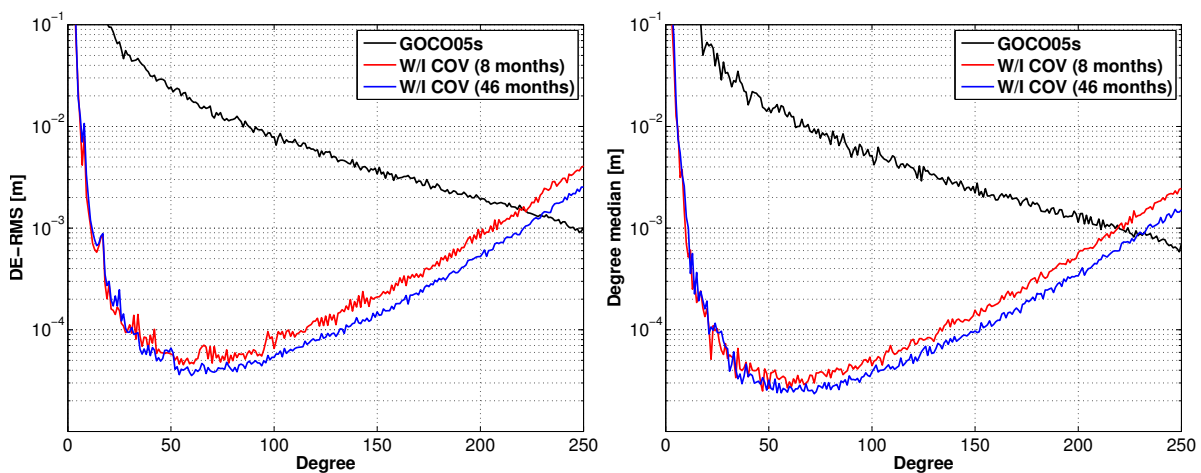


Figure 4.14: The effect of the quality of the VCM on the recovered gravity field models, left: DE-RMS, right: degree median

4.6.2 Contribution of each component

The individual spherical harmonic analysis of the four accurate gradient components is carried out based on the observations of November and December 2009. The original gradient data is down-sampled to 2 s and then used to recover a global gravity field model up to d/o 220. The two-dimensional error spectrum of the estimated coefficients is shown in Fig. 4.15 which includes the coefficient differences w.r.t. GOCO05S and the formal errors.

The results show that the four gravity gradients manifest similar patterns regarding both the coefficient differences and formal errors, while they are sensitive to different parts of the gravity field. For instance, V_{xx} is more sensitive to lower order zonal and near-zonal coefficients but less sensitive to higher order coefficients. In this regard, V_{yy} exactly complements V_{xx} with the inverse sensitivity. It contributes mainly to non-zonal coefficients, i.e., the sectorial coefficients and the higher order coefficients. The reason for the inverse and complementary

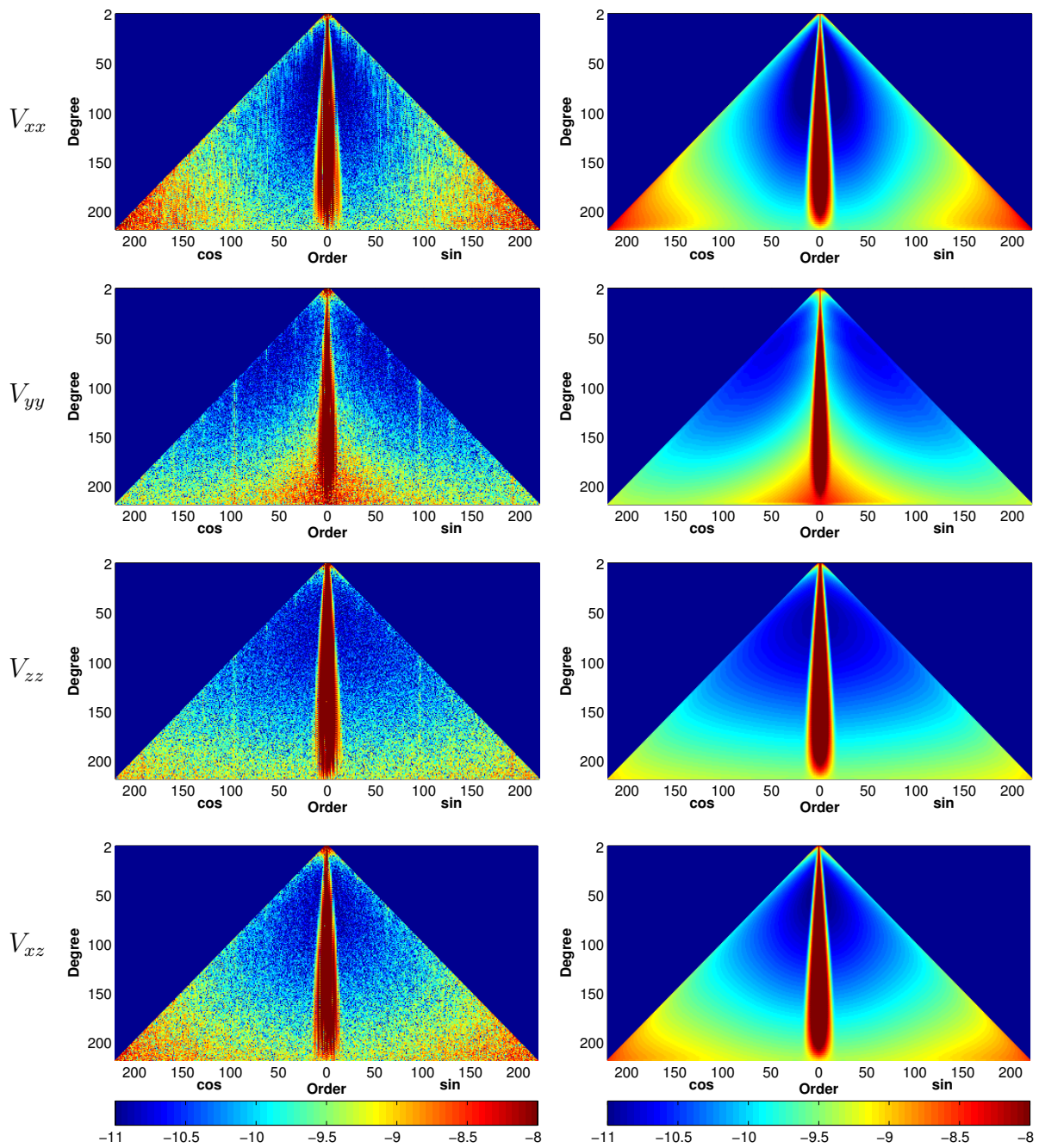


Figure 4.15: Two-dimensional error spectrum of the spherical harmonic coefficients estimated from the individual gradient components, V_{xx} , V_{yy} , V_{zz} , V_{xz} from top to bottom. Coefficient differences w.r.t. GOCO05S (left) and formal errors (right), both are unitless and shown in logarithmic scale.

sensitivity is related to the orientation of the corresponding accelerometer pairs. To be more specific, the accelerometer pair responsible for V_{xx} is oriented almost along track (Gruber and Rummel, 2006). It is mainly projected on the latitude direction since the GOCE satellite was in a near polar orbit with an inclination of 96.5° . The accelerometer pair of the component V_{yy} is approximately oriented in cross-track direction so that it measures the gravity field better in cross-track direction. Its contribution is mainly on the longitude direction. This orthogonal orientations of the two accelerometer pairs thus result in the inverse and complementary sensitivity of V_{xx} and V_{yy} .

Compared to V_{xx} and V_{yy} , V_{zz} is sensitive to all orders of coefficients. According to the Laplace's equation, i.e., Eq. (4.3), $V_{zz} = -(V_{xx} + V_{yy})$. The contribution of V_{zz} is then compared to that of the combination of V_{xx} and V_{yy} . The results are shown in Fig. 4.16. On the one hand, the pattern of V_{zz} coincides well with that of the combination of V_{xx} and V_{yy} . On the other hand, the accuracy of the coefficients estimated from the combination of V_{xx} and V_{yy} is higher than that from V_{zz} . The differences of the coefficients between the combined and individual analysis are presented in the bottom part of Fig. 4.16. They are mainly caused by the errors of V_{zz} .

The derivation of gravity gradients from Differential Mode Accelerations (DMA) suggests that in theory, V_{xz} approximately amount to the mean average of V_{xx} and V_{zz} after the separation of angular and centrifugal acceleration terms, cf. Stummer (2013). Fig. 4.17 compares the solution based on V_{xz} with that based on the combination of V_{xx} and V_{zz} . The result show that both solutions have similar patterns in the two-dimensional error spectrum. Both solutions contribute mainly to the coefficients of low order, especially zonal and near-zonal parts. However, the accuracy of the solution from the individual analysis of V_{xz} is lower than that from the combined analysis. The difference between the two solutions is depicted in the bottom of Fig. 4.17.

According to a quantitative analysis on the contribution of different types of observations to the final gravity field model, V_{xz} contributes smallest among the four accurate gradient components. More details of the quantitative analysis are already discussed in Yi (2012b); Yi et al. (2013). In order to reduce the computational burden, the contribution of V_{xz} is neglected in the following analysis of this chapter.

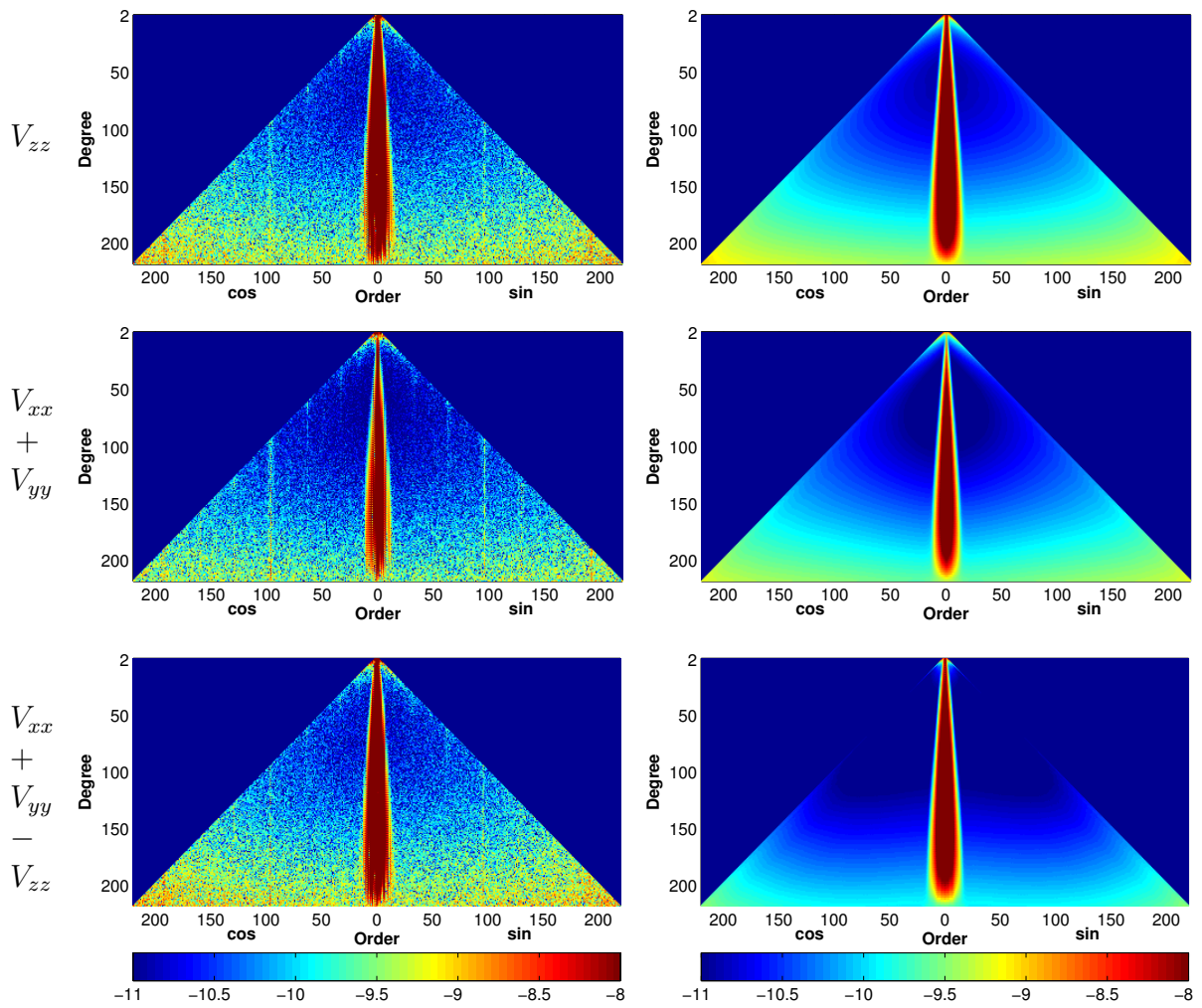


Figure 4.16: The top and middle panel are the two-dimensional error spectrum of the spherical harmonic coefficients estimated from V_{zz} and $V_{xx} + V_{yy}$, with coefficient differences w.r.t. GOCO05S (left) and formal errors (right). The bottom panel shows the difference of the two solutions.

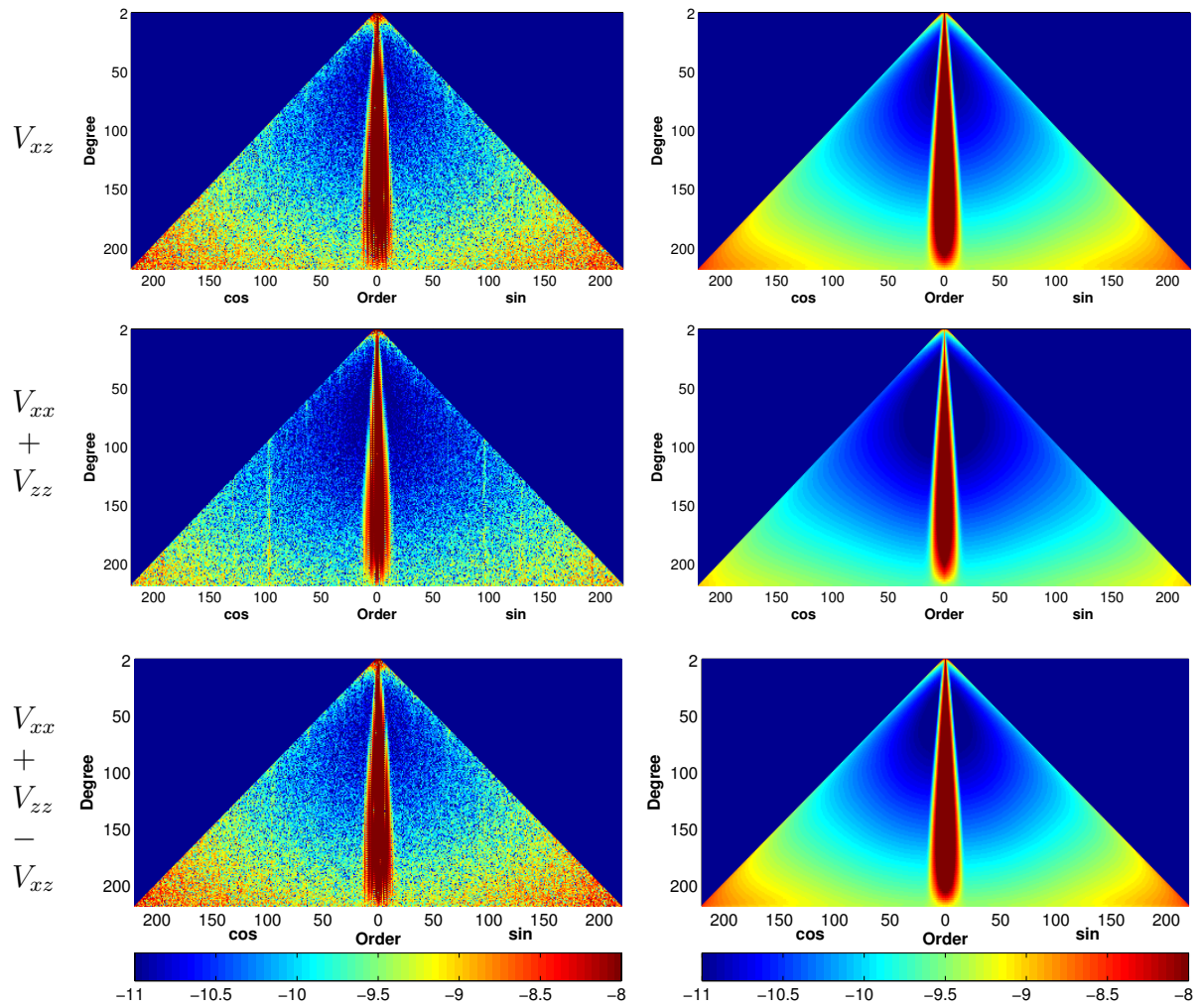


Figure 4.17: The top and middle panel are the two-dimensional error spectrum of the spherical harmonic coefficients estimated from V_{xz} and $V_{xx} + V_{zz}$, with coefficient differences w.r.t. GOCO05S (left) and formal errors (right). The bottom panel shows the difference of the two solutions.

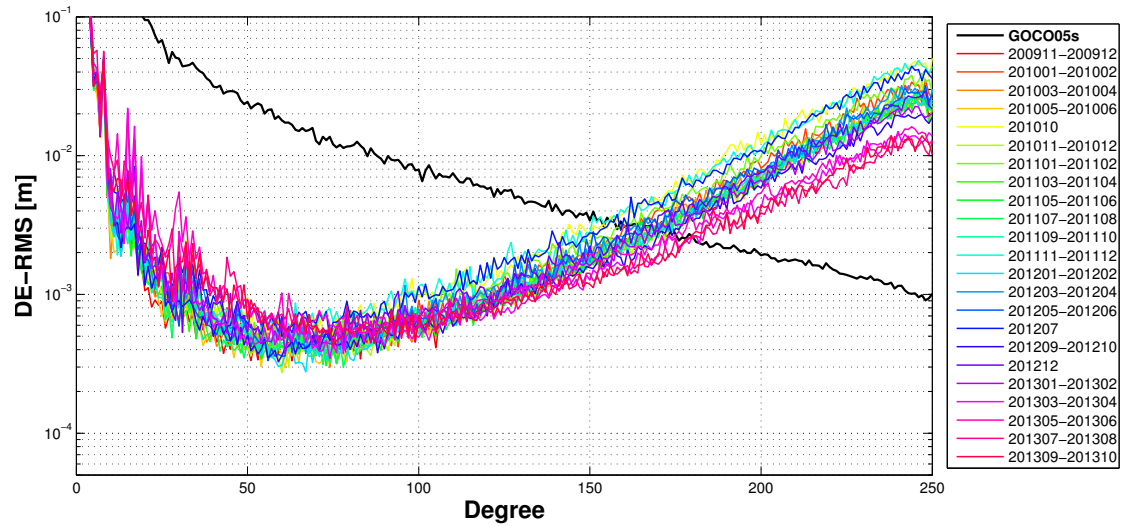
4.6.3 Results from different amounts of observations

The entire GOCE gravity gradients are grouped bimonthly because the satellite finished a repeat cycle in about every two months. The total four years' observations are thus divided into 23 groups except for the biggest data gap between July and September 2010. For each group, the normal matrix is assembled and inverted to derive an independent gravity field solution up to d/o 250. For the main diagonal gradient components, three groups of solutions are finally obtained. The DE-RMS of these solutions w.r.t. GOCO05S are depicted in Fig. 4.18. The result shows that every independent solution has a good consistency at the aimed frequency part, above about d/o 50. The performances of these independent solutions can be treated as a quick-look tool to diagnose the quality of the gravity gradients. In addition, Fig. 4.18 shows that the accuracies of solutions vary for every group. This is mainly caused by the number of observations used to recover the model is different. After removing the anomalous observations, outlier and data gaps, the number of observations of each group is different. The solutions that are recovered from a larger number of observations show superior performances. In addition, the observations at different altitudes have different signal-to-noise ratios. More specifically, the observations at the lowered orbit have large signal-to-noise ratios which further help to improve the accuracies of the high-degree coefficients. The influence of the satellite altitude on the recovered model will be discussed in detail in the next subsection.

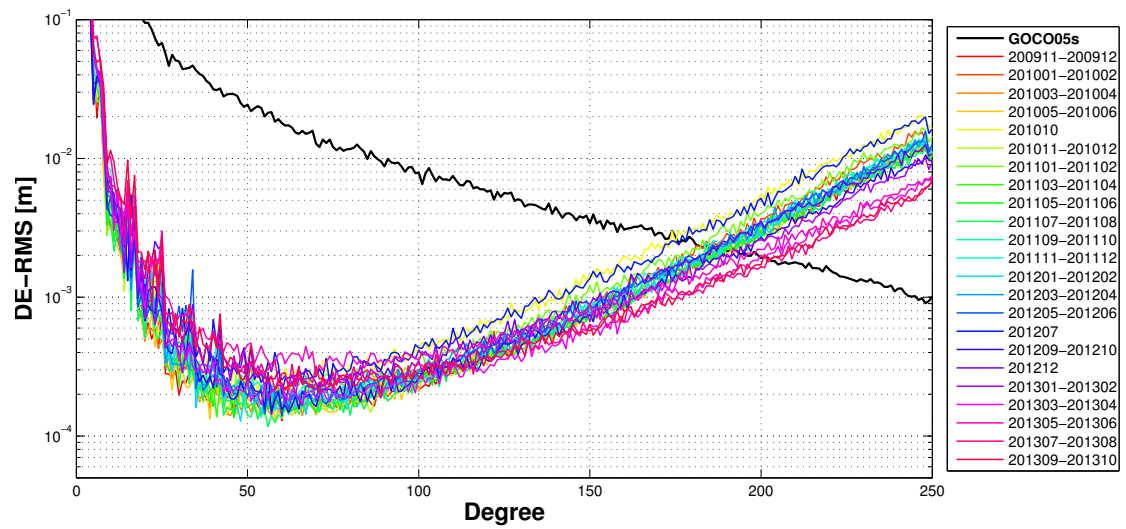
4.6.4 Analysis of the gravity gradients at the lowered orbit

Since the nominal and extended mission lifetime completed in July 2012, ESA performed multiple manoeuvres and gradually lowered the satellite's orbit from the designed altitude of 259 km to about 229 km, thereby increasing the sensitivity of the gradiometer to the gravity signal. The first three manoeuvres took place in August 2012, November 2012, and February 2013, and lowered the satellite by 8.6 km, 15 km and 20 km from its designed orbit. In between the manoeuvres, the satellite collected two 61-day cycles of data. After another 70-day cycle, ESA performed a fourth and final manoeuvre in May 2013, and lowered the orbit by another 10 km, which started a 143-day repeat cycle with 56-day sub-cycles. The daily mean altitudes of the GOCE satellite since July, 2012 are depicted in Fig. 4.19.

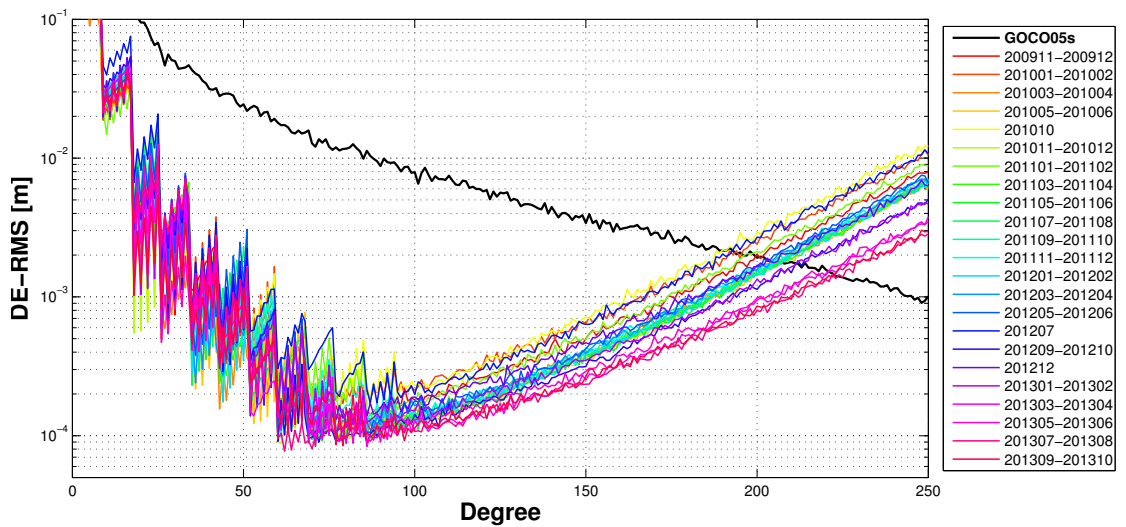
It is interesting to study the effect of the orbit altitude on the resulting global gravity field model, because it can provide useful insight for the design of future satellite missions. Therefore, this dissertation analyses the gravity gradients that are observed at different altitudes. The analysis is based on five groups of gravity gradients, with each group containing two months' observations. More specifically, the duration of these five groups are: March to April 2012



(a) solutions from V_{xx}



(b) solutions from V_{yy}



(c) solutions from V_{zz}

Figure 4.18: DE-RMS of the gravity field models that are recovered from bimonthly gravity gradients

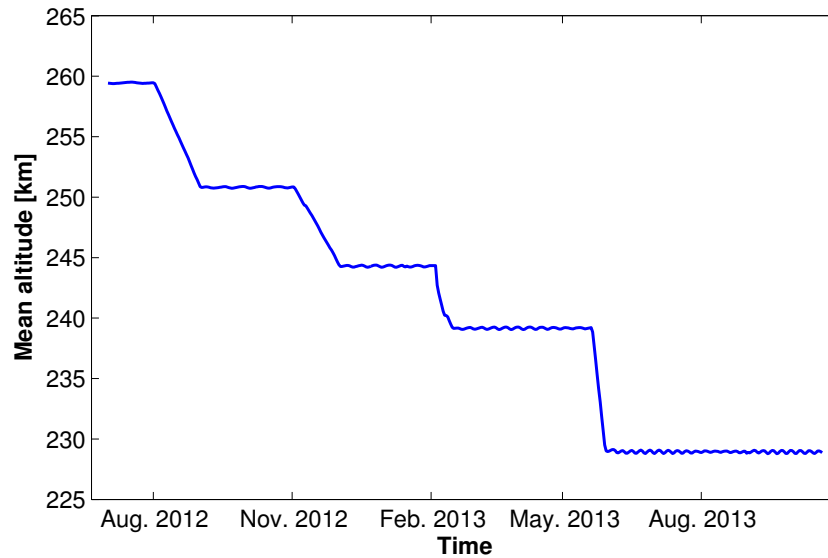


Figure 4.19: Daily mean altitude of the GOCE satellite since July, 2012

(altitude: 259 km), September to October 2012 (altitude: 250.4 km), December 2012 to January 2013 (altitude: 244 km), March to April 2013 (altitude: 239 km) and July to August 2013 (altitude: 229 km).

As the first step, the spectral behaviour of the main diagonal gravity gradients, V_{xx} , V_{yy} and V_{zz} for the five groups are compared in Figs. 4.20, 4.21, 4.22.

The root PSDs are mainly compared over the MBW since the contribution in this frequency part is most relevant due to mission specification. For the original gradients, the root PSDs in the lower part of the MBW (below about 40 mHz) are increased with the decrease of the orbit altitude. In order to confirm that the increase of the root PSDs is mainly caused by the strengthened signal instead of the noise, the OMC gradients which can be considered as the noise are also analysed. Here, the computed gradients are derived from the EIGEN-6C4 model which is truncated at d/o 360. The root PSDs of the OMC gradients show that the gradient noise of the five groups remains at the same level, especially for V_{xx} and V_{zz} . This implies that by lowering the orbit, the signal is really strengthened, and the signal-to-noise ratio is increased. It is thus foreseeable that the accuracy of the recovered gravity field will be improved. In addition, the quality of V_{yy} is severely affected by the solar activity. This is indicated by the root PSDs of OMC V_{yy} which behaves abnormal over the interested bandwidth.

Moreover, the gravity field models that were independently recovered from each of the five groups of gravity gradients are also compared. After pre-processing, the numbers of the epochs of each group are 2,317,095, 2,500,394, 1,915,531, 2,624,100, 2,250,045. These observations are used to derive models up to d/o 250. Fig. 4.23 shows the DE-RMS and degree median of

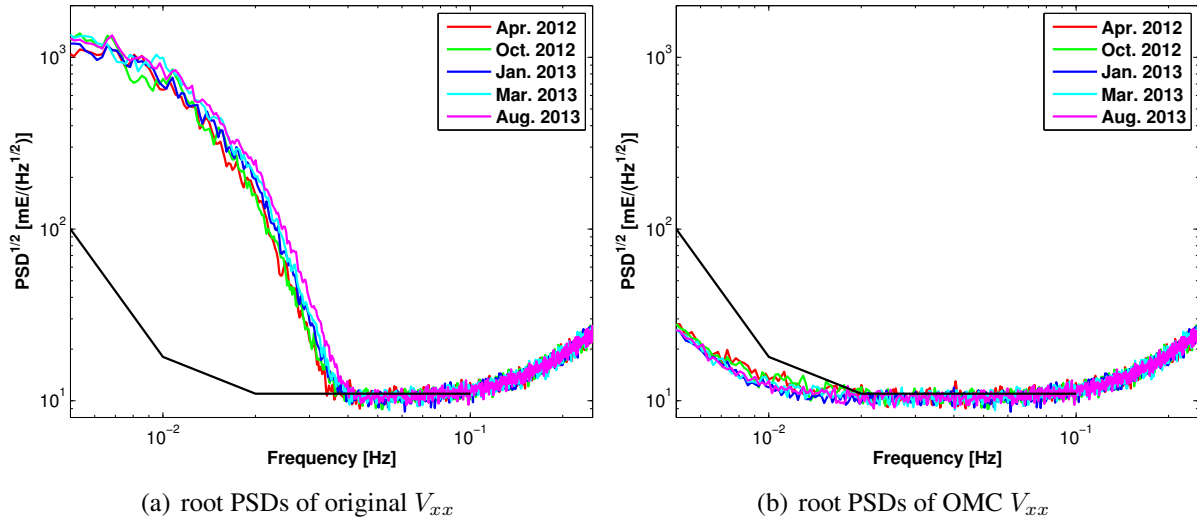


Figure 4.20: Root PSDs of V_{xx} during different time periods

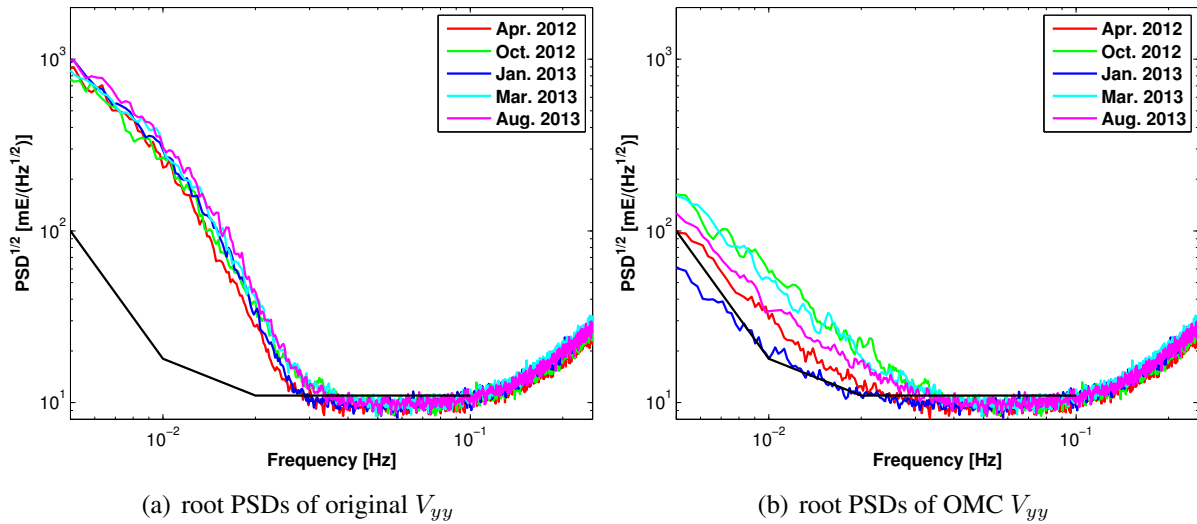


Figure 4.21: Root PSDs of V_{yy} during different time periods

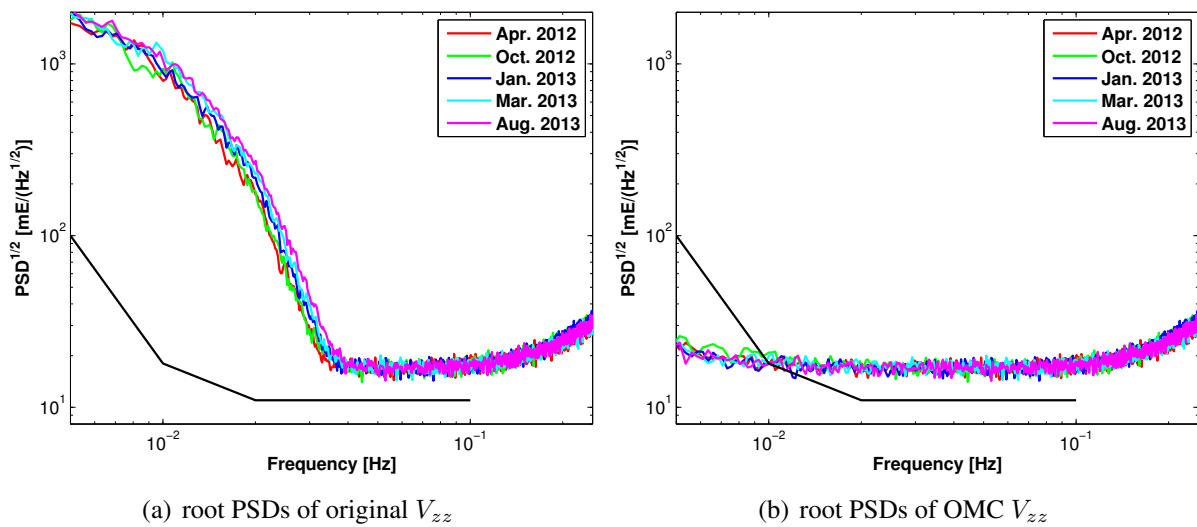


Figure 4.22: Root PSDs of V_{zz} during different time periods

the coefficients estimated from V_{xx} . It shows that the accuracies of the high-degree coefficients (above about d/o 100) are improved with a lower altitude. For the low-degree coefficients, the accuracies remain at the same level. The conclusions are consistent for V_{yy} and V_{zz} , see Figs. 4.24 and 4.25. In summary, lowering the satellite orbit can increase the signal-to-noise ratio of the gravity gradients over the MBW, and thereby improve the accuracy of the high-degree spherical harmonic coefficients.

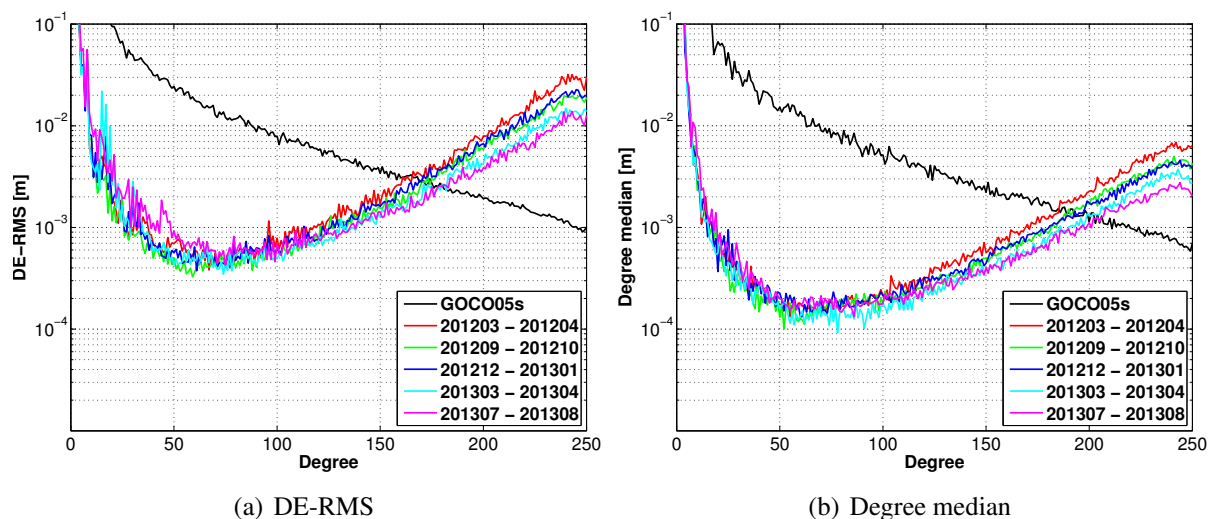


Figure 4.23: Gravity field models recovered from V_{xx} of each group, left: DE-RMS, right: degree median

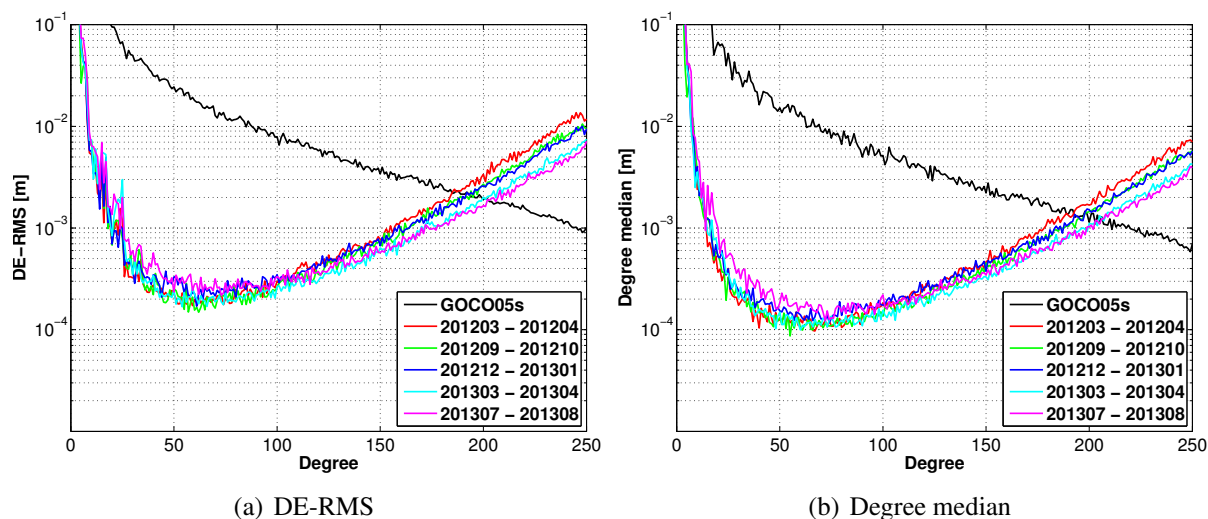


Figure 4.24: Gravity field models recovered from V_{yy} of each group, left: DE-RMS, right: degree median

To sum up all the improvements achieved by lowering the orbit, the spherical harmonic analysis based on all the gravity gradients after the first lowering of the orbit (starting from September 2012 and ending to October 2013) is carried out. In addition, the gravity fields recovered

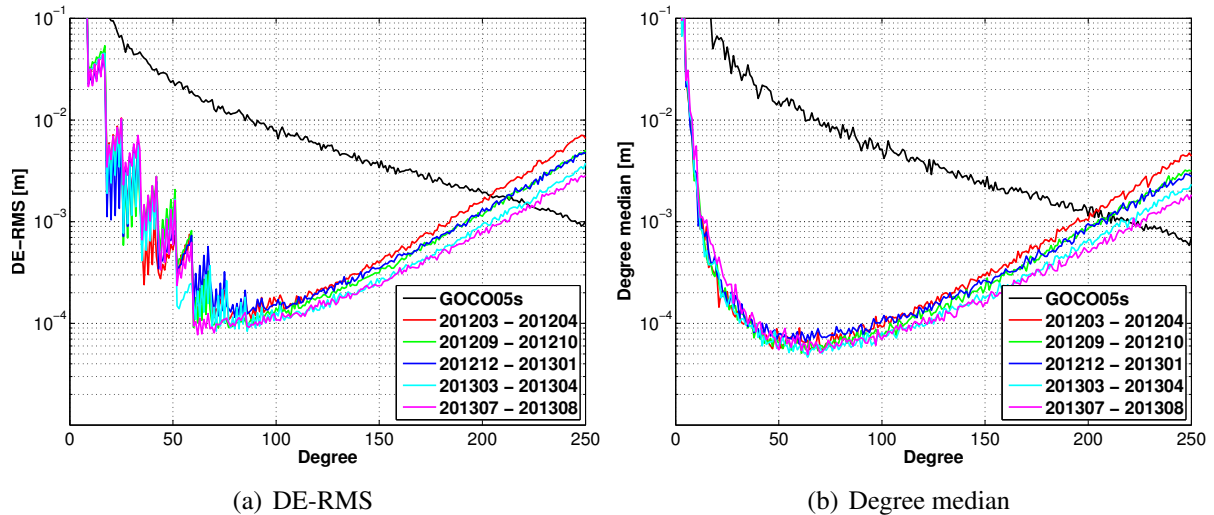


Figure 4.25: Gravity field models recovered from V_{zz} of each group, left: DE-RMS, right: degree median

from the observations of the nominal and the extended operation period (from November 2009 to July 2012) are also given. The comparison of these solutions are shown in Fig. 4.26. It shows that the accuracies of the SH coefficients below d/o 150 are at the same level. But above d/o 150, the accuracy of the SH coefficients derived from the gradients of the lower orbit periods is higher than that from the nominal and extended period. Concerning the data volumes, the gravity gradients from the lower orbit period is about half of that of the nominal and extended period, 14 months vs. 30 months. This demonstrated that the gravity field signal can significantly be improved by lowering the orbit.

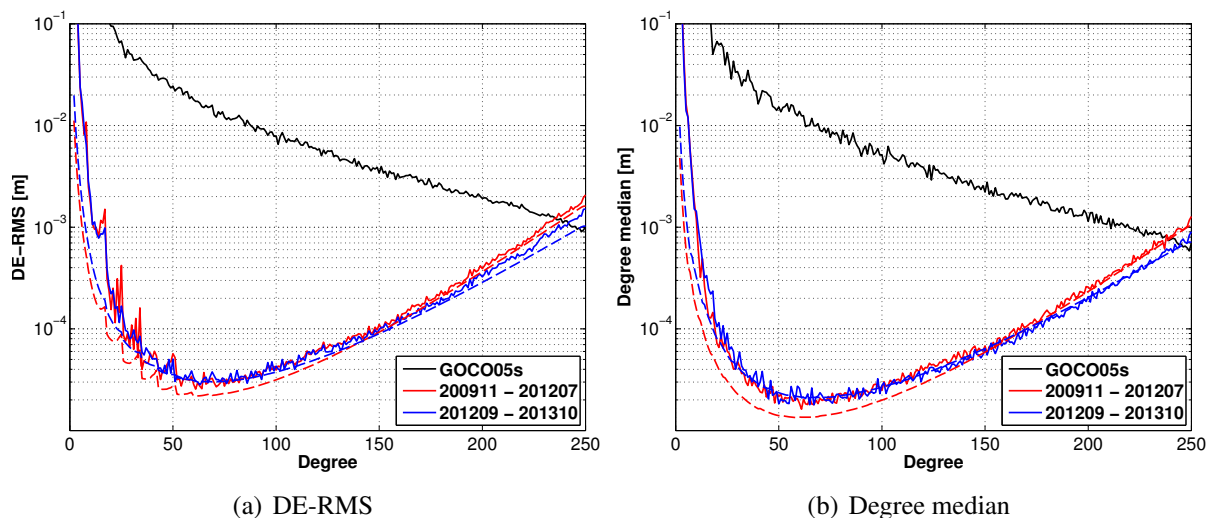


Figure 4.26: Comparison of the gravity field models recovered from the main diagonal gravity gradients of two time periods. One is from November 2009 to July 2012; the other one is from September 2012 to October 2013.

4.6.5 Final models from only gravity gradients

The three main diagonal gravity gradients that are down-sampled to 2 s are finally used for the model determination. Corresponding to the officially published models, there are also five generations of models derived in this dissertation. The first model generation is recovered up to d/o 220 and the other four generations are recovered up to d/o 250. The five generations of models are named as SGG_R1, SGG_R2, SGG_R3, SGG_R4, SGG_R5. The two-dimensional error spectrum of the estimated coefficients is shown in Fig. 4.27, and the one-dimensional error spectrum is shown in Figs 4.28 and 4.29.

The quality of the estimated coefficients is improved from generation to generation. The improvement from SGG_R1 to SGG_R2 is the most distinct, and slight improvements can be noticed for each generation afterwards. Compared with the GOCO05S model, the coefficient differences agree well with the formal errors. This indicates that the formal errors truly reflect the accuracy of the estimated coefficients and can further be used via the error propagation law. Compared with the EGM2008 model, huge differences can be noticed between degree 50 and degree 200. This is because of the well known fact that the EGM2008 model does not have sufficient accuracy in this particular part. Hence, the result demonstrates that the GOCE mission has successfully fulfilled its designed goal by making contributions to the gravity field recovery especially over this part.

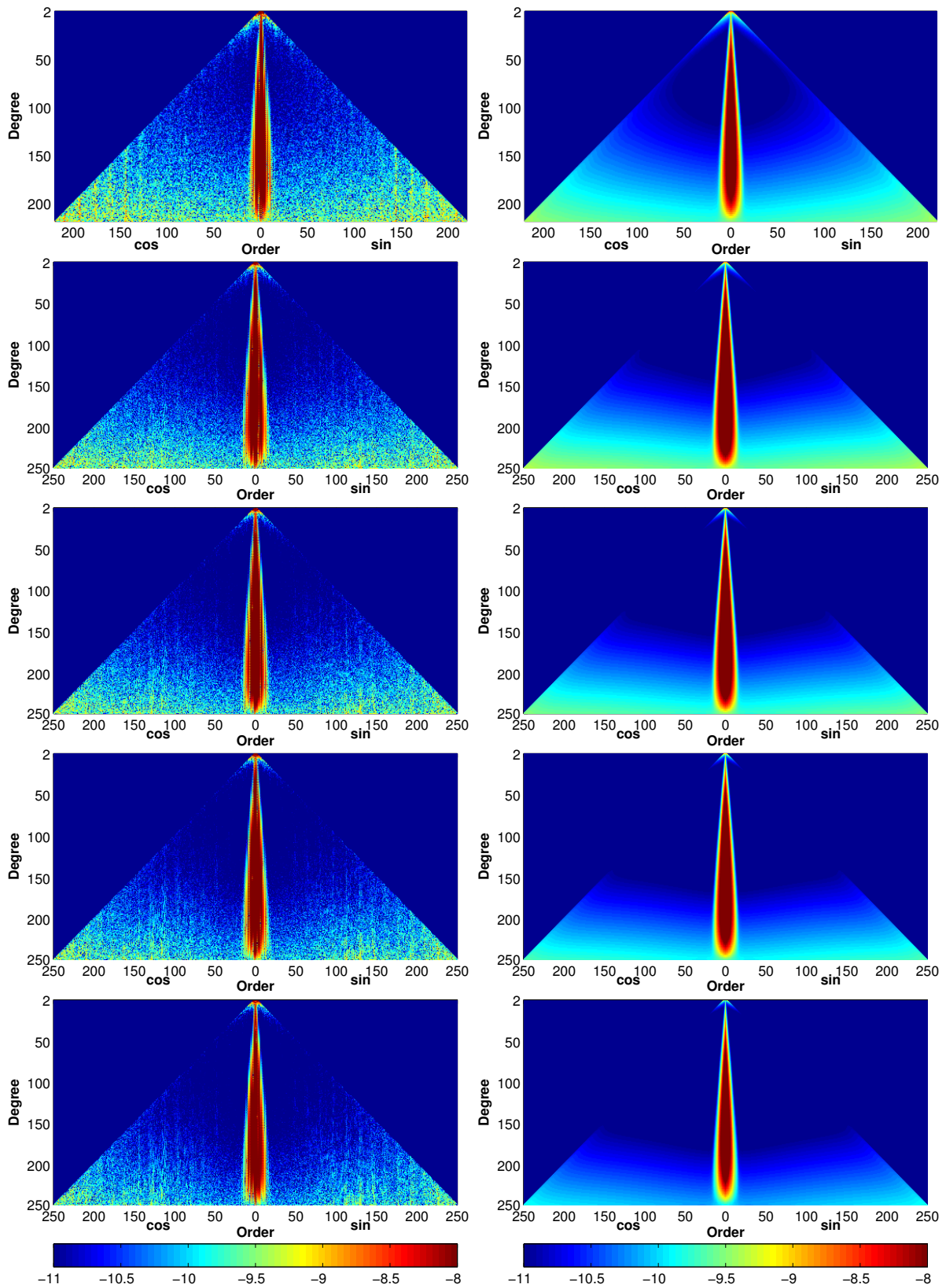


Figure 4.27: Final solutions from the main diagonal gravity gradients, SGG_R1 to SGG_R5 from top to bottom. Coefficient differences w.r.t. GOCO05S (left) and formal errors (right), both are unitless and shown in logarithmic scale.

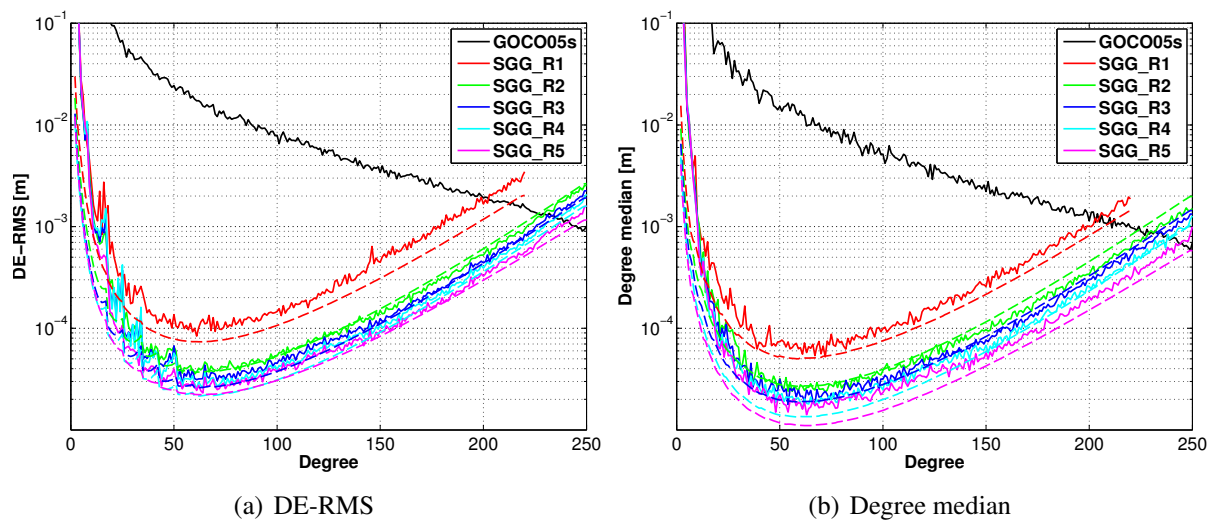


Figure 4.28: Final solutions from the main diagonal gravity gradients, left: DE-RMS, right: degree median. The solid lines represent the coefficient difference w.r.t. GOCO05S while the dashed lines represent formal errors.

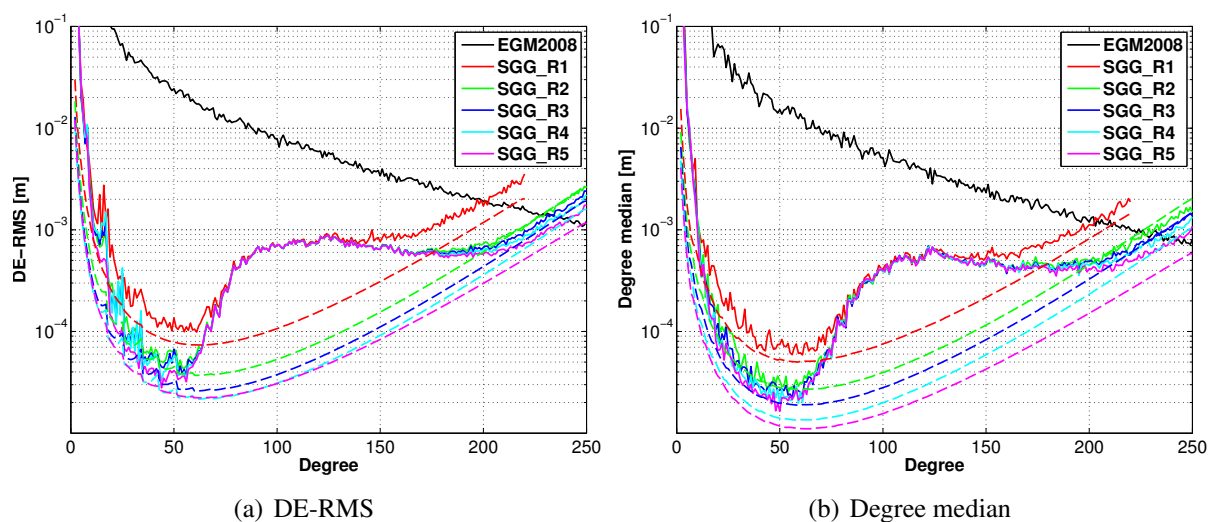


Figure 4.29: Final solutions from the main diagonal gravity gradients, left: DE-RMS, right: degree median. The solid lines represent the coefficient difference w.r.t. EGM2008 while the dashed lines represent formal errors.

Chapter 5

Combined gravity field models using all GOCE observations

In the previous two chapters, a spherical harmonic analysis is performed separately using GOCE orbit data and gravity gradients, and two independent global gravity field models have been derived correspondingly. Because these two types of data are sensitive to different parts of the gravity field signal, their corresponding models have data-oriented restrictions if evaluated alone. However, the two imperfect models are spectrally complementary to each other. To be more specific, the model derived from the orbit data is accurate in the long-wavelength part, while the one derived from the gravity gradients provides the medium- and short-wavelength part. Therefore, a spectral combination of the two parts will provide an advanced model that is accurate over the full wavelength spectrum down to a spatial resolution of about 80 km. In addition to these two complementary parts, a further procedure of regularization is required to cope with the ill-posedness of the problem that is mainly caused by the polar gaps. In this dissertation, the combination of these three data parts is performed with the Variance Component Estimation (VCE) approach, the details of which is explained in Section 5.1. And the final model that is obtained from the combination is presented and evaluated thoroughly in Section 5.2.

5.1 Combined analysis of different data groups

Due to the attenuation of the gravity field signal with the satellite's altitude, the SST-hl technique is only sensitive to the long-wavelength part of the Earth's gravity field. In contrast, the measured gravity gradients are highly accurate only in the Measurement Band Width (MBW) which corresponds to the medium- and short-wavelength parts of the gravity field. Both the SST-hl and SGG techniques are applied in the GOCE mission in order to measure the different parts of the Earth's gravity field. In addition, the zonal and near-zonal coefficients are poorly determined due to the absence of observations in the polar regions. This calls for a procedure of regularization (e.g., Kaula's regularization) to constrain these coefficients. Therefore, the

above-mentioned three data parts have to be combined in order to obtain the final and optimal model of the Earth's gravity field from GOCE data.

The Variance Component Estimation (VCE) approach is applied for the joint analysis of the different data parts. The basis of the VCE approach has been given in Section 2.4. In practice, the normal equation systems for SST-hl, SGG and regularization that are already assembled for the individual analysis are summed up to a complete system by optimal weighting factors, cf. Eq. (2.35). Accounting for the different maximum resolvable spherical harmonic degrees of the SST-hl and SGG observations, the summation of the normal equation systems can not be performed directly. According to the numbering scheme of the parameters, cf. Eq. (4.15), the combination of SST-hl and SGG is performed by adding the corresponding elements on both the left- and right-hand side of the normal equation system. Afterwards, the estimation of the unknown parameters as well as their standard deviations are obtained by direct inversion of the completed normal matrix.

One key point of the VCE approach is the decision on the weight factors which balance the contribution of different data parts to the final solution. In this dissertation, the weight factors for the SST-hl and SGG parts are designed as the inverse of the variance of the unit weight σ_{sst}^2 and σ_{sgg}^2 . Since the a priori values of σ_{sst}^2 and σ_{sgg}^2 are unknown, they are replaced by the posterior variances of $\hat{\sigma}_{sst}^2$ and $\hat{\sigma}_{sgg}^2$. The estimation of $\hat{\sigma}_{sst}^2$ and $\hat{\sigma}_{sgg}^2$ follows Eq. (2.14) or Eq. (2.15). In the real data processing, three acceleration components a_x , a_y and a_z are computed from the SST-hl orbit data, and then used separately for the long-wavelength gravity field recovery. The estimates of their posterior variances are 0.74, 0.74 and 0.80. For the SGG data, the main diagonal gradients V_{xx} , V_{yy} and V_{zz} are used for the gravity field model recovery. The posterior variances of these three components are 0.75, 0.73, 0.75, respectively. In addition, the regularization factor α is determined empirically. For the first regularization group that is used to constrain the polar-gap-related zonal and near-zonal coefficients, a stronger regularization is required because the contribution of the SST-hl and SGG data on this part is quite small. Thus, a large value of $\alpha = 6$ is chosen. For the second regularization group that is used to improve the signal-to-noise ratio in the higher-degree parts, a moderate regularization is applied to only add some smoothness conditions for the high-degree coefficients. The value of $\alpha = 1$ is chosen here.

5.2 Evaluation of the IFE models

With all the above-explained algorithms and techniques, an advanced global gravity field model that is accurate in the full wavelength spectrum up to a certain degree can be derived purely

from the GOCE data. In line with the latest four generations of the official TIM and DIR models, this dissertation also derived four generations of models using GOCE observations with the same timespan as used by the corresponding official models. And as pointed out in the last chapter, the main diagonal gravity gradients are down-sampled to 2 s and used for the final gravity field recovery. These derived models are named after the Institut für Erdmessung (IFE). To be more specific, the four models are named as IFE_R2, IFE_R3, IFE_R4 and IFE_R5.

Our IFE models are resolved up to the spherical harmonic degree of 250. Note that it would be possible to derive the fifth model generation with a higher maximum degree as the observations with better signal-to-noise ratio at the period of a lower orbit are included. But because of the limited computational power, the IFE_R5 has the same truncated degree as its previous versions.

This section deals with the evaluation of our IFE models. The evaluation is performed from three perspectives. First, the four generations of IFE models are compared with each other in the frequency domain (Section 5.2.1). Afterwards, they are compared with the official models in both the frequency (Section 5.2.2) and space (Section 5.2.3) domains.

5.2.1 Internal evaluation of the IFE models

In order to compare the performance of the four releases of IFE models, the error degree variances (i.e., DE-RMS) of the estimated coefficients are firstly computed from the coefficient differences w.r.t. EGM2008. The results are shown in Fig. 5.1. It contains the total error degree variance (all order coefficients are taken into account) and the reduced error degree variance (the zonal and near-zonal coefficients are discarded due to the polar gap). In the high-degree part, i.e., above d/o 170, significant improvements are visible from generation to generation. In the medium-degree part, i.e., between d/o 50 and 170, the errors are similar but with a high level. The reason is attributed to the poor performance of EGM2008 in this frequency part. In the low-degree part, i.e., between d/o 15 and 50, improvements are visible when the zonal and near-zonal coefficients are not taken into account. And in the very low-degree part, i.e., below d/o 15, the performance of the four IFE models are at a comparable level.

Because of the widely-known poor performance of EGM2008 at the medium-frequency part, the latest combined global gravity field model EIGEN-6C4 is then taken as an alternative reference model. The IFE solutions are compared with EIGEN-6C4 and the results are shown in Fig. 5.2. Without considering the zonal and near-zonal coefficients, significant improvements can be noticed in the degrees above d/o 15, except for the coefficients in the frequency band between d/o 100 and 130. One assumption is that the inconsistency could be caused by the EIGEN-6C4 which is determined from a band-limited combination of multiple sources of ob-

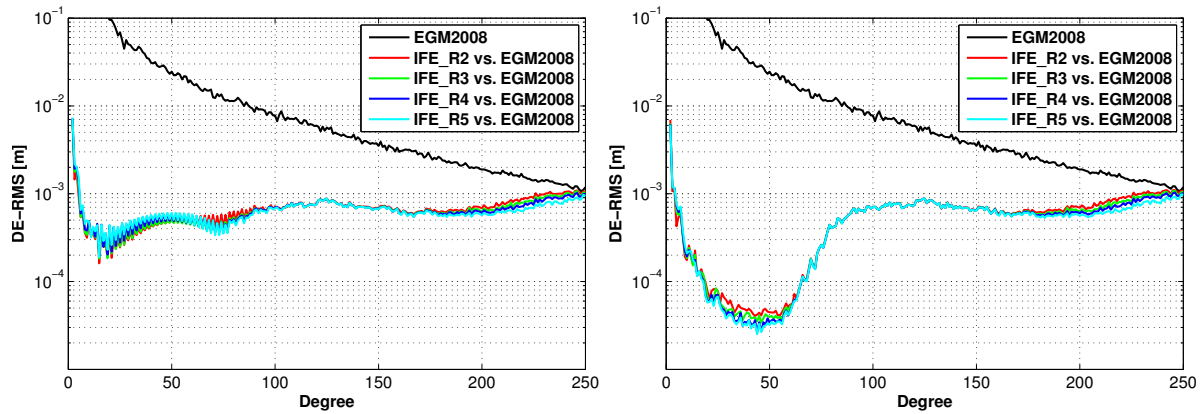


Figure 5.1: Degree-Error RMS of the IFE gravity field solutions w.r.t. EGM2008. Left: all coefficients are considered; right: the zonal and near-zonal coefficients are excluded.

servations, e.g., the satellite and surface data, etc. To prove this assumption, Fig. 5.3 compares the IFE models with GOCO05S which is a combined satellite gravity field model. The consistent improvements are clearly seen above d/o 15. For the very low degree part below d/o 15, the accuracies of the IFE models are at a similar level, which agrees with the comparison w.r.t. EGM2008. This indicates the increasing amount of observations does not improve the accuracy of the very low degree coefficients.

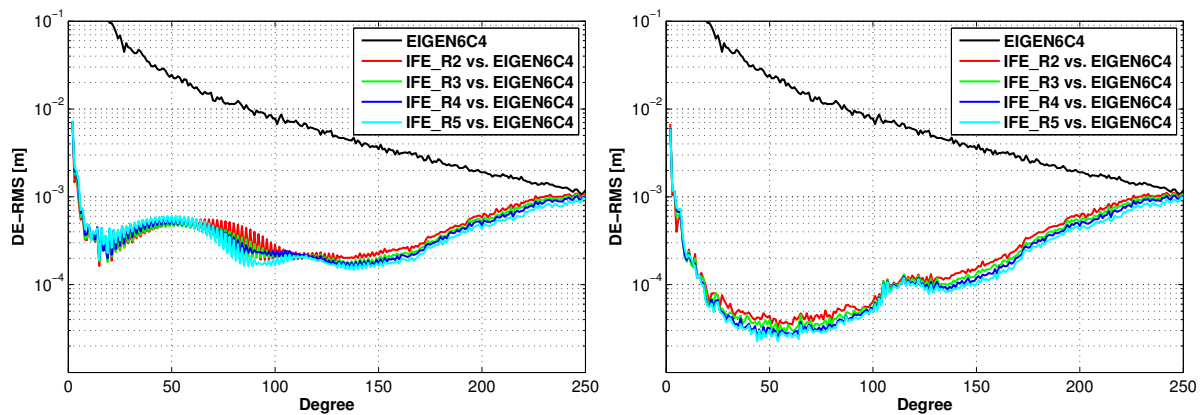


Figure 5.2: Degree-Error RMS of the IFE gravity field solutions w.r.t. EIGEN-6c4. Left: all coefficients are considered; right: the zonal and near-zonal coefficients are excluded.

Taking coefficients of all orders into account, the improvement between d/o 15 and 100 is not visible. This means that the poorly determined zonal and near-zonal coefficients dominate the error of this part. Although regularization has been applied, the constraint on the coefficients of this frequency part is still not optimal. An advanced regularization strategy is required in future work.

Furthermore, the cumulative geoid height errors of the IFE solutions w.r.t. the EIGEN-6C4 and GOCO05S are computed. As discussed above, the zonal and near-zonal coefficients are not

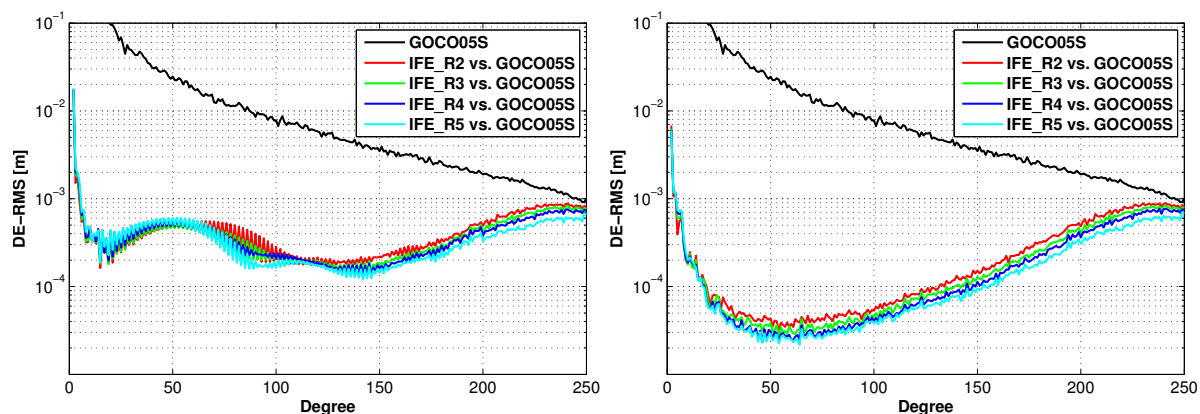


Figure 5.3: Degree-Error RMS of the IFE gravity field solutions w.r.t. GOCO05s. Left: all coefficients are considered; right: the zonal and near-zonal coefficients are excluded.

determined in a comparable accuracy with the coefficients of other parts, they are discarded in the computation of the cumulative geoid errors. The comparison of the results is shown in Fig. 5.4. Up to d/o 200 (corresponding to a spatial resolution of 100 km), the cumulative geoid height errors of the IFE solutions w.r.t. EIGEN-6C4 are 3.99, 3.65, 3.43 and 3.25 cm, for the second to fifth generation; similarly, the errors w.r.t. GOCO05s are 3.62, 3.23, 2.98 and 2.75 cm. Up to d/o 250 (corresponding to a spatial resolution of 80 km), the cumulative geoid height errors of the IFE solutions w.r.t. EIGEN-6C4 are 8.52, 7.83, 7.35 and 6.75 cm while the errors w.r.t. GOCO05s are 7.43, 6.66, 6.08 and 5.31 cm. The comparison with EIGEN-6C4 and GOCO05s indicates that the performance of IFE solutions are closer to the satellite combined solution GOCO05s. And the geoid height error of IFE_R5 is 2.75 cm which is slightly higher than the GOCE designed goal with a 1-2 cm geoid accuracy at the spatial resolution of 100 km.

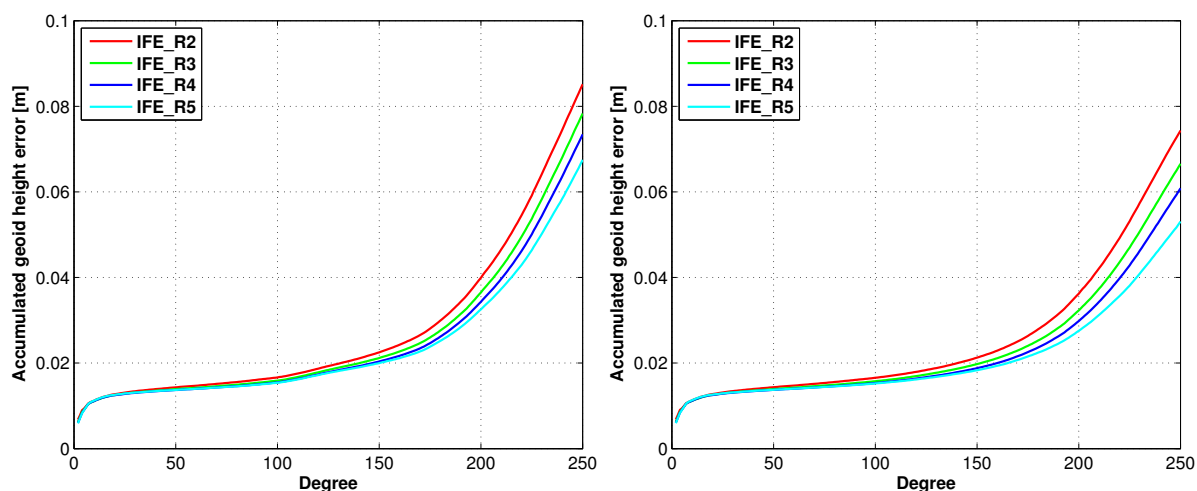


Figure 5.4: Cumulative geoid errors of the IFE gravity field solutions w.r.t. EIGEN-6C4 (left) and GOCO05S (right). The zonal and near-zonal coefficients are excluded to calculate the cumulative geoid errors.

In addition, the errors of the very low-degree coefficients are significant, especially at degree 2, which are easily found in both the comparison with EIGEN-6C4 and GOCO05s. The cumulative geoid height errors of the IFE solutions without considering the errors of the very low-degree coefficients, i.e., d/o 2 to 4, are recomputed and shown in Fig. 5.5. The cumulative geoid height error of IFE_R5 up to d/o 200 is now reduced to 2.43 cm and 1.92 cm, with respect to EIGEN-6C4 and GOCO05s, respectively. The reason for the poor performance of the very low-degree coefficients is that the SST-hl technique is not sensitive enough to this frequency part. The observations from Laser Geodynamics Satellite (LAGEOS) are thus usually combined with the other data to improve the accuracy of the coefficients in the very low-degree part. The LAGEOS satellite is operated in a much higher altitude, i.e., 5900 km, so that it is only sensitive to the very long-wavelength part of the Earth's gravity field. Moreover, the applied acceleration approach may be responsible for the large error of the degree-2 coefficients. The double-difference operation of the satellite orbit may cause a decrease of the signal-to-noise ratio at the very low-frequency part.

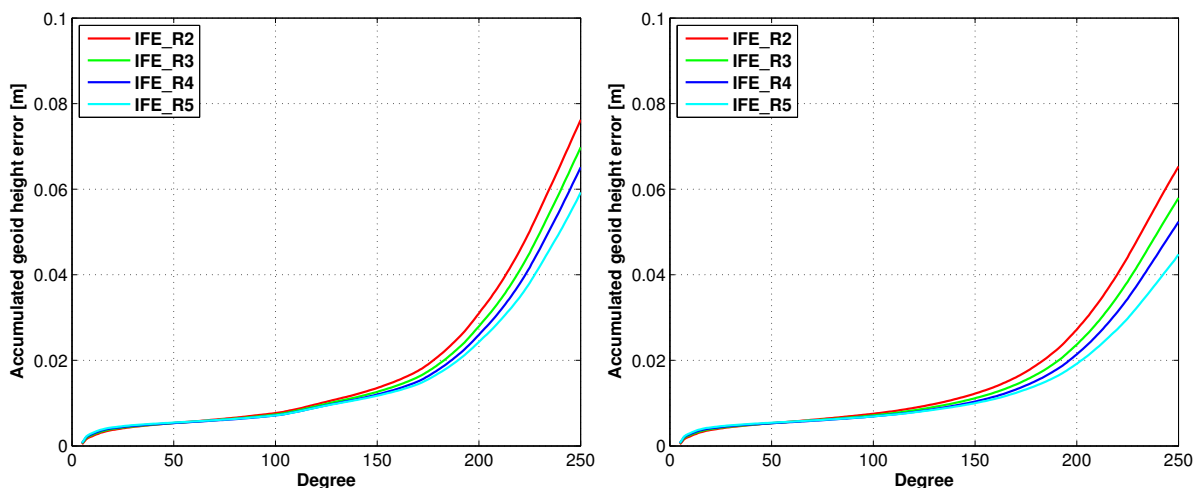


Figure 5.5: Cumulative geoid errors of the IFE gravity field solutions w.r.t. EIGEN-6C4 (left) and GOCO05S (right). The zonal and near-zonal coefficients as well as the low degree (d/o 2 to 4) coefficients are excluded to calculate the cumulative geoid errors.

5.2.2 External evaluation of the IFE models in the frequency domain

A number of global gravity field models have been derived from the GOCE observations and published during the past years. Among them, the official releases of the TIM, DIR and SPW series are produced by the GOCE High Performance Facility (HFP). TIM and DIR contain five generations of models while SPW contains three generations. Additionally, several GOCE related models have also been published by other research groups. These include, for example, the ITG-Goce02s derived by the Bonn group, JYY_GOCE solutions computed by Yi (Yi, 2012b), etc. Tab. 5.1 lists some details of these published models, including the type of the

data set being used, the timespan of the data set, the sampling interval of the data as well as the maximum resolved degree and order. To achieve rational and objective evaluation results for our IFE models, the external comparisons that is carried out in the following will be based on models with similar timespan.

Table 5.1: Details of the published GOCE gravity field models and the IFE solutions

model name	data set	timespan	interval [s]	d/o
TIM_R1	PKI, V_{xx} , V_{yy} , V_{zz}	11/2009 - 01/2010	1	224
TIM_R2	PKI, V_{xx} , V_{yy} , V_{zz}	11/2009 - 07/2010	1	250
TIM_R3	PKI, V_{xx} , V_{yy} , V_{zz} , V_{xz}	11/2009 - 04/2011	1	250
TIM_R4	PKI, V_{xx} , V_{yy} , V_{zz} , V_{xz}	11/2009 - 06/2012	1	250
TIM_R5	PKI, V_{xx} , V_{yy} , V_{zz} , V_{xz}	11/2009 - 10/2013	1	280
DIR_R1	PRD, V_{xx} , V_{yy} , V_{zz}	11/2009 - 01/2010	1	240
DIR_R2	PKI, V_{xx} , V_{yy} , V_{zz}	11/2009 - 06/2010	1	240
DIR_R3	PKI, V_{xx} , V_{yy} , V_{zz}	11/2009 - 04/2011	1	240
DIR_R4	PKI, V_{xx} , V_{yy} , V_{zz} , V_{xz}	11/2009 - 07/2012	1	260
DIR_R5	PKI, V_{xx} , V_{yy} , V_{zz} , V_{xz}	11/2009 - 10/2013	1	300
SPW_R1	PKI, V_{xx} , V_{yy} , V_{zz} , V_{xz}	11/2009 - 01/2010	1	210
SPW_R2	PKI, V_{xx} , V_{yy} , V_{zz} , V_{xz}	11/2009 - 07/2010	1	240
SPW_R4	PKI, V_{xx} , V_{yy} , V_{zz} , V_{xz}	11/2009 - 07/2012	1	280
ITG_Goce02s	PKI, V_{xx} , V_{yy} , V_{zz}	11/2009 - 06/2010	5	240
JYY_GOCE02S	PKI, V_{xx} , V_{yy} , V_{zz} , V_{xz}	11/2009 - 08/2012	1	230
JYY_GOCE04S	PKI, V_{xx} , V_{yy} , V_{zz} , V_{xz}	11/2009 - 10/2013	1	230
IFE_R2	PKI, V_{xx} , V_{yy} , V_{zz}	11/2009 - 06/2010	2	250
IFE_R3	PKI, V_{xx} , V_{yy} , V_{zz}	11/2009 - 04/2011	2	250
IFE_R4	PKI, V_{xx} , V_{yy} , V_{zz}	11/2009 - 06/2012	2	250
IFE_R5	PKI, V_{xx} , V_{yy} , V_{zz}	11/2009 - 10/2013	2	250

First, the models derived from GOCE observations during a period of 8 months from November 2009 to June 2010 are compared. The same data set was used to derive the second generation of GOCE official models. Fig. 5.6 shows the comparison of these models with respect to the GOCO05s. Above d/o 50, the performance of IFE_R2 is the best while SPW_R2 is the worst, see the DE-RMS plot in Fig. 5.6. The performance of other models, i.e, TIM_R2, DIR_R2 and ITG_goce02s, is between IFE_R2 and SPW_R2. The SPW solution is solved by numerical integration of the spherical gridded values which are interpolated from the local patches of data. The interpolation can be seen as low-pass filter which causes a loss of the high-frequency information. This is the reason why the SPW solution is the worst above d/o 50. Although the number of observations to derive the IFE_R2 solution is only half of that is used to derive the other two GOCE official models, its accuracy is still higher than them. There are two main reasons for this: 1) reprocessed gravity gradients which have better quality (Pail et al., 2013) are

used to derive the IFE model; 2) a more accurate stochastic model is used in the determination of IFE_R2, i.e., the empirical VCMs are constructed from the more accurate residuals which are computed based on the whole period of GOCE observations, cf. Section 4.6.1. ITG_GoCe02s is also determined from the reprocessed gravity gradients but with a large sampling interval of 5 s. Due to the smaller number of observations, the accuracy of ITG_GoCe02s is poorer than IFE_R2. And the quality of the VCM also affects the accuracy of ITG_GoCe02s. Between d/o 15 and 50, ITG_GoCe02s and IFE_R2 perform better than TIM_R2 and SPW_R2. The contribution to this frequency part is mainly from the SST-hl observations. The acceleration approach and the short-arc approach are applied to process the SST-hl observations in IFE_R2 and ITG_goCe02s. The results of these two approaches are known to be better than that from the energy balance approach which is used in the TIM and SPW solutions. DIR_R2 is most accurate below d/o 30 since a priori gravity field information of ITG-Grace2010s is introduced. In the very low-degree part (between d/o 2 and 4), the error of the IFE solution is the largest. This is because the acceleration approach is less sensitive to the very long-wavelength gravity field signal. Moreover, the cumulative geoid errors of these models are also compared. As discussed above, the zonal and near-zonal as well as the very low-degree coefficients (below d/o 4) are not taken into account to calculate the cumulative geoid error. Up to d/o 200, the error of IFE_R2 is 2.72 cm, smaller than 3.81, 3.73, 4.79, 3.27 cm for the TIM, DIR, SPW solutions and ITG-GoCe02s.

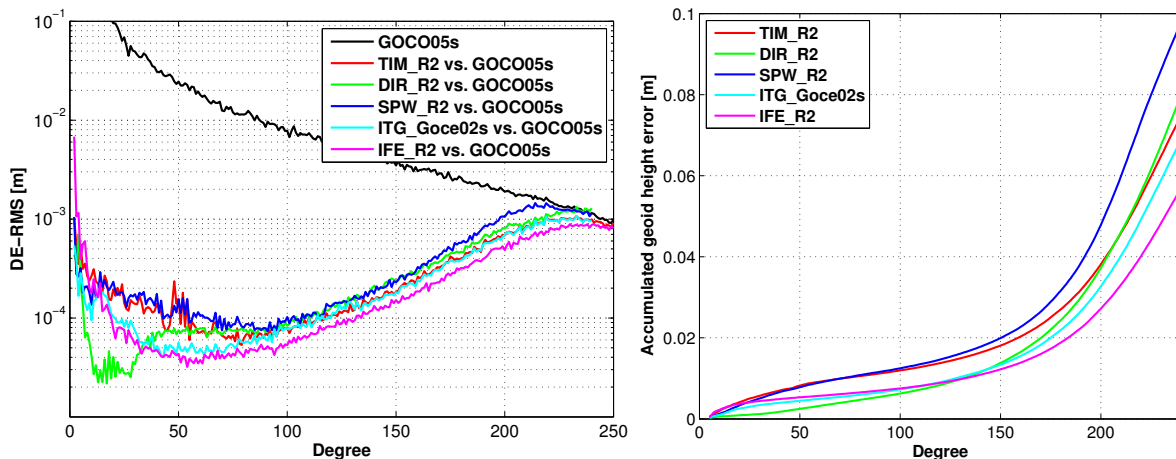


Figure 5.6: Comparison of the second generation of GOCE models w.r.t. GOCO05s. Left: Degree-Error RMS; right: cumulative geoid error. The zonal and near-zonal coefficients are not taken into account, and the cumulative geoid errors are computed starting from d/o 5.

The comparison of the third generation GOCE models that are determined from the observations between November 2009 and April 2011 is shown in Fig. 5.7. IFE_R3 is slightly more accurate than TIM_R3 above about d/o 80. On the one hand, the number of observations to derive TIM_R3 is about twice of IFE_R3, because the gravity gradients are down-sampled to 2 s when they are used to derive the IFE solutions. In addition, the gradient V_{xz} is not used in the

determination of IFE_R3 but used in TIM solution. On the other hand, the reprocessed gravity gradients with a higher accuracy are used to derive the IFE models. And also, more accurate VCMs are applied in the IFE solution. Both effects are almost counteracting each other. Below d/o 80, the IFE solution performs much better than TIM since the energy balance approach is replaced by the acceleration approach. As for the DIR solution, it is slightly worse than TIM above d/o 150 as the contribution of V_{xz} is not taken into account. Below d/o 150, especially below d/o 80, it is better than the other two solutions as GRACE information and the satellite laser ranging (SLR) data of LAGEOS are combined with GOCE. Besides, the DIR solution is not consistent around d/o 150. The cumulative geoid errors up to d/o 200 are 2.79, 2.71 and 2.37 cm for TIM_R3, DIR_R3 and IFE_R3, respectively.

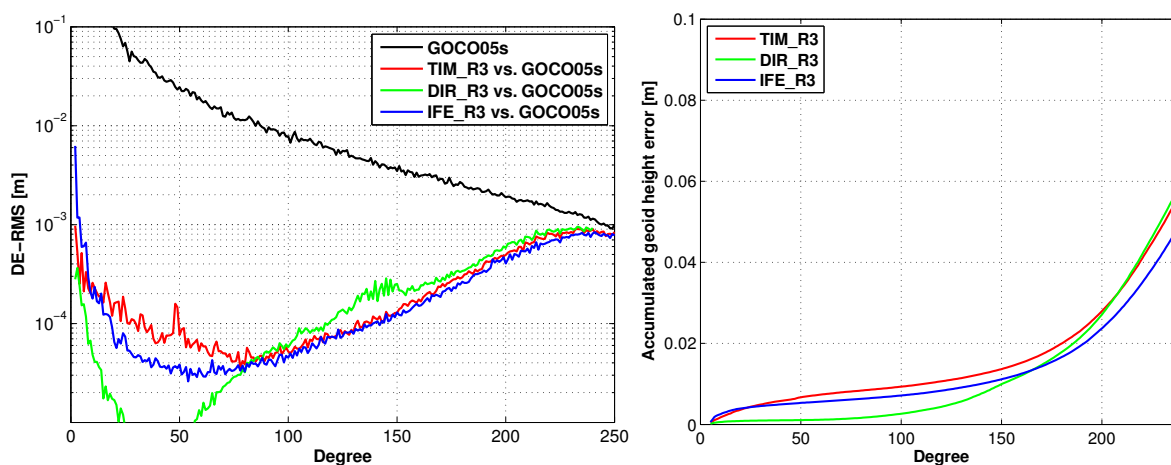


Figure 5.7: Comparison of the third generation of GOCE models w.r.t. GOCO05s. Left: Degree-Error RMS; right: cumulative geoid error. The zonal and near-zonal coefficients are not taken into account, and the cumulative geoid errors are computed starting from d/o 5.

The comparison of the fourth generation GOCE models that are determined from the observations between November 2009 and June 2012 is shown in Fig. 5.8. From this generation on, all the models are determined from the reprocessed gravity gradients. Fig. 5.8 shows that TIM_R4 performs best in the whole spectrum among the fourth generation models. The short-arc approach is alternatively applied to process the SST-hl data, which significantly increases the accuracy of the low-degree coefficients. Additionally, the increasing amount of the observations (about two times of the third generations) and the reprocessed high-quality gravity gradients significantly improve the performance of the model in the high-degree part. In addition, the increased amount of observations also leads to more accurate VCMs which adds positive effects to improve the models. Similar as the third generation, the low-degree part of DIR_R4 is not purely from GOCE SST-hl data but combined with GRACE and LAGEOS observations. With an advanced gridding algorithm used, the SPW solution is improved compared to its previous versions. But it is still worse than the TIM solution. *jyy_goce02s* is derived from an alternative strategy to process the GOCE gradients where a bandpass filter is applied to cope with the

coloured noise (Yi, 2012a). The performance of `jyy_goce02s` is similar to the SPW solution. As for `IFE_R4`, it is slightly worse than the other models in the high-degree part (above d/o 80). The reason is mainly attributed to the smallest amount of the gravity gradients used (due to the down-sampling of main diagonal gradients and the neglect of V_{xz}). Up to d/o 200, the geoid height errors of `TIM_R4` and `DIR_R4` are 1.33 and 1.29 cm, respectively, followed by 1.79 and 1.80 cm for `SPW_R4` and `jyy_goce02s`, and 2.14 cm for `IFE_R4`.

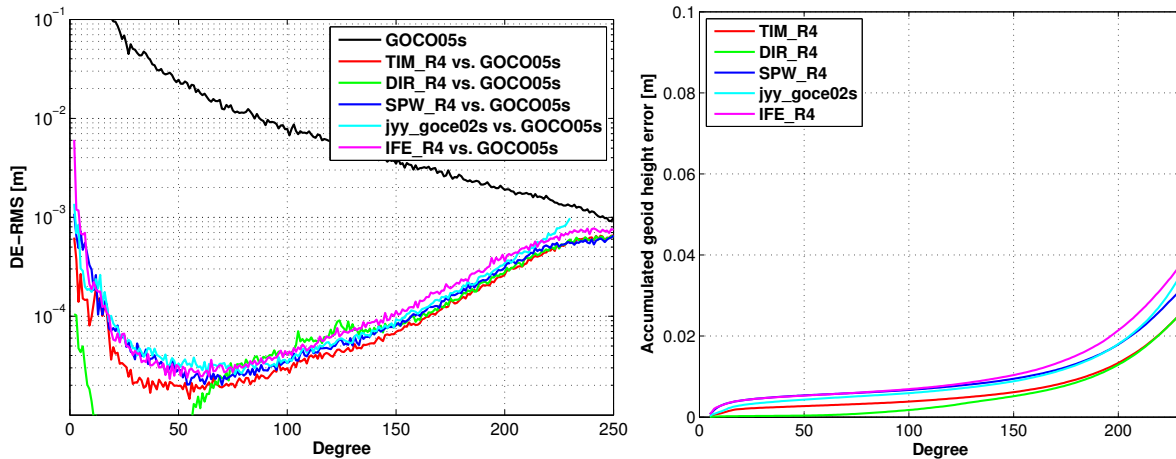


Figure 5.8: Comparison of the fourth generation of GOCE models w.r.t. GOCO05s. Left: Degree-Error RMS; right: cumulative geoid error. The zonal and near-zonal coefficients are not taken into account, and the cumulative geoid errors are computed starting from d/o 5.

The comparison of the fifth generation of GOCE models are shown in Fig. 5.9. The observations during the entire period from November 2009 to October 2013 are used to derive the fifth generation models. Different to the previous TIM solutions, the error behaviour of `TIM_R5` is not consistent in the whole spectrum. After a sharp decrease, the errors above d/o 200 become much smaller which indicates that the signal of `TIM_R5` is quite close to `GOCO05s`. This is because the same gradiometer observations are also used in the determination of `GOCO05s`. The contribution of both models above d/o 200 are mainly from the GOCE gradients. Between d/o 150 and 200, the signal of `GOCO05s` is determined from the combination of GRACE and GOCE gradients. The contribution of the gradients is dominant in this part, but the contribution from GRACE is also visible. The `DIR` solution still performs best in the low-degree part since information of GRACE and LAGEOS is introduced. The inconsistency of the `DIR` solution around d/o 120 still exists due to the applied band-limited filter. With the same amount of GOCE observations used, `jyy_goce04s` performs worse than `TIM_R5` and `DIR_R5`. The `IFE` solution is worse than the other models above d/o 80 due to the loss of observations (caused by down-sampling of main diagonal gradients and the neglect of V_{xz}). The cumulative geoid errors up to d/o 200 are 0.60 and 0.95 cm for `TIM_R5`, `DIR_R5`, followed by 1.34 and 1.92 cm for `jyy_goce04s` and `IFE_R5`.

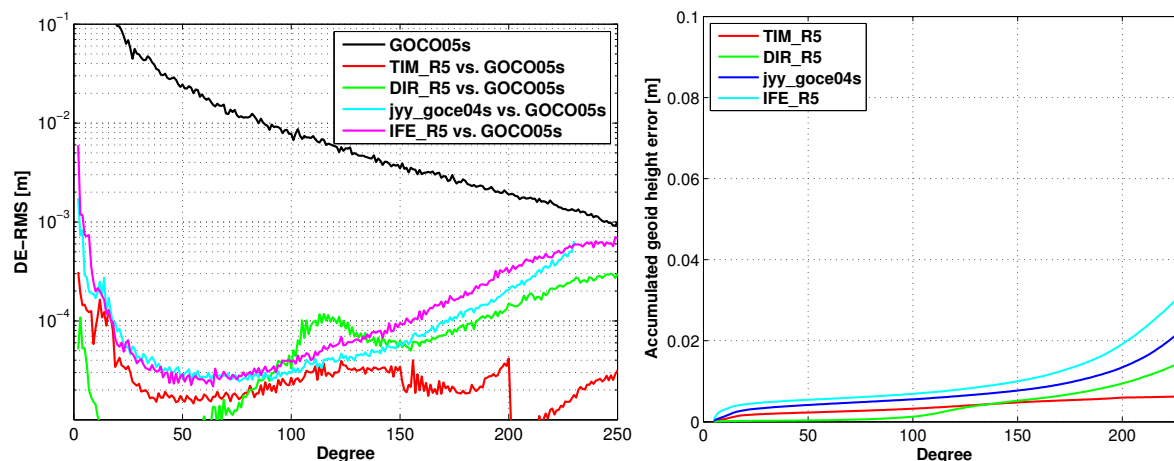


Figure 5.9: Comparison of the fifth generation of GOCE models w.r.t. GOCO05s. Left: Degree-Error RMS; right: cumulative geoid error. The zonal and near-zonal coefficients are not taken into account, and the cumulative geoid errors are computed starting from d/o 5.

5.2.3 External evaluation of the IFE models in the space domain

In addition to the frequency domain analysis, the error behaviour of the model coefficients in the spatial domain is analysed in this subsection. The error behaviour is presented geographically in terms of geoid height differences and gravity anomaly differences which are calculated from the coefficient differences by a Spherical Harmonic Synthesis. Here, the combined model EGM2008 is taken as the reference model. Figs. 5.10 and 5.11 show the comparison of the TIM and IFE solutions, with the geoid height differences and the gravity anomaly differences computed from the coefficients up to d/o 250 corresponding to a spatial resolution of 80 km.

A distinct feature of the error behaviour shown in Fig. 5.10 is that large geoid height differences are clearly visible in South America, Africa and Himalaya, etc. This is attributed to the large errors of EGM2008 in these regions since no or only erroneous terrestrial data are used in the determination of EGM2008. In the other regions where high accurate terrestrial or satellite observations are available, the performance of EGM2008 is considered as the best. Then geoid height differences are relatively small, and are dominated by the errors of the GOCE solutions. With the improvements of newer releases of the GOCE models, the errors are then reduced. The comparison of the TIM and IFE solutions in the spatial domain coincides with the frequency-domain analysis. Generally, the second and third generation of IFE solutions are superior due to the more accurate VCMs applied; while the four and fifth generation of TIM solutions perform better than the IFE solutions because more observations are used for their determination. Moreover, Fig. 5.11 shows the errors in terms of gravity field anomalies. Similarly, large errors are visible over the continents where it is lack of accurate gravimetric observations. In the other parts, the errors dominated by the GOCE models are reduced from

generation to generation.

The standard deviations of the geoid height differences and the gravity anomaly differences in the region between latitude -80° to 80° (the polar gaps are excluded) are shown in Tab. 5.2. The standard deviations of the IFE_R2 and IFE_R3 models in terms of geoid height difference are 17.0 cm and 16.1 cm, respectively, which are smaller than 18.3 cm and 16.8 cm of the corresponding TIM solutions. For the fourth and fifth generation models, the standard deviations of the TIM solutions decrease to 14.8 cm and 13.1 cm, while the IFE solutions are reduced to 15.6 cm and 14.9 cm. In terms of gravity anomaly differences, the standard deviations of the IFE solutions are 5.19 mGal, 4.88 mGal, 4.67 mGal and 4.39 mGal from the second to fifth generation. Correspondingly, the values for the TIM solutions are 5.68 mGal, 5.14 mGal, 4.40 mGal, 3.67 mGal. For the DIR models, the standard deviations are close to those of the TIM solutions.

Table 5.2: Comparison of the TIM, DIR and IFE solutions. The standard deviations of the geoid height differences and gravity anomaly differences w.r.t. EGM2008 are calculated. The models are truncated at d/o 250.

(a) geoid height differences (cm)				(b) gravity anomaly differences (mGal)			
release	TIM	DIR	IFE	release	TIM	DIR	IFE
R2	18.3	18.7	17.0	R2	5.68	5.71	5.19
R3	16.8	16.0	16.1	R3	5.14	4.70	4.88
R4	14.8	14.5	15.6	R4	4.40	4.25	4.67
R5	13.1	13.0	14.9	R5	3.67	3.63	4.39

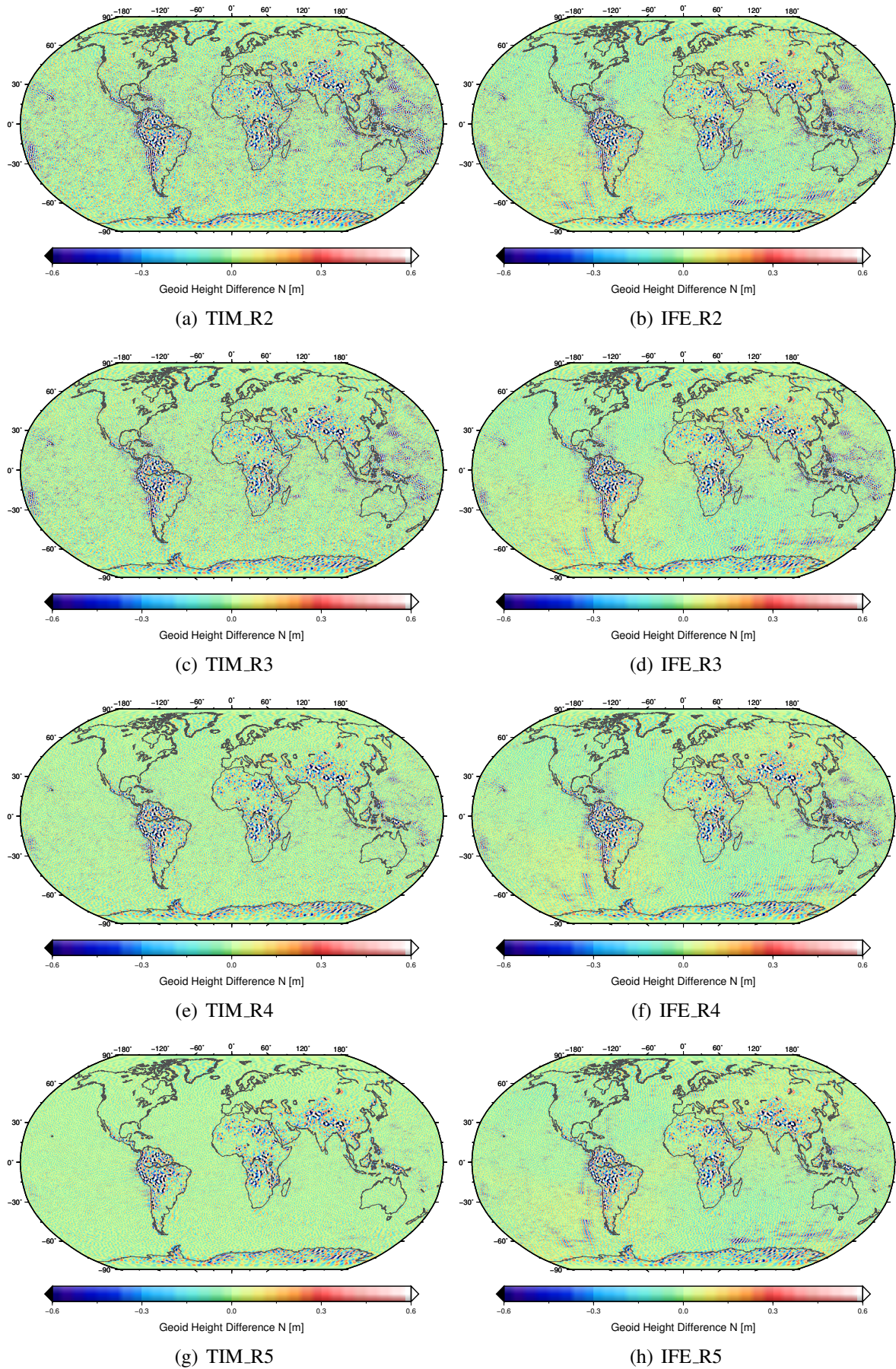


Figure 5.10: Differences of the TIM and IFE solutions to EGM2008 in terms of geoid heights

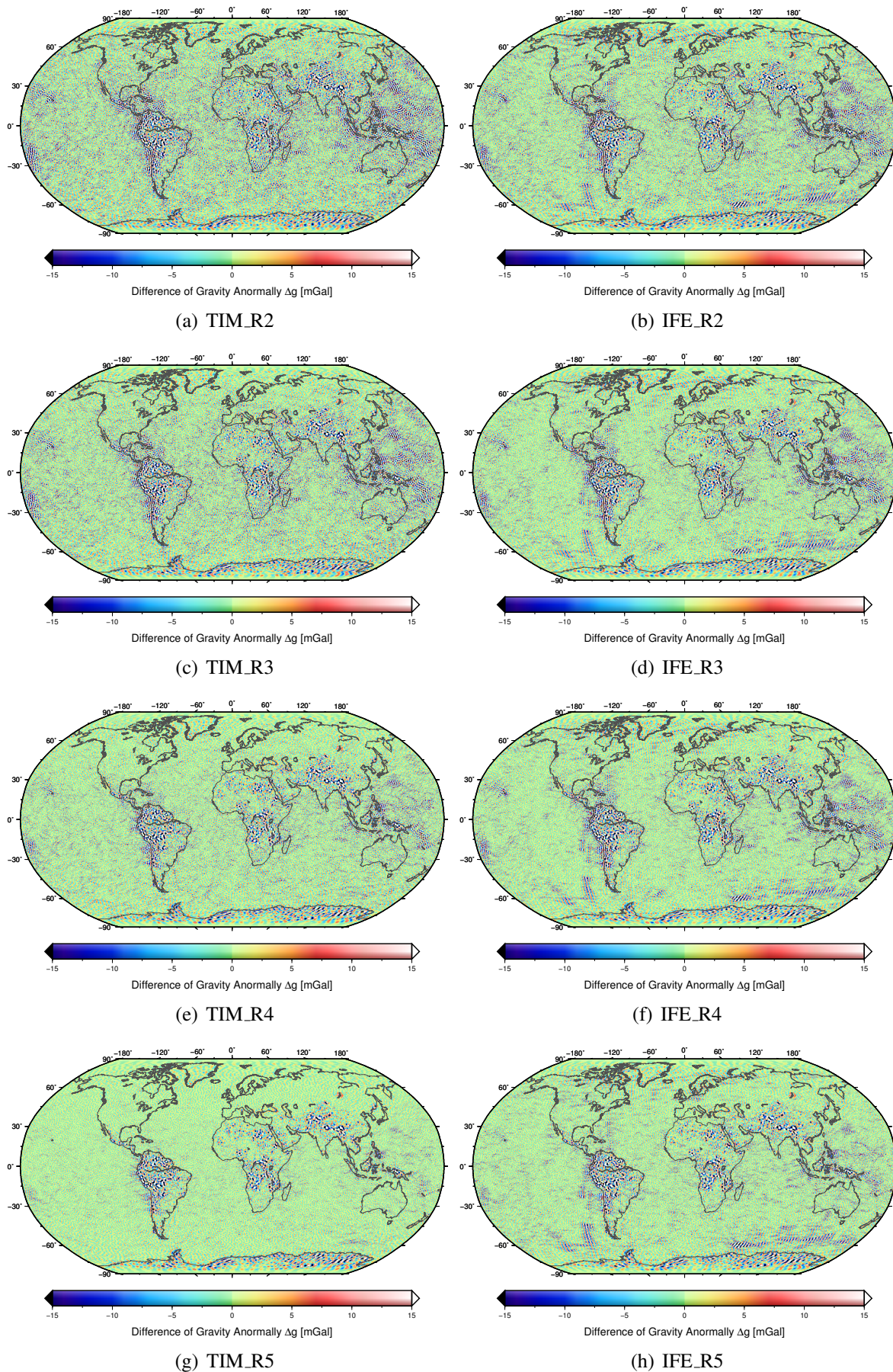


Figure 5.11: Differences of the TIM and IFE solutions to EGM2008 in terms of gravity field anomalies

Chapter 6

Conclusions and outlook

6.1 Conclusions

An adequate knowledge of the Earth's gravity field is essential for many Earth sciences and practical applications. This dissertation expands such knowledge by providing an accurate global gravity field model from GOCE observations. Being the first to implement both SST-hl and SGG techniques, the GOCE mission has delivered hundreds of millions of observations to enable the recovery of a Earth's gravity field model. In this dissertation, the kinematic orbit is used to determine the long-wavelength part of the gravity field, while the gravity gradients are employed for the medium- and short-wavelength parts. The two types of observations are analysed both separately for determining two complementary models and jointly for the final gravity field models.

The acceleration approach is employed for the individual analysis of the GOCE SST-hl data. Within this approach, the satellite's accelerations and the representation of the Earth's gravity field model are transformed and balanced in the same frame, i.e., Inertial Reference Frame. The over-determined linear equation system is solved by the classic LS technique. The assembly of the normal matrix is performed arc-wisely, which facilitates parallel computation. In each arc, one empirical parameter is added to absorb systematic errors in the observations, which implicitly assumes having the same systematic errors for all observations of one arc. In addition, the empirical Variance/Covariance Matrix of the observations is constructed in each arc. Hence, the length of the arc becomes crucial for the quality of the recovered model. If the length is too short, the empirical parameters would absorb not only the systematic errors but also the very long-wavelength gravity field signal. If the length is too large, the systematic errors can not be fully absorbed. In this dissertation, the arc length is chosen as 35 minutes by trial and error.

In addition to the length of the arc, another key setting in the analysis of SST-hl observations is the sampling rate. The GOCE sensors collect observations at a sampling rate of 1 s, which corresponds to gravity field features up to d/o 2700. Since the SST-hl technique is only sensitive to the long-wavelength gravity field, the 1 s kinematic orbit is over-sampled. In addition, the

high-frequency content can be amplified during the computation of accelerations, which affects the extraction of the long-wavelength gravity field signal. Therefore, the original observations are down-sampled to a rate of 30 s. But this causes a loss of the observations. To avoid it, an extended down-sampling algorithm is applied.

The gravity field is solved up to d/o 150, where the signal-to-noise ratio is close to one. Compared with the most accurate long-wavelength gravity field model ITG-Grace2010s, the geoid height errors is 7.76 cm when the zonal and near-zonal coefficients (degraded by the polar gaps) are not considered. In addition, the degree-2 coefficients are not well determined. This implies that the acceleration approach is not sensitive enough to such very low-degree coefficients.

The gravity gradients are processed in the Gradiometer Reference Frame to avoid possible transformation errors, since the transformation of the gradients might degrade the four accurate gradient components by two other less accurate components. The gradients are firstly screened by removing the abnormal observations and the outliers. The remaining observations are used for the estimation of the spherical harmonic coefficients up to d/o 250. This is a challenging task in terms of computational time and memory, which could not be solved without a parallel computer. In this research, the computation is carried out on the cluster system of Leibniz Universität IT Services. To save computational time, the computation is performed in parallel based on the very efficient library MKL. Concerning the memory space, a new storage format, i.e., RFP, which saves the upper triangular part of the normal matrix by a rectangular packet format, is employed.

Similar as the kinematic orbit, the gravity gradients also suffer from systematic errors and coloured noise. The systematic errors are expected to be absorbed by empirical parameters that contain a bias and drift term. The coloured noise is handled by applying the empirical VCMs that are constructed from the initial residuals. The empirical parameters are added and the VCMs are constructed in each arc. The length of the arc is chosen as 15 minutes. In addition, the original 1 s data is down-sampled to 2 s in order to reduce the computational burden. Five models are derived from different amounts of observations (2 months, 8 months, 16 months, 32 months and 46 months). The results shows that these models show a high performance in the aimed spectral band (between d/o 50 and 250), and increasing the amount of the observations improves the quality of the models.

This dissertation further explores the effect of the orbit altitude. ESA lowered the GOCE orbit in four steps since July 2012. The observations at different altitudes are used to derive independent models. The comparison of the derived models indicates that the medium- and high-frequency parts are improved. This suggests that the signal-to-noise ratio of the observations is increased by lowering the satellite orbit.

In a joint analysis, the contributions of the SST-hl and SGG data are combined using the Variance Component Estimation approach. The individual analysis of the SST-hl and SGG data gives their posterior variance of unit weight (0.74, 0.74 and 0.80 for the three components of the orbit and 0.75, 0.73 and 0.75 for the three main diagonal gradient components) which determines the optimal weighting factors. Regularization is also applied to constrain the zonal and near-zonal coefficients which are severely affected by the polar gap.

Four generations of gravity field models are finally derived, using data over the same time span as the latest four generations of GOCE official models. Up to d/o 200, the cumulative geoid errors w.r.t. GOCO05s are 3.62, 3.23, 2.98 and 2.75 cm. Among the four models, the second and third generations are better than the official ones, because reprocessed gradients are used and the more accurate VCMs are constructed in the derivation of the gravity field models. The fourth and fifth generations are poorer than the official ones. Due to the down-sampling of the main diagonal gravity gradients and neglect of V_{xz} component, a loss of observations is caused that further affects the performance of the derived models.

6.2 Outlook

The regularization parameters that weigh the contribution of the constraints and observations are chosen empirically in this dissertation. Although it works well for the determination of the second generation model, the performance of constraint decreases with the increasing amount of observations from the third generation on. Optimized regularization parameters or more advanced regularization approaches can be applied in the future.

The long-wavelength gravity field that is derived from the GOCE SST-hl observations is not the most accurate one. With the integration of other data sources, the performance of the resulting model could still be significantly improved. For example, GRACE observations can be combined with GOCE observations as it has already been done in the GOCO models. In addition, SLR observations to LAGEOS can be combined to improve the performance of the very long-wavelength part.

The software that is developed for this dissertation is prepared to also process observations of other satellite missions. For example, the kinematic orbits of the SWARM satellites can be analysed so that it may close the mission gap between GOCE and GRACE follow-on. With a slight modification, the software can also be used to process future satellite gravimetry observations.

Appendix A

Temporal corrections

Since this dissertation aims to derive a gravity field model that is “static”, any temporal variations should be removed from the observations. Temporal variations are mainly caused by the direct tides, solid Earth tides, ocean tides and pole tides. According to the type of the observations, the variations are often computed in forms of potential (analysis of the orbit data in the Energy Balance Approach), acceleration (analysis of the orbit data in the Acceleration Approach) or gradient (analysis of the gravity gradients). For the direct tide, explicit equations will be provided to compute the variations. For the other tides, their contributions are conveniently modelled as variations in the standard spherical harmonic (SH) coefficients $\Delta\bar{C}_{nm}$, $\Delta\bar{S}_{nm}$, and based on these coefficients the temporal variations are then computed by a spherical harmonic synthesis.

A.1 Direct tides

Direct tides are the gravitational effect of a celestial body on the satellite in a geocentric system. As a celestial body attracts both the satellite and the Earth, the difference of both is used to express the relative attraction of the satellite w.r.t. the center of the Earth. The corrections on the satellite in terms of the potential can be written as (Hartmann and Wenzel, 1994)

$$V_j = GM_j \sum_{n=2}^{\infty} \frac{r^n}{r_j^{n+1}} \frac{1}{2n+1} \sum_{m=0}^n \bar{P}_{nm}(\cos \theta) \bar{P}_{nm}(\cos \theta_j) \cos(m\lambda - m\lambda_j), \quad (\text{A.1})$$

where (r, θ, λ) is the satellite position given in spherical coordinates, $(r_j, \theta_j, \lambda_j)$ denotes the geocentric spherical coordinates of the specific celestial body (Sun, Moon, planets) of which mass is M_j . G is the gravitational constant. The coordinates of the celestial bodies can be computed from subroutines and ephemeris (e.g., DE405) provided by the JPL planetary catalogue¹.

¹<ftp://ssd.jpl.nasa.gov/pub/eph/planets/>

In terms of accelerations, the variations caused by the direct tides can be corrected by

$$\mathbf{a}_j = GM_j \cdot \left(\frac{\mathbf{r}_j - \mathbf{r}}{|\mathbf{r}_j - \mathbf{r}|^3} - \frac{\mathbf{r}_j}{|\mathbf{r}_j|^3} \right), \quad (\text{A.2})$$

where the vectors \mathbf{r}_j and \mathbf{r} represent the Cartesian coordinates of the disturbing planets j and the satellite in the geocentric reference system.

The corrections of the gravity gradient tensor Γ_j can be obtained by differentiation of the accelerations. It is expressed in the geocentric frame as

$$\Gamma_j = \frac{GM_j}{l^5} \begin{pmatrix} 3(x_j - x)^2 - l^2 & 3(x_j - x)(y_j - y) & 3(x_j - x)(z_j - z) \\ 3(y_j - y)(x_j - x) & 3(y_j - y)^2 - l^2 & 3(y_j - y)(z_j - z) \\ 3(z_j - z)(x_j - x) & 3(z_j - z)(y_j - y) & 3(z_j - z)^2 - l^2 \end{pmatrix}, \quad (\text{A.3})$$

where $l = |\mathbf{r}_j - \mathbf{r}|$.

A.2 Solid Earth tides

The gravitational attraction of Moon, Sun and other celestial bodies does not only affect the gravity potential directly but also deforms the Earth. This results in a redistribution of masses, which has an indirect effect on the motion of the satellite due to the slight change of the Earth's potential field. The changes induced by the solid Earth tides are conveniently modelled as variations in the standard SH coefficients (Petit and Luzum, 2010). The computation will be done in a two-step procedure.

In the first step, the frequency-independent part is calculated by

$$\begin{aligned} \Delta \bar{C}_{nm} &= \frac{1}{2n+1} \sum_j \frac{GM_j}{GM_\oplus} \left(\frac{R_e}{r_j} \right)^{n+1} \bar{P}_{nm}(\cos \theta_j) (k_{nm}^R \cos m\lambda_j + k_{nm}^I \sin m\lambda_j), \\ \Delta \bar{S}_{nm} &= \frac{1}{2n+1} \sum_j \frac{GM_j}{GM_\oplus} \left(\frac{R_e}{r_j} \right)^{n+1} \bar{P}_{nm}(\cos \theta_j) (k_{nm}^R \sin m\lambda_j - k_{nm}^I \cos m\lambda_j), \end{aligned} \quad (\text{A.4})$$

where GM_j and GM_\oplus are gravitational constants for the planets and the Earth; R_e is the equatorial radius of the Earth; $(r_j, \theta_j, \lambda_j)$ denotes the body-fixed geocentric coordinates of the celestial body j ; k_{nm} are the nominal Love numbers for degree n and order m which are complex in the case of an anelastic Earth, with the real and imaginary parts labelled as k_{nm}^R and k_{nm}^I . The Love numbers are given in Tab. A.1. With Eq. (A.4), the corrections of the coefficients $\Delta \bar{C}_{nm}$ and $\Delta \bar{S}_{nm}$ for both degree 2 and 3 are computed, apart from the corrections for frequency dependence to be estimated in step 2.

Table A.1: Love numbers for the solid Earth tides as an anelastic Earth

n	m	k_{nm}^R	k_{nm}^I	$k_{nm}^{(+)}$
2	0	0.30190	-0.00000	-0.00089
2	1	0.29830	-0.00144	-0.00080
2	2	0.30102	-0.00130	-0.00057
3	0	0.093		
3	1	0.093		
3	2	0.093		
3	3	0.094		

One further computation has to be done in the first step since the degree-2 tides produce perturbations on the degree-4 coefficients. They are given by

$$\begin{aligned}\Delta\bar{C}_{4m} &= \frac{k_{2m}^{(+)}}{5} \sum_j \frac{GM_j}{GM_\oplus} \left(\frac{R_e}{r_j}\right)^3 \bar{P}_{2m}(\cos\theta_j) \cos m\lambda_j, \\ \Delta\bar{S}_{4m} &= \frac{k_{2m}^{(+)}}{5} \sum_j \frac{GM_j}{GM_\oplus} \left(\frac{R_e}{r_j}\right)^3 \bar{P}_{2m}(\cos\theta_j) \sin m\lambda_j,\end{aligned}\quad (m = 0, 1, 2). \quad (\text{A.5})$$

The frequency-dependent corrections are computed in Step 2 as the sum of contributions from a number of tidal constituents belonging to the respective bands. The correction on $\Delta\bar{C}_{20}$ is mainly caused from the long-period tidal constituents f , which reads

$$\Delta\bar{C}_{20} = \sum_f (A_f^{ip} \cos\theta_f + A_f^{op} \sin\theta_f), \quad (\text{A.6})$$

where the in-phase amplitudes A_f^{ip} and out-of-phase amplitudes A_f^{op} of the tidal constituents f are given in the Table 6.5b in [Petit and Luzum \(2010\)](#); θ_f is the argument of the corresponding tidal constituents and its computation is the same as that of the ocean tides (see section A.3).

The main contribution to $\Delta\bar{C}_{21}$, $\Delta\bar{S}_{21}$ is from the diurnal tidal constituents and, to $\Delta\bar{C}_{22}$, $\Delta\bar{S}_{22}$, it is caused by the semidiurnal tides. They can be computed by

$$\Delta\bar{C}_{2m} - i\Delta\bar{S}_{2m} = \eta_m \sum_f (A_f^{ip} + iA_f^{op}) e^{i\theta_f}, \quad (m = 1, 2) \quad (\text{A.7})$$

with $\eta_1 = -i$ and $\eta_2 = 1$. A_f^{ip} and A_f^{op} are given in the Tables 6.5a and 6.5c in [Petit and Luzum \(2010\)](#).

A.3 Ocean tides

Similar to the solid Earth tides, the oceans are deformed by the direct tides and the transport of the water causes variations in the gravity potential. The dynamic effect of ocean tides is most easily incorporated as periodic variations in the SH coefficients. These variations can be evaluated as

$$\begin{aligned}\Delta\bar{C}_{nm} &= \sum_f [(C_{f,nm}^+ + C_{f,nm}^-) \cos \theta_f + (S_{f,nm}^+ + S_{f,nm}^-) \sin \theta_f], \\ \Delta\bar{S}_{nm} &= \sum_f [(S_{f,nm}^+ - S_{f,nm}^-) \cos \theta_f - (C_{f,nm}^+ - C_{f,nm}^-) \sin \theta_f],\end{aligned}\tag{A.8}$$

where $C_{f,nm}, S_{f,nm}$ are the geopotential harmonic amplitudes for the tide constituent f , and θ_f is the argument of the tide constituent f . The superscripts $+$ and $-$ denote the retrograde waves and the prograde waves. In our computation, the FES2004 ocean tide model (Lyard et al., 2006) is used and the coefficients $C_{f,nm}^\pm, S_{f,nm}^\pm$ for the main tidal waves can be found at the web². The argument of the tidal constituents is computed by

$$\theta_f = \sum_{i=1}^6 n_i \beta_i,\tag{A.9}$$

where β_i are the Doodson's fundamental arguments (τ, s, h, p, N', p_s) , and n_i are integer multipliers, which are encoded in the 6 digit Doodson numbers (Doodson, 1921)

$$A = n_1(n_2 + 5)(n_3 + 5) \cdot (n_4 + 5)(n_5 + 5)(n_6 + 5).\tag{A.10}$$

β_i are linear combinations of the Delaunay variables (l, l', F, D, Ω) and $GMST$, as

$$\begin{aligned}\tau &= GMST + \pi - s, \\ s &= F + \Omega, \\ h &= s - D, \\ p &= s - l, \\ N' &= -\Omega, \\ p_s &= s - D - l'.\end{aligned}\tag{A.11}$$

²http://62.161.69.131/iers/convupdt/convupdt_c6.html

The Delaunay variables are computed by (Petit and Luzum, 2010)

$$\begin{aligned}
 l &= 485868.2490 + 1717915923.2178 t + 31.8792 t^2 + 0.051635 t^3, \\
 l' &= 1287104.7930 + 129596581.0481 t - 0.5532 t^2 + 0.000136D0 t^3, \\
 F &= 335779.5262 + 1739527262.8478 t - 12.7512 t^2 - 0.001037 t^3, \\
 D &= 1072260.7036 + 1602961601.2090 t - 6.3706 t^2 + 0.006593 t^3, \\
 \Omega &= 450160.3980 - 6962890.5431 t + 7.4722 t^2 + 0.007702 t^3,
 \end{aligned} \tag{A.12}$$

the unit is arcseconds, t is the Julian century. $GMST$ is computed by (Lederle, 1980)

$$GMST = 24110.5484 + 8640184.8128 t + 0.093104 t^2 - 0.0000062 t^3, \tag{A.13}$$

the unit is seconds, which can be transformed into radians by multiplying the Earth's rotation angular velocity.

A.4 Solid Earth pole tides

Solid Earth pole tides are generated by the centrifugal effect of polar motion. The perturbation on the potential is equivalent to changes on the SH coefficients $\Delta\bar{C}_{21}$ and $\Delta\bar{S}_{21}$. It reads as

$$\begin{aligned}
 \Delta\bar{C}_{21} &= -1.333 \cdot 10^{-9}(m_1 + 0.0115m_2), \\
 \Delta\bar{S}_{21} &= -1.333 \cdot 10^{-9}(m_2 - 0.0115m_1),
 \end{aligned} \tag{A.14}$$

where the wobble variables (m_1, m_2) are in arcseconds and calculated according to

$$m_1 = x_p - \bar{x}_p, \quad m_2 = y_p - \bar{y}_p, \tag{A.15}$$

where x_p, y_p are the polar coordinates in arcseconds which can be downloaded from the IERS data center³. The average polar motion variables \bar{x}_p and \bar{y}_p are calculated by

$$\bar{x}_p(t) = \sum_{i=0}^3 (t - t_0)^i \times \bar{x}_p^i, \quad \bar{y}_p(t) = \sum_{i=0}^3 (t - t_0)^i \times \bar{y}_p^i, \tag{A.16}$$

where t_0 is 2000.0 and the coefficients \bar{x}_p^i and \bar{y}_p^i are given in the Tab. A.2.

³<ftp://ftp.iers.org/products/eop/bulletinb/>

Table A.2: The coefficients \bar{x}_p^i and \bar{y}_p^i , unit is milliarcseconds per year.

i	Until 2010.0		After 2010.0	
	\bar{x}_p^i	\bar{y}_p^i	\bar{x}_p^i	\bar{y}_p^i
0	55.794	346.346	23.513	358.891
1	1.8243	1.7896	7.6141	-0.6287
2	0.18413	-0.10719	0.0	0.0
3	0.007024	-0.000908	0.0	0.0

A.5 Ocean pole tides

Not only the solid Earth, also polar motion generates a centrifugal effect on the oceans. The SH coefficients $\Delta\bar{C}_{21}$ and $\Delta\bar{S}_{21}$ are the dominant terms of the ocean pole tide, which takes approximately 90% of the variance of the ocean pole tides potential. The corrections of these terms are

$$\begin{aligned}\Delta\bar{C}_{21} &= -2.1778 \cdot 10^{-10}(m_1 - 0.01724m_2), \\ \Delta\bar{S}_{21} &= -1.7232 \cdot 10^{-10}(m_2 - 0.03365m_1),\end{aligned}\tag{A.17}$$

where the wobble variables (m_1, m_2) are in arcseconds.

Bibliography

- Albertella, A., Migliaccio, F., Sansò, F., and Tscherning, C. C. (2000). Scientific data production quality assessment using local space-wise pre-processing. *From Eötvös to mGal, Final Report, (Ed) Sünkel, H., ESA/ESTEC contract, (13392/98).*
- Anderson, E., Bai, Z., Bischof, C., Blackford, S., Demmel, J., Dongarra, J., Du Croz, J., Greenbaum, A., Hammarling, S., McKenney, A., and Sorensen, D. (1999). *LAPACK Users' Guide*. Society for Industrial and Applied Mathematics, Philadelphia, PA, third edition.
- Anton, H. (2010). *Elementary linear algebra*. John Wiley & Sons.
- Barnett, V. and Lewis, T. (1994). *Outliers in statistical data*, volume 3. Wiley New York.
- Baur, O. (2009). Tailored least-squares solvers implementation for high-performance gravity field research. *Computers & Geosciences*, 35(3):548 – 556.
- Baur, O., Bock, H., Höck, E., Jäggi, A., Krauss, S., Mayer-Gürr, T., Reubelt, T., Siemes, C., and Zehentner, N. (2014). Comparison of GOCE-GPS gravity fields derived by different approaches. *Journal of Geodesy*, 88(10):959–973.
- Baur, O., Reubelt, T., Weigelt, M., Roth, M., and Sneeuw, N. (2012). GOCE orbit analysis: Long-wavelength gravity field determination using the acceleration approach. *Advances in Space Research*, 50(3):385 – 396.
- Baur, O., Sneeuw, N., Cai, J., and Roth, M. (2010). GOCE data analysis: realization of the invariants approach in a high performance computing environment. *Signal*, 10:8.
- Baur, O., Sneeuw, N., and Grafarend, E. W. (2008). Methodology and use of tensor invariants for satellite gravity gradiometry. *Journal of Geodesy*, 82(4-5):279–293.
- Beutler, G., Jäggi, A., Mervart, L., and Meyer, U. (2010). The celestial mechanics approach: theoretical foundations. *Journal of Geodesy*, 84:605–624.
- Bjerhammar, A. (1969). On the energy integral for satellites. *Tellus*, 21(1):1–9.
- Bock, H., Jäggi, A., Beutler, G., and Meyer, U. (2014). GOCE: precise orbit determination for the entire mission. *Journal of Geodesy*, 88(11):1047–1060.
- Bock, H., Jäggi, A., Meyer, U., Visser, P., IJssel, J., Helleputte, T., Heinze, M., and Hugentobler, U. (2011). GPS-derived orbits for the GOCE satellite. *Journal of Geodesy*, 85:807–818.
- Brieden, P. and Müller, J. (2014). Validation of GOCE gravitational gradients in satellite track cross-overs. In Rizos, C. and Willis, P., editors, *Earth on the Edge: Science for a Sustainable Planet*, volume 139 of *International Association of Geodesy Symposia*, pages 399–405. Springer Berlin Heidelberg.

- Brockmann, J. M. (2014). *On High Performance Computing in Geodesy: Applications in Global Gravity Field Determination*. PhD thesis, Rheinische Friedrich-Wilhelms-Universität Bonn.
- Brockmann, J. M., Zehentner, N., Höck, E., Pail, R., Loth, I., Mayer-Gürr, T., and Schuh, W.-D. (2014). EGM_TIM_RL05: An independent geoid with centimeter accuracy purely based on the GOCE mission. *Geophysical Research Letters*, 41(22):8089–8099.
- Bruinsma, S. L., Förste, C., Abrikosov, O., Lemoine, J.-M., Marty, J.-C., Mulet, S., Rio, M.-H., and Bonvalot, S. (2014). ESA's satellite-only gravity field model via the direct approach based on all GOCE data. *Geophysical Research Letters*, 41(21):7508–7514.
- Bruinsma, S. L., Förste, C., Abrikosov, O., Marty, J.-C., Rio, M.-H., Mulet, S., and Bonvalot, S. (2013). The new ESA satellite-only gravity field model via the direct approach. *Geophysical Research Letters*, 40(14):3607–3612.
- Cesare, S. (2008). Performance requirements and budgets for the gradiometric mission. Technical report, ThalesAleniaSpace, Torino.
- Colombo, O. L. (1981). Numerical methods for harmonic analysis on the sphere. Technical report, Department of Geodetic Science.
- Ditmar, P., Kusche, J., and Klees, R. (2003). Computation of spherical harmonic coefficients from gravity gradiometry data to be acquired by the GOCE satellite: regularization issues. *Journal of Geodesy*, 77(7-8):465–477.
- Ditmar, P., Kuznetsov, V., van der Sluijs, A. v. E., Schrama, E., and Klees, R. (2006). DEOS_CHAMP-01C_70: a model of the Earth's gravity field computed from accelerations of the CHAMP satellite. *Journal of Geodesy*, 79(10-11):586–601.
- Doodson, A. T. (1921). The harmonic development of the tide-generating potential. *Proceedings of the Royal Society of London. Series A, Containing Papers of a Mathematical and Physical Character*, pages 305–329.
- EGG-C (2006). GOCE L1B products user handbook. Technical Report GOCE-GSEG-EOPG-TN-06-0137, Issue 1.1.
- EGG-C (2014). GOCE level 2 product data handbook. Technical Report GO-MA-HPF-GS-0110, Issue 5.0.
- Farahani, H. H., Ditmar, P., Klees, R., Liu, X., Zhao, Q., and Guo, J. (2013). The static gravity field model DGM-1S from GRACE and GOCE data: computation, validation and an analysis of GOCE mission's added value. *Journal of Geodesy*, 87(9):843–867.
- Floberghagen, R., Fehring, M., Lamarre, D., Muzi, D., Frommknecht, B., Steiger, C., Piñeiro, J., and Da Costa, A. (2011). Mission design, operation and exploitation of the gravity field and steady-state ocean circulation explorer mission. *Journal of Geodesy*, 85(11):749–758.
- Fuchs, M. J. and Bouman, J. (2011). Rotation of GOCE gravity gradients to local frames. *Geophysical Journal International*, 187(2):743–753.

- Gerlach, C., Sneeuw, N., Visser, P., and Švehla, D. (2003). CHAMP gravity field recovery with the energy balance approach: first results. In *First CHAMP Mission Results for Gravity, Magnetic and Atmospheric Studies*, pages 134–139. Springer.
- Götzelmann, M., Keller, W., and Reubelt, T. (2006). Gross error compensation for gravity field analysis based on kinematic orbit data. *Journal of Geodesy*, 80(4):184–198.
- Gruber, T. and Rummel, R. (2006). Concept and capability of GOCE. In *Proceedings of the GOCINA workshop*, volume 25, pages 31–37.
- Gustavson, F. G., Waśniewski, J., Dongarra, J. J., and Langou, J. (2010). Rectangular full packed format for Cholesky’s algorithm: factorization, solution, and inversion. *ACM Transactions on Mathematical Software*, 37(2):18.
- Hartmann, T. and Wenzel, H.-G. (1994). The harmonic development of the Earth tide generating potential due to the direct effect of the planets. *Geophysical Research Letters*, 21(18):1991–1993.
- Hofmann-Wellenhof, B. and Moritz, H. (2006). *Physical Geodesy*. Springer Science & Business Media.
- Holoborodko, P. (2008). Smooth noise robust differentiators. <http://www.holoborodko.com/pavel/numerical-methods/>.
- Ilk, K. H., Mayer-Gürr, T., and Feuchtinger, M. (2005). Gravity field recovery by analysis of short arcs of CHAMP. In *Earth Observation with CHAMP*, pages 127–132. Springer.
- Intel (2009). *Intel Math Kernel Library. Reference Manual*. Intel Corporation. Santa Clara, USA. ISBN 630813-054US.
- Jäggi, A., Beutler, G., and Mervart, L. (2010). GRACE gravity field determination using the Celestial Mechanics Approach: First results. In Mertikas, S. P., editor, *Gravity, Geoid and Earth Observation*, volume 135 of *International Association of Geodesy Symposia*, pages 177–184. Springer Berlin Heidelberg.
- Jäggi, A., Bock, H., Prange, L., Meyer, U., and Beutler, G. (2011). GPS-only gravity field recovery with GOCE, CHAMP, and GRACE. *Advances in Space Research*, 47(6):1020–1028.
- Jekeli, C. (1999). The determination of gravitational potential differences from satellite-to-satellite tracking. *Celestial Mechanics and Dynamical Astronomy*, 75(2):85–101.
- Johannessen, J., Balmino, G., Le Provost, C., Rummel, R., Sabadini, R., Sünkel, H., Tscherning, C., Visser, P., Woodworth, P., Hughes, C., Legrand, P., Sneeuw, N., Perosanz, F., Aguirre-Martinez, M., Rebhan, H., and Drinkwater, M. (2003). The European gravity field and steady-state ocean circulation explorer satellite mission its impact on geophysics. *Surveys in Geophysics*, 24(4):339–386.
- Kaula, W. (2000). *Theory of Satellite geodesy: applications of satellites to geodesy*. Courier Corporation.

- Kern, M., Preimesberger, T., Allesch, M., Pail, R., Bouman, J., and Koop, R. (2005). Outlier detection algorithms and their performance in GOCE gravity field processing. *Journal of Geodesy*, 78(9):509–519.
- Khan, I. R. and Ohba, R. (1999). Closed-form expressions for the finite approximations of first and higher derivatives based on Taylor series. *J. Comput. Appl. Math.*, 107(2):179–193.
- Koch, K.-R. (1999). *Parameter Estimation and Hypothesis Testing in Linear Models*. Springer.
- Koch, K.-R., Kuhlmann, H., and Schuh, W.-D. (2010). Approximating covariance matrices estimated in multivariate models by estimated auto- and cross-covariances. *Journal of Geodesy*, 84(6):383–397.
- Koch, K.-R. and Kusche, J. (2002). Regularization of geopotential determination from satellite data by variance components. *Journal of Geodesy*, 76(5):259–268.
- Koop, R. (1993). *Global gravity field modelling using satellite gravity gradiometry*. PhD thesis, Delft: Nederlandse Commissie voor Geodesie.
- Kusche, J. and Klees, R. (2002). Regularization of gravity field estimation from satellite gravity gradients. *Journal of Geodesy*, 76(6-7):359–368.
- Lederle, T. (1980). The IAU/1976/system of astronomical constants. *Mitteilungen der Astronomischen Gesellschaft Hamburg*, 48:59–65.
- Liu, X. (2008). *Global gravity field recovery from satellite-to-satellite tracking data with the acceleration approach*. PhD thesis, TU Delft: Delft University of Technology.
- Lyard, F., Lefevre, F., Letellier, T., and Francis, O. (2006). Modelling the global ocean tides: modern insights from FES2004. *Ocean Dynamics*, 56(5-6):394–415.
- Mayer-Gürr, T., Ilk, K., Eicker, A., and Feuchtinger, M. (2005). ITG-CHAMP01: a CHAMP gravity field model from short kinematic arcs over a one-year observation period. *Journal of Geodesy*, 78:462–480.
- Mayer-Gürr, T., Kurtenbach, E., and Eicker, A. (2010). ITG-Grace2010: the new GRACE gravity field release computed in Bonn. In *EGU General Assembly Conference Abstracts*, volume 12, page 2446.
- Metzler, B. and Pail, R. (2005). GOCE data processing: The spherical cap regularization approach. *Studia Geophysica et Geodaetica*, 49(4):441–462.
- Migliaccio, F., Reguzzoni, M., Sansò, F., Tscherning, C., and Veicherts, M. (2010). GOCE data analysis: the space-wise approach and the first space-wise gravity field model. In *Proceedings of the ESA living planet symposium*, volume 28.
- Migliaccio, F., Reguzzoni, M., Sansò, F., and Tselfes, N. (2009). An error model for the GOCE space-wise solution by Monte Carlo methods. In *Observing our Changing Earth*, pages 337–344. Springer.
- Müller, J. (2001). *Die Satellitengradiometriemission GOCE: Theorie, technische Realisierung und wissenschaftliche Nutzung*. Habilitation, DGK, Reihe C, Heft 541, Verlag der Bayerischen Akademie der Wissenschaften, ISSN 0065-5325.

- O'Keefe, J. A. (1957). An application of Jacobi's integral to the motion of an Earth satellite. *The Astronomical Journal*, 62:265.
- Pail, R. (2014). Its all about statistics: Global gravity field modeling from GOCE and complementary data. In Freeden, W., Nashed, M. Z., and Sonar, T., editors, *Handbook of Geomatics*, pages 1–24. Springer Berlin Heidelberg.
- Pail, R., Bruinsma, S., Migliaccio, F., Förste, C., Goiginger, H., Schuh, W.-D., Höck, E., Reguzzoni, M., Brockmann, J., Abrikosov, O., Veicherts, M., Fecher, T., Mayrhofer, R., Krasbutter, I., Sansò, F., and Tscherning, C. C. (2011). First GOCE gravity field models derived by three different approaches. *Journal of Geodesy*, 85(11):819–843.
- Pail, R., Fecher, T., Murböck, M., Rexer, M., Stetter, M., Gruber, T., and Stummer, C. (2013). Impact of GOCE Level 1b data reprocessing on GOCE-only and combined gravity field models. *Studia Geophysica et Geodaetica*, 57(2):155–173.
- Pail, R., Goiginger, H., Mayrhofer, R., Schuh, W.-D., Brockmann, J. M., Krasbutter, I., Höck, E., and Fecher, T. (2010). GOCE gravity field model derived from orbit and gradiometry data applying the time-wise method. In *Proceedings of the ESA living planet symposium*, volume 28. European Space Agency Bergen, Norway.
- Pail, R. and Wermut, M. (2003). GOCE SGG and SST quick-look gravity field analysis. *Advances in Geosciences*, 1(1):5–9.
- Petit, G. and Luzum, B. (2010). IERS Conventions (2010). Technical Report IERS Technical Note No. 36.
- Reguzzoni, M. and Tselfes, N. (2009). Optimal multi-step collocation application to the space-wise approach for GOCE data analysis. *Journal of Geodesy*, 83(1):13–29.
- Reigber, C., Lühr, H., and Schwintzer, P. (2002). CHAMP mission status. *Advances in Space Research*, 30(2):129 – 134.
- Reigber, C., Schwintzer, P., Neumayer, K.-H., Barthelmes, F., König, R., Förste, C., Balmino, G., Biancale, R., Lemoine, J.-M., Loyer, S., et al. (2003). The CHAMP-only Earth gravity field model EIGEN-2. *Advances in Space Research*, 31(8):1883–1888.
- Reubelt, T., Austen, G., and Grafarend, E. (2003a). Harmonic analysis of the Earth's gravitational field by means of semi-continuous ephemerides of a low Earth orbiting GPS-tracked satellite. case study: CHAMP. *Journal of Geodesy*, 77:257–278.
- Reubelt, T., Austen, G., and Grafarend, E. W. (2003b). Space gravity spectroscopy - determination of the Earth's gravitational field by means of Newton interpolated LEO ephemeris case studies on dynamic (CHAMP rapid science orbit) and kinematic orbits. *Advances in Geosciences*, 1:127–135.
- Reubelt, T., Götzelmann, M., and Grafarend, E. W. (2006). Harmonic analysis of the Earth's gravitational field from kinematic CHAMP orbits based on numerically derived satellite accelerations. *Observation of the Earth system from space*. Springer, New York, pages 27–42.
- Roth, M., Baur, O., and Keller, W. (2012). “brute-force” solution of large-scale systems of equations in a MPI-PBLAS-ScaLAPACK environment. In *High Performance Computing in Science and Engineering'11*, pages 581–594. Springer.

- Rummel, R. (1986). Satellite gradiometry. In Sünkel, H., editor, *Mathematical and Numerical Techniques in Physical Geodesy*, volume 7 of *Lecture Notes in Earth Sciences*, pages 317–363. Springer Berlin Heidelberg.
- Rummel, R., Balmino, G., Johannessen, J., Visser, P., and Woodworth, P. (2002). Dedicated gravity field missions-principles and aims. *Journal of Geodynamics*, 33(1 - 2):3 – 20.
- Rummel, R., van Gelderen, M., Koop, R., Schrama, E., Sansò, F., Brovelli, M., Migliaccio, F., and Sacerdote, F. (1993). Spherical harmonic analysis of satellite gradiometry. Publications on Geodesy - New Series 39, Netherlands Geodetic Commission.
- Rummel, R., Yi, W., and Stummer, C. (2011). GOCE gravitational gradiometry. *Journal of Geodesy*, 85(11):777–790.
- Savitzky, A. and Golay, M. J. E. (1964). Smoothing and differentiation of data by simplified least squares procedures. *Analytical Chemistry*, 36.
- Schall, J., Eicker, A., and Kusche, J. (2014). The ITG-Goce02 gravity field model from GOCE orbit and gradiometer data based on the short arc approach. *Journal of Geodesy*, 88(4):403–409.
- Schneider, M. (1968). A general method of orbit determination. *Royal Aircraft Translation*, (1279).
- Schneider, M. (1969). Outline of a general orbit determination method. In Champion, K. S. W.; Smith, P. A. S.-R. R. L., editor, *Space Research IX, Proceedings of Open Meetings of Working Groups (OMWG) on Physical Sciences of the 11th Plenary Meeting of the Committee on Space Research (COSPAR), Tokyo*, pages 37–40. North-Holland Publishing Company. Mitteilungen aus dem Institut für Astronomische und Physikalische Geodäsie, Nr. 51.
- Schuh, W. (1996). Tailored numerical solution strategies for the global determination of the Earth's gravity field. Technical report.
- Schuh, W.-D. (2003). The processing of band-limited measurements; filtering techniques in the least squares context and in the presence of data gaps. *Space Science Reviews*, 108(1-2):67–78.
- Schwintzer, P. (1990). Sensitivity analysis in least squares gravity modelling by means of redundancy decomposition of stochastic a priori information. *Deutsches Geodätisches Forschungsinstitut*.
- Siemes, C. (2008). *Digital filtering algorithms for decorrelation within large least squares problems*. PhD thesis, Institut für Geodäsie und Geoinformation, Universität Bonn. DGK series C, No. 707, Verlag der Bayerischen Akademie der Wissenschaften.
- Sneeuw, N. (2000). *A semi-analytical approach to gravity field analysis from satellite observations*. DGK series C, No. 527, Verlag der Bayerischen Akademie der Wissenschaften.
- Sneeuw, N. and van Gelderen, M. (1997). The polar gap. In *Geodetic boundary value problems in view of the one centimeter geoid*, pages 559–568. Springer.

- Stummer, C. S. (2013). *Gradiometer data processing and analysis for the GOCE mission*. PhD thesis, Fakultät für Bauingenieur- und Vermessungswesen, TU München. DGK series C, No. 695, Verlag der Bayerischen Akademie der Wissenschaften.
- Tapley, B. D., Bettadpur, S., Watkins, M., and Reigber, C. (2004). The gravity recovery and climate experiment: Mission overview and early results. *Geophysical Research Letters*, 31(9).
- Van den IJssel, J., Visser, P., Doornbos, E., Meyer, U., Bock, H., and Jäggi, A. (2011). GOCE SSTI L2 tracking losses and their impact on POD performance. In *Proceedings of 4th International GOCE User Workshop, Munich, Germany, 31 March-1 April 2011; ESA SP-696*. European Space Agency (ESA).
- Visser, P., Sneeuw, N., and Gerlach, C. (2003). Energy integral method for gravity field determination from satellite orbit coordinates. *Journal of Geodesy*, 77(3-4):207–216.
- Weigelt, M. (2007). *Global and Local Gravity Field Recovery from Satellite-to-satellite Tracking*. PhD thesis, University of Calgary (Canada).
- Weigelt, M., Baur, O., Reubelt, T., Sneeuw, N., and Roth, M. (2011). Long wavelength gravity field determination from GOCE using the acceleration approach. In *Proceedings of the 4th GOCE User Workshop, ESA SP-696*. ESA.
- Wermuth, M. (2008). *Gravity Field Analysis from the Satellite Missions CHAMP and GOCE*. PhD thesis, Fakultät für Bauingenieur- und Vermessungswesen, Technische Universität München.
- Xu, C., Sideris, M. G., and Sneeuw, N. (2008). The torus approach in spaceborne gravimetry. In *VI Hotine-Marussi Symposium on Theoretical and Computational Geodesy*, pages 23–28. Springer.
- Yi, W. (2012a). An alternative computation of a gravity field model from GOCE. *Advances in Space Research*, 50(3):371 – 384.
- Yi, W. (2012b). *The Earth's gravity field from GOCE*. PhD thesis, Fakultät für Bauingenieur- und Vermessungswesen, Technische Universität München.
- Yi, W., Rummel, R., and Gruber, T. (2013). Gravity field contribution analysis of GOCE gravitational gradient components. *Studia Geophysica et Geodaetica*, 57(2):174–202.

List of Figures

1.1	Gravity anomalies computed from GOCO03s, showing deviations from the theoretical gravity of an idealized smooth Earth, the so-called earth ellipsoid	1
2.1	The arrangement of the SH coefficients, zonal, sectorial and tesseral coefficients are in different colors.	22
3.1	Concept of Satellite-to-Satellite Tracking in high-low mode (Rummel et al., 2002)	26
3.2	Flowchart of global gravity field recovery from GOCE SST-hl data	33
3.3	The daily altitudes of the GOCE satellite from November 2009 to October 2013	34
3.4	The probability density distribution of the orbit differences between PKI and PRD	35
3.5	Spatial distribution of the outliers of PKI orbit (November 2009)	36
3.6	The scheme of the EDF, cited from Baur et al. (2012)	37
3.7	Frequency responses of the second-order differentiators	40
3.8	Tidal accelerations a_z in November 2009, unit is m/s^2	41
3.9	Root PSDs of the tidal accelerations a_z in November 2009	42
3.10	Spatial distribution of the tidal corrections in November and December, 2009 .	43
3.11	Root PSDs of the residual accelerations	44
3.12	Time and memory used to assemble the normal matrix. The computation is based on a single acceleration component from November and December, 2009. The sampling interval is 1 s.	45
3.13	Two-dimensional error spectrum of the estimated coefficients (unitless). Left: coefficient differences w.r.t. ITG-Grace2010s; right: formal errors. Both are in logarithmic scale.	46
3.14	One-dimensional error spectrum of the estimated coefficients, left: DE-RMS; right: degree median values. The red curves represent the coefficient differences and the blue curves represent formal errors.	47
3.15	The cumulative geoid height error w.r.t ITG-Grace2010s	47

3.16	The DE-RMS of the SST only solutions w.r.t. ITG-Grace2010s	48
3.17	The cumulative geoid height errors of the SST only solutions	48
4.1	Configuration of EGG. 6 accelerometers in pairs are orthogonally mounted in three gradiometer arms. Each accelerometer has 3 axes, with 2 ultra sensitive axes indicated by solid arrows and 1 less sensitive axis as dashed arrow (EGG-C, 2006).	51
4.2	Flowchart of gravity field recovery from GOCE SGG data	56
4.3	Time series of the gravity gradients on November 1, 2009	59
4.4	Root PSDs of the gravity gradients on November 1, 2009	60
4.5	Spatial representation of the gravity gradients on November 1, 2009	61
4.6	Coloured noise behaviour of the gravity gradients	62
4.7	Time series plot of gradients, with anomalous observations on February 5 and 7, 2010	65
4.8	Spatial distribution of the outliers in November and December 2009, represented by the blue dots	67
4.9	Data gap of V_{xx} in March, 2010	68
4.10	Time and memory that are required to assemble the normal matrix. The computation is based on a single gradient component from November and December, 2009. The sampling interval is reduced to 2 s.	72
4.11	DE-RMS and degree median of the gravity field model recovered from V_{zz} with sampling intervals of 1 s, 2 s and 5 s. The time period is November and December 2009.	74
4.12	DE-RMS and degree median of the gravity field model recovered from V_{zz} with different arc lengths of 12 minutes, 15 minutes and 18 minutes. The time period is November and December 2009.	75
4.13	Comparison of the gravity field models recovered with and without consideration of VCM, left: DE-RMS, right: degree median	75
4.14	The effect of the quality of the VCM on the recovered gravity field models, left: DE-RMS, right: degree median	76
4.15	Two-dimensional error spectrum of the spherical harmonic coefficients estimated from the individual gradient components, $V_{xx}, V_{yy}, V_{zz}, V_{xz}$ from top to bottom. Coefficient differences w.r.t. GOCO05S (left) and formal errors (right), both are unitless and shown in logarithmic scale.	77

4.16	The top and middle panel are the two-dimensional error spectrum of the spherical harmonic coefficients estimated from V_{zz} and $V_{xx} + V_{yy}$, with coefficient differences w.r.t. GOCO05S (left) and formal errors (right). The bottom panel shows the difference of the two solutions.	79
4.17	The top and middle panel are the two-dimensional error spectrum of the spherical harmonic coefficients estimated from V_{xz} and $V_{xx} + V_{zz}$, with coefficient differences w.r.t. GOCO05S (left) and formal errors (right). The bottom panel shows the difference of the two solutions.	80
4.18	DE-RMS of the gravity field models that are recovered from bimonthly gravity gradients	82
4.19	Daily mean altitude of the GOCE satellite since July, 2012	83
4.20	Root PSDs of V_{xx} during different time periods	84
4.21	Root PSDs of V_{yy} during different time periods	84
4.22	Root PSDs of V_{zz} during different time periods	84
4.23	Gravity field models recovered from V_{xx} of each group, left: DE-RMS, right: degree median	85
4.24	Gravity field models recovered from V_{yy} of each group, left: DE-RMS, right: degree median	85
4.25	Gravity field models recovered from V_{zz} of each group, left: DE-RMS, right: degree median	86
4.26	Comparison of the gravity field models recovered from the main diagonal gravity gradients of two time periods. One is from November 2009 to July 2012; the other one is from September 2012 to October 2013.	86
4.27	Final solutions from the main diagonal gravity gradients, SGG_R1 to SGG_R5 from top to bottom. Coefficient differences w.r.t. GOCO05S (left) and formal errors (right), both are unitless and shown in logarithmic scale.	88
4.28	Final solutions from the main diagonal gravity gradients, left: DE-RMS, right: degree median. The solid lines represent the coefficient difference w.r.t. GOCO05S while the dashed lines represent formal errors.	89
4.29	Final solutions from the main diagonal gravity gradients, left: DE-RMS, right: degree median. The solid lines represent the coefficient difference w.r.t. EGM2008 while the dashed lines represent formal errors.	89
5.1	Degree-Error RMS of the IFE gravity field solutions w.r.t. EGM2008. Left: all coefficients are considered; right: the zonal and near-zonal coefficients are excluded.	94

5.2	Degree-Error RMS of the IFE gravity field solutions w.r.t. EIGEN-6c4. Left: all coefficients are considered; right: the zonal and near-zonal coefficients are excluded.	94
5.3	Degree-Error RMS of the IFE gravity field solutions w.r.t. GOCO05s. Left: all coefficients are considered; right: the zonal and near-zonal coefficients are excluded.	95
5.4	Cumulative geoid errors of the IFE gravity field solutions w.r.t. EIGEN-6C4 (left) and GOCO05S (right). The zonal and near-zonal coefficients are excluded to calculate the cumulative geoid errors.	95
5.5	Cumulative geoid errors of the IFE gravity field solutions w.r.t. EIGEN-6C4 (left) and GOCO05S (right). The zonal and near-zonal coefficients as well as the low degree (d/o 2 to 4) coefficients are excluded to calculate the cumulative geoid errors.	96
5.6	Comparison of the second generation of GOCE models w.r.t. GOCO05s. Left: Degree-Error RMS; right: cumulative geoid error. The zonal and near-zonal coefficients are not taken into account, and the cumulative geoid errors are computed starting from d/o 5.	98
5.7	Comparison of the third generation of GOCE models w.r.t. GOCO05s. Left: Degree-Error RMS; right: cumulative geoid error. The zonal and near-zonal coefficients are not taken into account, and the cumulative geoid errors are computed starting from d/o 5.	99
5.8	Comparison of the fourth generation of GOCE models w.r.t. GOCO05s. Left: Degree-Error RMS; right: cumulative geoid error. The zonal and near-zonal coefficients are not taken into account, and the cumulative geoid errors are computed starting from d/o 5.	100
5.9	Comparison of the fifth generation of GOCE models w.r.t. GOCO05s. Left: Degree-Error RMS; right: cumulative geoid error. The zonal and near-zonal coefficients are not taken into account, and the cumulative geoid errors are computed starting from d/o 5.	101
5.10	Differences of the TIM and IFE solutions to EGM2008 in terms of geoid heights	103
5.11	Differences of the TIM and IFE solutions to EGM2008 in terms of gravity field anomalies	104

List of Tables

2.1	Expressions of the symbols γ, p, α, β in Eq. (2.2) are given. $\bar{P}'_{nm}, \bar{P}''_{nm}$ denote the first- and second-order derivatives of the Legendre functions w.r.t. θ	9
4.1	Data volumes that are used for the recovery of the five generations of gravity field models (only the end dates are given)	58
4.2	Available computing power of the three main clusters	71
5.1	Details of the published GOCE gravity field models and the IFE solutions	97
5.2	Comparison of the TIM, DIR and IFE solutions. The standard deviations of the geoid height differences and gravity anomaly differences w.r.t. EGM2008 are calculated. The models are truncated at d/o 250.	102
A.1	Love numbers for the solid Earth tides as an anelastic Earth	111
A.2	The coefficients \bar{x}_p^i and \bar{y}_p^i , unit is milliarcseconds per year.	114

List of Abbreviations

CHAMP	CHallenging Minisatellite Payload
CMA	Common Mode Accelerations
DE-RMS	Degree-Error Root Mean Square
DIR	Direct approach
DMA	Differential Mode Accelerations
d/o	degree and order
EDF	Extended Differentiation Filter
EGG	Electrostatic Gravity Gradiometer
ERF	Earth-fixed Reference Frame
ESA	European Space Agency
GNSS	Global Navigation Satellite System
GOCE	Gravity field and steady-state Ocean Circulation Explorer
GPS	Global Positioning System
GRACE	Gravity Recovery And Climate Experiment
GRF	Gradiometer Reference Frame
HPF	High Performance Facility
IAQ	Inertial Attitude Quaternions
IRF	Inertial Reference Frame
LAGEOS	Laser Geodynamics Satellite
LNOF	Local North-Oriented Frame
LS	Least-Squares
LUIS	Leibiz Universität IT Services
MBW	Measurement Band Width
OMC	Observed-Minus-Computed
PKI	Precise KInematic
PRD	Precise Reduced-Dynamic
PSD	Power Spectral Density
RFP	Rectangular Full Package
SGG	Satellite Gravity Gradiometry
SH	Spherical Harmonic
SHA	Spherical Harmonic Analysis
SHS	Spherical Harmonic Synthesis
SNR	Signal-to-Noise Ratio
SPW	Space-wise approach
SST-hl	Satellite-to-Satellite Tracking in high-low mode
SST-ll	Satellite-to-Satellite Tracking in low-low mode
TIM	Time-wise approach
VCE	Variance Component Estimation
VCM	Variance/Covariance Matrix

Curriculum Vitae

Personal information

Name	Hu Wu
Date of birth	25.09.1986
Place of birth	Hefei, Anhui
Nationality	Chinese

Educational background

since 10.2011	PhD candidate in physical geodesy, at Institut für Erdmessung, Leibniz Universität Hannover, Hannover, Lower Saxony, Germany
09.2009 – 07.2011	Master of Science in geodesy, at Wuhan University, Wuhan, Hubei, China
09.2005 – 07.2009	Bachelor of Science in Geomatics engineering, at China University of Petroleum (East China), Qingdao, Shandong, China
09.2004 – 06.2005	Senior stage of middle school, at Feidong Shengquan Middle School, Hefei, Anhui, China
09.2001 – 06.2004	Senior stage of middle school, at First Middle School of Feidong Hefei, Anhui, China
09.1998 – 06.2001	Junior stage of middle school, at First Middle School of Liangyuan Hefei, Anhui, China

Acknowledgements

First of all, I would like to express my gratitude to Prof. Jürgen Müller as my supervisor for all the research guidance, personal help and financial support he has provided me throughout my Ph.D work. I have benefited a lot from his professional insight of our research field and his supportive leadership for the free research atmosphere in our group.

Moreover, I want to thank Prof. Wolf-Dieter Schuh and Prof. Christian Heipke for being the reviewers of my dissertation and members of the examination committee. Their constructive feedback in the examination and the useful comments afterwards are greatly acknowledged.

Furthermore, I want to thank my colleagues, in particular Phillip Brieden for always being willing to help me. We have had a lot of interesting discussions that have benefited my research and helped me to being better adapted in Germany. I also want to thank Dr. Miao Lin for being a wonderful and helpful office-mate for the past five years. My thanks also go to all the other colleagues at IfE for the great teamwork and support, and my friends for their spiritual encouragements. Meeting you all in Hannover is a treasure of my life.

I also appreciate the support of Leibniz Universität IT Service (LUIS). The challenging task of computation in my Ph.D work is accomplished in the cluster system of LUIS. Special thanks also go to the China Scholarship Council (CSC) for the funding support of my study in Germany.

Finally, I want to thank my parents for their love and generous support in all aspects of my life, and my sisters for their devotional support. I appreciate the birth of my lovely daughter, Xinyuan. You have made me a stronger father and a stronger man to cope with all the challenges in our life. Last but not the least, I want to thank my wife, Ming Li, for all her understanding, patience and support during the whole period of my Ph.D. Without your motivation and loving support this dissertation would not have been imaginable. It is dedicated to all of you!

